

© 2020 by Roberto E. Fairhurst Agosta. All rights reserved.

MULTI-PHYSICS AND TECHNICAL ANALYSIS OF HIGH-TEMPERATURE GAS-COOLED  
REACTORS FOR HYDROGEN PRODUCTION

BY

ROBERTO E. FAIRHURST AGOSTA

THESIS

Submitted in partial fulfillment of the requirements  
for the degree of Master of Science in Nuclear, Plasma, and Radiological Engineering  
with a concentration in Computational Science and Engineering  
in the Graduate College of the  
University of Illinois at Urbana-Champaign, 2020

Urbana, Illinois

Master's Committee:

Assistant Professor Kathryn D. Huff, Advisor  
Associate Professor and Associate Head for Undergraduate Programs, Tomasz Kozlowski

# Abstract

The future energy needs require the development of clean energy sources to ease the increasing environmental concerns. High-Temperature Gas-cooled Reactors have several desirable features that make them ideal candidates for the near-future large-scale deployment. Some of these features are a high temperature and high thermal cycle efficiency, which enable a wide range of process heat applications, such as hydrogen production. Implementing hydrogen economies can decarbonize the transport and power sectors, offering an alternative to ease climate change.

This work uses Moltres as the primary simulation tool. Although Moltres original development targeted Molten Salt Reactors, this work studies Moltres applicability to multi-physics simulations of prismatic High-Temperature Gas-cooled Reactors. Multi-physics simulations are necessary for assessing reactor safety characteristics. Ensuring Moltres' multi-physics modeling capabilities requires assessing the independent modeling capabilities of the different involved physical phenomena. Therefore, this thesis breaks down the analysis into three parts: stand-alone neutronics, stand-alone thermal-fluids, and coupled neutronics/thermal-fluids.

Regarding stand-alone neutronics, several analyses compare the results calculated by Moltres and Serpent on a model of the MHTGR-350. The first analysis studies the energy group structure effects on the simulation of a fuel column. The results of the study suggest using a 15-energy group structure for attaining a desirable accuracy. The following analysis focuses on the full-core problem and compares different aspects of the simulations, concluding that Moltres obtains reasonably accurate results. The final study on stand-alone neutronics describes Moltres results of Phase I Exercise 1 of the OECD/NEA MHTGR-350 Benchmark. The benchmark exercise proved to be a modeling challenge, requiring the implementation of several approximations. For the most part, this thesis demonstrates Moltres' capability to simulate stand-alone neutronics of prismatic High-Temperature Gas-cooled Reactors.

Regarding stand-alone thermal-fluids, several studies compare Moltres results to previously published results. These studies focus on local models such as the unit cell and the fuel column problems, for which Moltres results differ by less than 2% from the published results. Further studies analyze the possibility of extending the thermal-fluids model implemented in the previous problems to a full-core simulation, finding a high memory requirement imposed by the simulations. The full-core simulations focus on Phase I Exercise 2 of the benchmark, for which

the implementation of a two-level approach in Moltres was necessary. The study's results were **within an 11.3% difference** to the published results, concluding that further analysis is required.

Regarding coupled neutronics/thermal-fluids, the analysis describes Phase I Exercise 3 of the benchmark. The exercise uses a simplified model that **helps** visualize some of the essential aspects of multi-physics simulations in Moltres. This exercise finds some **flaws** in Moltres' model and sets a basis for future work.

This thesis aligns with the University of Illinois' goals to reduce carbon emissions from its campus's electricity generation and transportation sectors. This work focuses on two main analysis by introducing a nuclear reactor coupled to a hydrogen plant as a solution. The first analysis evaluates the conversion of the university fleet **along with** the mass transit transport system in Urbana-Champaign to Fuel Cell Electric Vehicles. The second analysis investigates the duck curve phenomenon in the university's grid and introduces a mitigation strategy that may reduce the reliance on dispatchable sources. These studies emphasize how nuclear energy and hydrogen production can potentially mitigate climate change.

*A mi familia, for their unconditional support.*

# Acknowledgments

I wish to express my gratitude to my advisor Dr. Kathryn Huff, who guided me from my academic beginnings. I would also like to thank Dr. Tomasz Kozlowski for his help and invaluable comments as the second reader of this thesis. I wish to acknowledge Dr. Paul Fischer, Dr. Rizwan Uddin, and Dr. Caleb Brooks for their time and discussions helpful to this work.

Besides the support from several faculty, this work was possible due to day-to-day motivation from my fellow group-mates Sam Dotson, Greg Westphal, Kip Kleimenhagen, Andrei Rykhlevskii, Gwen Chee, and Sun Myung Park. I also much appreciate Nataly Panczyk's and Gavin Davis' help with proofreading my writing. Finally, I want to acknowledge my family, who, even though we were more than five thousand miles apart, their support and encouragement were always present. I also wanted to express my gratitude to Daniela Calero for her moral support throughout the COVID-19 pandemic.

# Table of Contents

<b>List of Tables . . . . .</b>	<b>viii</b>
<b>List of Figures . . . . .</b>	<b>ix</b>
<b>Chapter 1 Introduction . . . . .</b>	<b>1</b>
1.1 The Prismatic High-Temperature Gas-Cooled Reactor . . . . .	1
1.2 Motivation . . . . .	5
1.3 Objectives . . . . .	6
<b>Chapter 2 Literature Review . . . . .</b>	<b>8</b>
2.1 Prismatic HTGR Diffusion Solvers . . . . .	8
2.1.1 Energy group structure analysis . . . . .	10
2.1.2 Summary of Prismatic HTGR Diffusion Solvers . . . . .	11
2.2 Prismatic HTGR Thermal-fluids . . . . .	12
2.2.1 Summary of Prismatic HTGR Thermal-fluids . . . . .	15
2.3 Prismatic HTGR Multi-physics . . . . .	16
2.3.1 Summary of Prismatic HTGR Multi-physics . . . . .	18
<b>Chapter 3 Methodology . . . . .</b>	<b>20</b>
3.1 Computational tools . . . . .	20
3.1.1 MOOSE . . . . .	20
3.1.2 Moltres . . . . .	21
3.1.3 Serpent . . . . .	21
3.2 Mathematical basis . . . . .	22
3.2.1 Diffusion and precursors equations . . . . .	22
3.2.2 Thermal-fluids . . . . .	24
3.3 OECD/NEA MHTGR-350 Benchmark . . . . .	26
3.4 MHTGR-350 Reactor Description . . . . .	26
3.5 Organization of the Simulations . . . . .	30
<b>Chapter 4 Neutronics . . . . .</b>	<b>31</b>
4.1 Preliminary studies . . . . .	31
4.1.1 Homogeneous vs. heterogeneous isotope distribution . . . . .	31
4.1.2 Problem set-up . . . . .	33
4.2 Serpent-Moltres comparison . . . . .	37
4.2.1 Fuel column . . . . .	37
4.2.2 Full-core . . . . .	44
4.3 OECD/NEA MHTGR-350 Benchmark: Phase I Exercise 1 . . . . .	47
4.3.1 Periodic vs Reflective Boundary Conditions . . . . .	52
4.4 Conclusions . . . . .	52

<b>Chapter 5 Thermal-fluids . . . . .</b>	<b>55</b>
5.1 Preliminary studies . . . . .	55
5.1.1 Verification of the thermal-fluids model . . . . .	55
5.1.2 Unit cell problem . . . . .	57
5.2 Fuel column . . . . .	60
5.2.1 Flow distribution analysis . . . . .	62
5.2.2 Mesh convergence analysis . . . . .	65
5.3 OECD/NEA MHTGR-350 Benchmark: Phase I Exercise 2 . . . . .	67
5.4 Coupled simulations . . . . .	71
5.4.1 OECD/NEA MHTGR-350 Benchmark: Phase I Exercise 3 . . . . .	71
5.4.2 Discussion . . . . .	72
5.4.3 Coupled exercise with average temperature thermal feedback . . . . .	75
5.5 Conclusions . . . . .	75
<b>Chapter 6 Hydrogen Production . . . . .</b>	<b>79</b>
6.1 Introduction . . . . .	79
6.1.1 Illinois Climate Action Plan . . . . .	81
6.2 Objectives . . . . .	82
6.3 Hydrogen production methods . . . . .	82
6.3.1 Electrolysis . . . . .	82
6.3.2 Sulfur-Iodine Thermochemical Cycle . . . . .	84
6.4 Microreactors and Small Modular Reactors . . . . .	86
6.5 Methodology . . . . .	87
6.6 Results . . . . .	88
6.6.1 Transportation . . . . .	89
6.6.2 Electricity Generation . . . . .	91
6.7 Conclusions . . . . .	94
<b>Chapter 7 Conclusions . . . . .</b>	<b>96</b>
7.1 Contribution . . . . .	96
7.2 Future Work . . . . .	98
8.1 Neutron flux equations . . . . .	100
8.2 Thermal-fluids equations . . . . .	102
8.3 Coolant distribution equation . . . . .	106
9.1 Group constants homogenization . . . . .	108
9.2 Group constants condensation . . . . .	109
9.3 Benchmark group constants . . . . .	110
10.1 Verification of the thermal-fluids model . . . . .	111
<b>References . . . . .</b>	<b>113</b>

# List of Tables

3.1	Description of the OECD/NEA MHTGR-350 Benchmark phases and exercises.	27
3.2	MHTGR-350 Characteristics [4].	28
3.3	MHTGR350 fuel element characteristics [4].	29
3.4	TRISO and fuel compact characteristics [4].	29
3.5	Burnable poison compact characteristics [4].	30
4.1	Neutron mean free path in different materials. Values expressed in [cm].	36
4.2	Energy group structure [101].	38
4.3	Eigenvalues calculated by Serpent and reactivity difference between eigenvalues calculated by Moltres and Serpent, see equation 4.3, for the different energy group structures.	41
4.4	Axial flux relative difference $L_2$ -norm for various energy group structures. Values expressed in [%].	44
4.5	Comparison between Serpent and Moltres-derived eigenvalues.	45
4.6	Global parameters.	50
4.7	Global parameter comparison for different types of BCs.	52
5.1	Problem characteristics.	56
5.2	Problem characteristics.	58
5.3	Comparison between In et al. [76] and Moltres/MOOSE results.	59
5.4	Thermal conductivity coefficients [113].	61
5.5	Constant problem characteristics.	61
5.6	Mass flow rate determined from Sato's calculation [79]. Values expressed in [g/s].	61
5.7	Comparison of the maximum temperatures calculated by this work and the reference values from Sato et al. [79]. Temperature values expressed in [°C].	62
5.8	Comparison of the calculated flow rates and the reference values [79]. Mass flow rates values expressed in [ $\text{g} \cdot \text{s}^{-1}$ ].	66
5.9	Comparison of the maximum temperatures between Moltres-derived and the reference results. Temperature values expressed in [°C].	66
5.10	Mesh characteristics and maximum temperatures of the full-fuel column model.	66
5.11	Problem characteristics.	68
5.12	Comparison of this work and INL [57] first bottom core level average temperatures.	69
5.13	Comparison of this work and INL [57] first bottom core level average temperatures. Temperature values expressed in [°C].	71
5.14	Homogenization scheme.	73
5.15	Energy group condensation scheme.	73
6.1	Energy requirements of the different hydrogen ( $\text{H}_2$ ) production methods.	88
6.2	$\text{H}_2$ necessary to replace a gallon of fuel [133] [134].	89
6.3	$\text{H}_2$ requirement for MTD and UIUC fleets.	89
6.4	$\text{CO}_2$ savings in pounds per gallon of fuel burned [135].	90
6.5	$\text{CO}_2$ yearly savings.	90
6.6	Microreactor designs.	91

# List of Figures

1.1	Fort St. Vrain Generating Station.	2
1.2	Drawing of a TRISO fuel particle. Image reproduced from [7].	2
1.3	Gas turbine coupled to an HTGR. Image reproduced from [13].	3
3.1	MHTGR-350 reactor layout.	27
3.2	MHTGR-350 fuel assembly layout.	28
4.1	Comparison of different Serpent models of the fuel compact.	32
4.2	Relative error of the group constants generated with a homogeneous isotope distribution vs. explicit TRISO modeling.	33
4.3	Fuel column of the MHTGR-350. $xy$ -plane in the active core region.	34
4.4	Two energy group axial flux in the fuel column calculated with Serpent and Moltres.	37
4.5	Operational case 1: fuel column with no burnable poisons at 600K. Comparison of Serpent and Moltres-derived 3-group axial neutron fluxes.	39
4.6	Operational case 2: fuel column with no burnable poisons at 1200K. Comparison of Serpent and Moltres-derived 3-group axial neutron fluxes.	40
4.7	Operational case 3: fuel column with burnable poisons at 600K. Comparison of Serpent and Moltres-derived 3-group axial neutron fluxes.	40
4.8	Operational case 4: fuel column with burnable poisons at 1200K. Comparison of Serpent and Moltres-derived 3-group axial neutron fluxes.	40
4.9	$L_2$ -norm relative error for different number of energy group structures for the operational cases with no burnable poisons.	42
4.10	$L_2$ -norm relative error for different number of energy group structures for the operational cases with burnable poisons.	42
4.11	Computational time and memory requirements for different number of energy group structures.	43
4.12	MHTGR-350 full-core model layout.	45
4.13	Comparison of the MHTGR-350 radial power distribution at 600 K calculated by Serpent and Moltres.	46
4.14	Comparison of the MHTGR-350 radial power distribution at 1200 K calculated by Serpent and Moltres.	46
4.15	Axial view of the flux detector locations.	47
4.16	Comparison of the axial and radial fluxes calculated by Serpent and Moltres at 600 K.	48
4.17	Comparison of the axial and radial fluxes calculated by Serpent and Moltres at 1200 K.	48
4.18	Moltres model, 1/3 <sup>rd</sup> section of the MHTGR-350.	50
4.19	Comparison between the radially averaged axial power distribution calculated by Moltres and the benchmark published result [98].	51
4.20	Comparison between the axially averaged radial power distribution calculated by Moltres and the benchmark published result [98].	51
5.1	Model geometry axial layout.	56
5.2	Comparison of the analytical and numerical temperature profiles.	57
5.3	Axial layout of the model geometry.	57
5.4	Temperature-dependent material properties [27].	58
5.5	Unit cell temperature profile calculated by Moltres.	60

5.6	Model geometry axial layout.	60
5.7	Outlet plane temperature along the line A-B and line A-C.	62
5.8	Axial view of the full-fuel column model geometry.	66
5.9	Phase I Exercise 2 model geometry for simulation in Moltres.	68
5.10	Radial temperature at the bottom of the active core (z=200 cm) determined by Moltres.	69
5.11	Model geometry.	70
5.12	Axial temperatures determined by Moltres.	70
5.13	Axial view of the model geometry.	73
5.14	Flux profile comparison. F: thermal feedback, NF: no thermal feedback.	73
5.15	Temperature profile comparison. F: thermal feedback, NF: no thermal feedback.	74
5.16	Temperature distribution.	76
5.17	Flux profile comparison.	76
5.18	Temperature profile comparison.	77
6.1	Total US GHG emissions by economic sector in 2017. Image reproduced from [116].	80
6.2	The duck curve. Image reproduced from [119].	80
6.3	Energy required by HTE at 3.5 MPa.	84
6.4	Diagram of the Sulfur-Iodine Thermochemical process. Image reproduced from [127].	85
6.5	Energy required by the Sulfur-Iodine Thermochemical Cycle.	86
6.6	Diagram of a reactor coupled to a hydrogen plant.	87
6.7	Fuel consumption data of MTD and UIUC fleet.	89
6.8	$H_2$ requirement for MTD and UIUC fleets.	90
6.9	Hydrogen production rate by the different microreactor designs.	91
6.10	Prediction of the electricity generation in the US for 2050. Data from [139].	92
6.11	Prediction of the UIUC's net demand for 2050.	92
6.12	$H_2$ production.	93
6.13	Peak reduction by using the $H_2$ produced by the different production methods. $E_{LTE}$ , $E_{HTE}$ , and $E_{SI}$ are the generated electricity from the different method's hydrogen production.	94

# Chapter 1

## Introduction

This thesis studies Moltres' current capabilities for conducting multi-physics simulations of prismatic High-Temperature Gas-Cooled Reactors (HTGRs). This chapter introduces past and current developments in HTGR technology, discusses the motivation behind the development of this thesis, and summarizes the objectives of the following chapters.

### 1.1 The Prismatic High-Temperature Gas-Cooled Reactor

The history of prismatic HTGRs or simply Prismatic Modular Reactors (PMRs) began in the 1960s with the deployment of the Dragon reactor in the United Kingdom (UK) [1]. Its initial objective was to demonstrate the feasibility of HTGRs. The Dragon reactor experiment first operated in July 1965 and reached its full-power operation of 20 MWth in April 1966. The reactor operated for 11 years, demonstrating many components' successful operation and providing information on fuel and material irradiation. Simultaneously, interest in the United States (US) led to the 40 MWe HTGR Peach Bottom Unit 1. This reactor achieved initial criticality in March 1966 and went into commercial operation in June 1967. Peach Bottom Unit 1 demonstrated the HTGR concept by confirming the core physics calculations, verifying the design analysis methods, and providing a database for further design activities. Most importantly, the plant demonstrated that HTGRs could load follow [1]. After the deployment of these two demonstration reactors came the first HTGR prototype plant - the Fort St. Vrain Generating Station, shown in Figure 1.1a. Its electric power generation started in December 1976, reaching full-power operation in November 1981. The Fort St. Vrain plant generated 842 MWth to achieve a net output of 330 MWe. This reactor laid the foundation for future prismatic designs. Beginning with Fort St. Vrain, prismatic HTGRs in the US adopted as their fuel large hexagonal-shaped graphite elements with ceramic coated Tristructural Isotropic (TRISO) particles embedded within rods [1], displayed in Figure 1.1b.



The HTGR's most fundamental characteristic is its unique safety features. Radionuclide containment does not rely on active systems or operator actions. TRISO particles, pictured in Figure 1.2, play a significant role in this task. They consist of various layers acting as containment to limit radioactive product release. A TRISO particle is a

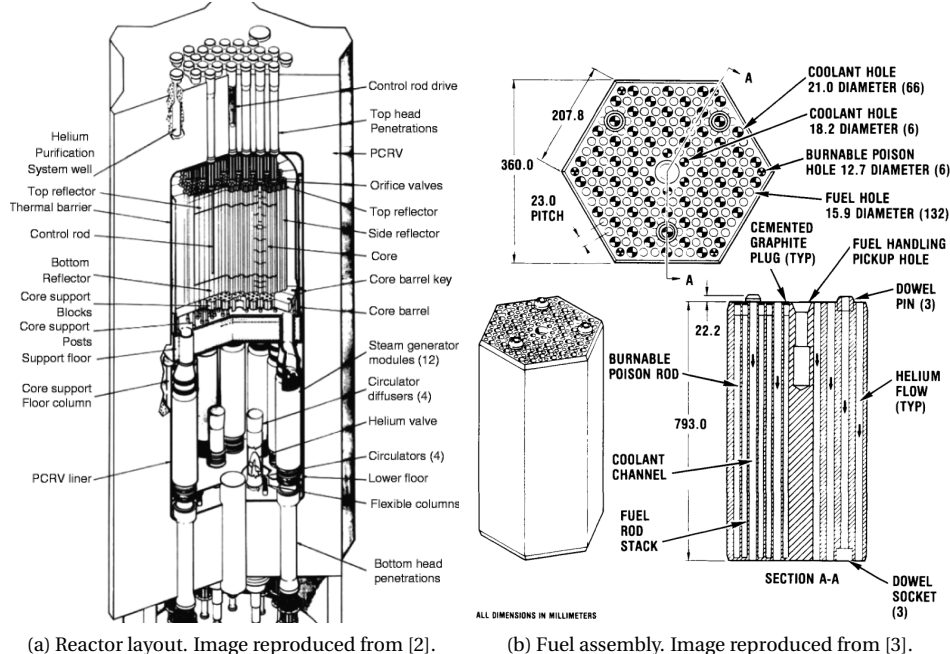


Figure 1.1: Fort St. Vrain Generating Station.

microsphere of about 0.8 mm in diameter. It includes a fuel kernel surrounded by a porous carbon layer (or buffer), followed successively by an inner pyrolytic carbon (IPyC) layer, a silicon carbide (SiC) layer, and an outer pyrolytic carbon (OPyC) layer. The buffer layer limits kernel migration and provides some retention of gas compounds [4]. The IPyC layer protects the kernel from chloride in the event of SiC decomposition and contributes to fission gas retention [5]. The SiC layer ensures the particle's structural integrity under constant pressure and helps retain non-gaseous fission products. The OPyC layer contributes to fission gas retention and protects the SiC layer during handling. As an additional advantage, TRISO particles increase the proliferation resistance of HTGRs. TRISO particles provide significant barriers and technical difficulties to retrieve materials from within the fuel coatings [6]. The particles can sustain high burnup, which causes the used nuclear fuel to have a low volume fraction of plutonium, making the fuel unsuitable for use in weapons [6].

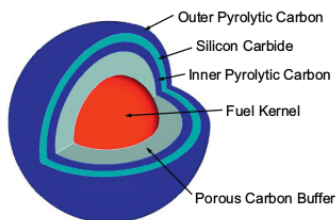


Figure 1.2: Drawing of a TRISO fuel particle. Image reproduced from [7].

Graphite is another contributor to the passive safety of the HTGR design. Combining ceramic fuel and a graphite

core structure permits high operating temperatures [8]. Graphite has a high heat capacity and maintains its strength at temperatures beyond 2760 °C. Moreover, HTGRs have an inherent negative temperature coefficient of reactivity. As a result, temperature changes in the core occur slowly and without damage to the core structure during transients.

HTGRs' higher operating temperatures offer increased thermal conversion efficiencies. The early HTGR designs converted their heat into electricity using the steam-Rankine cycle [9]. In such a system, the helium coolant passes through a steam generator, and the steam drives a turbine. This arrangement is around 38% efficient [10]. However, the steam cycle requires a steam generator and also a gas circulator [11]. This requirement increases the plant's capital cost, and it creates a risk of a water ingress event. The Brayton cycle is a better option because the helium coolant can directly drive a gas turbine in a closed cycle. Figure 1.3 exhibits an HTGR coupled to a gas turbine. A closed-cycle eliminates the need for a steam generator and a gas circulator. Additionally, it removes external sources of contamination of the nuclear circuit, reducing the need for on-line cleanup systems [12]. With the Brayton cycle, the system can achieve an energy conversion efficiency of around 48% [10].

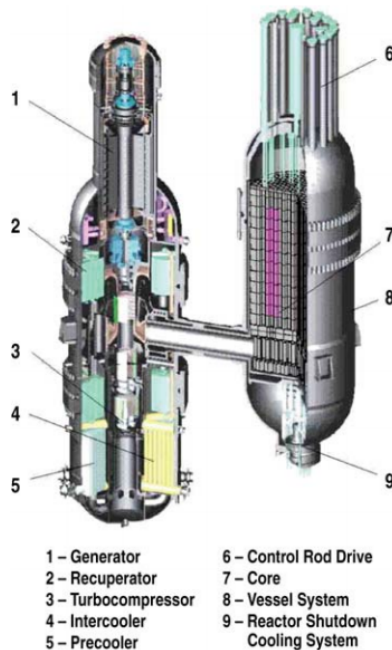


Figure 1.3: Gas turbine coupled to an HTGR. Image reproduced from [13].

HTGRs higher outlet temperatures and increased thermal conversion efficiencies enable a wide range of process heat applications, such as coal gasification processes, oil refinery processes, and production of synthesis gas, methanol, and hydrogen. Hydrogen offers a solution to energy and climate challenges, decarbonizing the transport and power sectors [14]. Several hydrogen production processes benefit from high temperatures, such as high-temperature electrolysis [15] or thermochemical water-splitting [16]. Utilizing the HTGR as the process's energy

source eliminates the need to burn fossil fuels to generate the steam those processes require [12].

In the early 1980s, Siemens/Interatom proposed the first modular type HTGR [1]. The modular HTGR design adds a low core power density to the safety features of HTGRs. A low core power density enables passive heat transfer mechanisms to remove the decay heat following postulated accidents [17]. These passive heat transfer mechanisms rely primarily on the natural processes of conduction, thermal radiation, and convection. This characteristic provides the modular HTGR the ability to cool down entirely without exceeding the failure temperature of the TRISO particles [1].

Under the sponsorship of the US Department of Energy (DOE), a team consisting of General Atomics, Combustion Engineering, General Electric, Bechtel National, Stone & Webster Engineering, and Oak Ridge National Laboratory (ORNL) developed the Modular High-Temperature Gas-Cooled Reactor (MHTGR)-350 [17] [18]. They designed the basic module to deliver superheated steam at 17.3 MPa and 538 °C. Based on both economic and technological considerations, the optimal configuration was a 350 MWth reactor with an annular core. The team completed in 1986 the preliminary safety information document for the MHTGR-350 and the complete draft pre-application in 1989 [19]. 

The MHTGR concept formed the basis for the Gas Turbine-Modular Helium Reactor (GT-MHR) reactor design. Renewed interest in HTGRs in the US resulted in the GT-MHR development program beginning in 1993. General Atomics (US) and MINATOM (Russia) a cooperation agreement to develop a prototype reactor. FRAMATOME and Fuji Electric joined the program in 1996 and 1997, respectively. The final conceptual design was a 600 MWth/293MWe plant to burn weapons plutonium and the long term goal of commercial deployment.

In 1987, the Japanese Atomic Energy Commission proposed constructing the High-Temperature engineering Test Reactor (HTTR), a prismatic block type core structure with a power rating of 30 MWth [12]. The Japanese government approved proceeding with the HTTR in 1989, and construction began in March 1991. The reactor reached first criticality in 1998 and full power  001. The HTTR has two operational modes, for which the outlet coolant temperatures are 850 and 950 °C. The HTTR program evaluated six major categories of the HTGR concept: safety, thermal-fluids, fuel, high-temperature components, core physics, and control/instrumentation. With the HTTR program, the Japanese Atomic Energy Agency established a database of operation and maintenance experience. The HTTR program aims to share the information in the database with the design, construction, and operation of future HTGRs. 

In the early 2000s, the Generation IV Roadmap project [20] identified reactor concepts that could meet the future's energy demands in an efficient, economical, and environmentally safe manner [21]. One of these reactor concepts is the Very High-Temperature Gas-Cooled Reactor (VHTR). A VHTR is a type of HTGR whose core outlet temperatures are between 700 and 950 °C [22]. The DOE selected this reactor concept for the Next Generation

Nuclear Power (NGNP) Project. This project intended to demonstrate emissions-free nuclear-assisted electricity and hydrogen production by 2015.

In addition to government-sponsored research, several privately funded gas reactor projects are underway. StarCore Nuclear [23] (Canada) is developing a 50 MWth HTGR that will produce electricity (20 MWe) and thermal energy (10 MWth) for use in process heat applications. Ultra Safe Nuclear Corporation (USNC)(US) [24] is developing the Micro Modular Reactor (MMR), a 15 or 30 MWth HTGR. The MMR Energy System works as a stand-alone power plant, as part of microgrids, or to provide process heat for industrial applications [25]. USNC has partnered with Ontario Power Generation, Idaho National Laboratory (INL), and the University of Illinois at Urbana-Champaign (UIUC). Through these partnerships, USNC proposes to deploy its MMR at sites in Ontario, Idaho, and Illinois.

## 1.2 Motivation

This work's ultimate goal is to support the development of the HTGR concept. As the last section described, HTGRs have several favorable characteristics that make them the right candidate for large scale deployment in the near term. For example, some microreactor designs embody this type of reactor technology and may be operational before 2030.

More specifically, this work develops computational methods for modeling prismatic HTGRs with *Moltres* [26]. Modeling and prediction of core thermal-fluid behavior are necessary for assessing the safety characteristics of a reactor. Determining the temperature inside a reactor, for both normal and transient operation, is of paramount importance as several materials' integrity depends on it. Most importantly, undesirably high temperatures endanger the TRISO particles' integrity and, consequently, jeopardize the fission product containment [27]. Furthermore, the complex fuel block geometry requires numerical calculations for obtaining the fuel temperatures.

The characteristics of an HTGR are different from those of conventional Light Water Reactors (LWRs). Such differences demand reactor analysis tools that capture the following peculiarities of HTGRs [28][29]:

- Double heterogeneity: the TRISO particles form the first heterogeneity level, consisting of four layers. The second level arises from the fuel elements, as they encompass the compacts, the coolant, and the moderator.
- Strong temperature dependence: the fuel temperature has a significant effect on the neutron spectrum and the transient feedbacks.
- High-temperature gradients: the temperature difference between the fuel and the moderator is large during transients. Large temperature gradients translate into large thermal stresses in the reactor structures.
- Large time-scale variation: the coolant's low heat capacity causes short transients while the large heat capacity

of the graphite structures causes long ones.

Historically, linking stand-alone neutronics solver to a thermal-fluid solver allowed for simulating an entire reactor. The programs' connection occurred in a loose-coupling fashion, such that one program's output served as the other's input and vice versa. This coupling technique is commonly known as the operator-splitting technique [30]. In such an approach, each program uses a physical model that solves some of the problem variables while assuming constant the rest of them. Nonetheless, these physical models describe processes that rely heavily on the solution of one another's. The neutron flux determines the power distribution, and the power distribution strongly influences the temperature field. Due to the temperature feedback, the temperature affects the neutron flux distribution in the core. Because of a strong temperature coefficient of reactivity present in HTGRs, multi-physics transient simulations coupled via the operator-splitting approach may introduce significant numerical errors [31][30].

Multi-physics Object-Oriented Simulation Environment (MOOSE) [32] is a computational framework targeted at solving fully coupled systems. Additionally, MOOSE facilitates relatively easy coupling between separate phenomena and allows for great flexibility, even with a large variance in time scales [33].

*Moltres* is an open-source, Finite Element Method (FEM) application built within the MOOSE framework. Moltres solves arbitrary-group neutron diffusion, delayed neutron precursor concentration, and temperature governing equations. These characteristics, plus some modifications that this work intends to implement, make Moltres suitable for solving the type of physical phenomena described above.

### 1.3 Objectives

As mentioned earlier, the ultimate goal of this work is to support the development of HTGR technology. The following list of main objectives expands on that goal.

**Determine prismatic HTGRs essential physics.** Prismatic HTGRs have inherent physics phenomena unique to their design. This thesis intends to determine which are those inherent physics crucial for their accurate modeling.

**Extend Moltres modeling capabilities to prismatic HTGRs.** Moltres is a multi-physics solver designed to capture critical physics in Molten Salt Reactors (MSRs). Moltres' current capabilities allow for solving some of the physics in the prismatic HTGR design. Nevertheless, the solver needs to capture the missing physics in prismatic HTGRs and adequately integrate them into the current capabilities.

**Understand HTGRs' contribution to stopping climate change.** HTGRs are an attractive technology due to attaining high temperatures and high thermal conversion efficiencies. These features yield a high hydrogen production efficiency, which can potentially ease climate change.

The main objectives are somewhat broad. The following list presents secondary objectives which will lead to the fulfillment of the main objectives:

**Demonstrate Moltres' ability to predict HTGR neutronics.** A neutronics solver should predict the flux shape and magnitude accurately during steady-state and transient simulations. Previous work demonstrated Moltres' ability to solve MSR neutronics. Chapter 4 illustrates such a capability for prismatic HTGRs.

**Understand the impact of the energy group structure on the HTGR diffusion calculations.** The underlying physics of HTGRs differs from the physics of other reactors. Consequently, the simulation results will be sensitive to different parameters from other reactor type simulations. Chapter 4 studies the impact of the energy group structure of the group constants on the diffusion calculations.

**Calculate power distribution correctly.** The power distribution is the most influential parameter over the thermal-fluids as it determines the temperature profile in the reactor. Previous work demonstrated Moltres' ability to calculate the power distribution in MSRs. Chapter 4 evinces such an ability for prismatic HTGRs.

**Predict the prismatic HTGRs temperature profile accurately.** Undesirably high temperatures endanger the integrity of the reactor structures, and most importantly, the TRISO particles. Additionally, the temperature influences the neutronics. Hence, a neutronics calculation will be inaccurate without a correct thermal-fluids calculation. Previous work demonstrated Moltres' ability to predict the temperature distribution in MSRs. Chapter 5 examines Moltres' ability to predict the temperature distribution in prismatic HTGRs accurately.

**Conduct coupled simulations of prismatic HTGRs.** An accurate simulation of prismatic HTGRs requires integrating the neutronics and the thermal-fluids through the modeling of the thermal feedback. Previous work demonstrated Moltres' ability to calculate thermal feedback in MSRs. Chapter 5 examines Moltres' capabilities for calculating the thermal feedback in prismatic HTGRs.

**Technical analysis of hydrogen production with HTGRs.** High temperatures enable high-efficiency hydrogen production methods. Most of them have different energy requirements and production rates. Chapter 6 analyses such quantities.

# **Chapter 2**

## **Literature Review**

This chapter summarizes previous efforts in numerical simulations of prismatic HTGRs. The simulation of prismatic HTGRs require the coupled modeling of the neutronics and thermal-fluid phenomena. This chapter comprehends the following sections: Section 2.1 addresses diffusion methods for solving the neutronics, Section 2.2 focuses on the thermal-fluids, and Section 2.3 studies the coupled simulations.

### **2.1 Prismatic HTGR Diffusion Solvers**

Currently, several software programs solve the neutronics of prismatic HTGRs. Most of these programs rely on one of the following methods: stochastic transport (Monte Carlo), deterministic transport, or deterministic diffusion. This section focuses on the last class.

The history of deterministic diffusion solvers began in the late 1950s with the Finite Difference Method (FDM) application to the analysis of LWRs. In FDM, mesh spacings are usually of the order of the diffusion length. While solving large multi-dimensional problems, this feature causes the mesh points to reach intractable numbers [34]. The computational expense of these calculations motivated the generation of more computationally efficient techniques [35]. Although substantial overlaps exist, the most common techniques fall into two broad categories: nodal methods and FEM.

FLARE [36] is a three-dimensional Boiling Water Reactor (BWR) simulator, and it is representative of the first generation of nodal methods. This approach used adjusted parameters to match actual operating data or the results of more accurate calculations. Most of these methods were implementations of the so-called "1.5 group theory" [37]. The second generation of nodal methods derived spatial coupling relationships by applying the transverse integration procedure (TIP). This procedure obtains equivalent one-dimensional equations by integrating the multi-dimensional diffusion equation over directions transverse to each coordinate axis [35]. This approach proved to be highly efficient and accurate in Cartesian geometries.

In 1981, a formulation based on the Nodal Expansion Method (NEM) first demonstrated the feasibility of nodal methods in hexagonal geometries [38]. However, this method would introduce non-physical singular terms that

required the utilization of discontinuous polynomials. This drawback motivated the development of more effective formulations. HEXNOD, introduced in 1988 by Wagner [39], is an example of such formulations. This algorithm uses the TIP and, in contrast to the NEM, solves the resulting differential equation analytically. Wagner's article demonstrated the method's good accuracy by comparing to FDM and Monte Carlo calculations for a few benchmark problems.

HEXPEDITE [40] introduced a new method that is another example of more effective formulations. HEXPEDITE uses the TIP formulation to derive a pseudo-one-dimensional equation. The resulting differential equation is solved analytically. The difference from HEXNOD is that HEXPEDITE uses a simpler and more efficient coupling scheme. Different works [40][41] on the HEXPEDITE methodology tested the approach against the NEM and the FDM. These studies established HEXPEDITE's superiority in terms of accuracy and runtime. HEXPEDITE's use prevailed in the analysis of HTGRs until recently. In 2010, INL conducted a study [42] in which they compared HEXPEDITE's results against several diffusion solvers, as well as the Monte Carlo solvers MCNP5 [43] and Serpent [44].

DIF3D [45] and PARCS [46] are other examples of prevalent nodal diffusion tools. DIF3D has several solution options, such as the diffusion FDM, diffusion NEM based on TIP, and the VARIANT nodal transport method. PARCS has several solution options as well, such as  diffusion FDM, diffusion NEM based on TIP,   $P_N$  transport methods, and the multi-group transport simplified  $P_3$  with FDM and NEM discretizations.

Nodal methods solve relatively coarse meshes for approximate solutions. This characteristic makes the process efficient.  On the other hand, the method does not provide detailed point-wise accurate solutions [47]. Additionally, the derivation of nodal methods happens in a specific coordinate system for a particular node shape.  The application to complex problems is not flexible as different geometries require customized configurations.  This lack of flexibility limits the applications of nodal methods to regular geometries only. 

The FEM is a well-established method in applied mathematics and engineering. FEM is a numerical technique for finding approximate solutions to partial differential equations by deriving their weak or variational form. Most applications make FEM preferable due to its flexibility in the treatment of curved or irregular geometries. Also, the use of high order elements attains higher rates of convergence [48]. The first engineering application of FEM was in the field of structural engineering, dating back to 1956. In successive years, FEM became the most extensively used technique in almost every branch of engineering. FEMs have several advantages over the nodal methods. It provides flexibility in the geometry definition, a firm mathematical basis, ease in extension to the multi-group application,  and detailed point-wise accurate solutions [49].

In 1973, Kang et al. [47] described the first application of FEM to neutron diffusion theory. The fundamental motivation for this development was the impractical application of the FDM to three-dimensional problems. In this early work, the author compared different FEM approaches to the FDM in one-dimensional and two-dimensional

problems. The studies showed a higher order of convergence achieved by the FEM. Throughout the last four decades, many software programs utilized the FEM to solve the diffusion equation. Some of the most recent software for diffusion simulations are CRONOS2 [50], Core Analyzer for Pebble and Prism type VHTRs (CAPP) [51], and Rattlesnake [52]. The list of FEM diffusion solvers is more extensive, but this thesis focuses on the best-documented software in the open literature.

Commissariat a l'Energie Atomique (CEA) developed CRONOS2 [50] as part of the SAPHYR system. CRONOS2 conducts steady-state and transient multi-group calculations, based on the diffusion equation or the transport equation using the  $S_N$  method and an FDM or a FEM discretization. In 2008, Damian et al. [53] presented the code suite NEPTHIS[54]/CAST3M[55], software that relied on CRONOS2. Section 2.3 describes further the coupling scheme.

In 2008, the Korea Atomic Energy Research Institute (KAERI) published an article [49] that presented CAPP. Its purposes are to conduct steady-state core physics analysis, core depletion analysis, and core transient analysis. The article validated the software with two benchmark problems: the IAEA PWR benchmark problem, and Phase I Exercise 1 of the OECD/NEA PBMR-400 Benchmark [56]. In 2011, Lee et al. published an article [51] that extended CAPP's functionalities to prismatic HTGRs. To validate CAPP, they had to integrate a simplified thermal-fluids tool into the software. Section 2.3 describes the thermal-fluids tool and the coupling scheme.

RattleSnake [52] is the MOOSE [32] based application for simulating the transport equation. INL had initially developed Pronghorn [33] to model Pebble Bed Modular Reactors (PBMRs) [57]. The MOOSE neutronics kernel library Yak incorporated the neutron diffusion models initially in Pronghorn. Currently, RattleSnake is the primary tool for solving the linearized Boltzmann neutron transport equation within MOOSE and relies heavily on Yak. Various solvers are available under RattleSnake, including low-order multi-group diffusion, spherical harmonics transport, and discrete ordinates transport, all solved with the FEM.

In 2013, INL conducted the OECD/NEA MHTGR-350 Benchmark [4][57] without further simplifications. The INL team solved Phase I Exercise 1 using INSTANT-P1 [58], Pronghorn, and RattleSnake. INSTANT-P1 is a transport solver that relies on the spherical harmonics discretization of angles. The results for Pronghorn and RattleSnake were identical, and all presented results exhibited good agreement with the benchmark results.

### 2.1.1 Energy group structure analysis

In the context of this thesis, Moltres uses homogenized group constants previously generated by neutron transport solvers. The choice of the energy group structure for the group constant homogenization affects the diffusion calculation accuracy. The longer neutron mean free path in HTGRs compared to LWR increases the spectral interactions between elements. For this reason, HTGR analyses require more energy groups than conventional LWR

analyses. This section summarizes previous studies on the impact of the energy group structure over the diffusion calculations.

Argonne National Laboratory (ANL) directed a study [59] to compare the accuracy of nodal diffusion calculations employing different energy group structures. The group constant homogenization used the DRAGON neutron transport solver, and the diffusion calculations utilized the application DIF3D. For the study, the ANL team implemented a one-dimensional fuel-reflector model in which they compared the solution accuracy using 4, 7, 8, 14, and 23 energy groups. They also used alternative energy group structures for the same number of groups. For simplicity, the authors used the homogenized fuel compact model and generated all the group constant at 300 K. One of their conclusions was that the number of energy groups should be more than four, and more than six would be sufficient for uranium fueled HTGRs. Another finding was that the accuracy of the diffusion calculation is sensitive to the energy group boundaries. 

Han's MS thesis [60] focused on selecting energy groups for the reactor analysis of the PBMR. The author used COMBINE6 [61] for group constant generation and the Penn State nodal diffusion tool NEM [62] for the reactor analysis. The author compared the results against MCNP5 reference results. To simplify the setup, the model used uniformly distributed isotopes in the fuel. The study performed the calculations at 300 and 1000 K. To arrive at an optimal group structure, the author compared many combinations of group structures using a trial and error strategy. One conclusion of this work agrees with the previous bibliography [63] [64] in that the energy spectrum is critical to yield an accurate description of a nuclear reactor using a few groups.

ANL's study helps set up proper nodal diffusion calculations for an HTGR. ANL's team conducted the study at 300 K — not in the operational range of any HTGRs. On the contrary, Han's thesis included an analysis at 1000 K, and his results showed that the temperature changes have a non-negligible impact. Additionally, ANL's study used the simplified model of the homogenized fuel compact. Han highlighted that homogenized fuel models of the PBMR underestimate criticality calculations. In 2015, INL presented their results [65] for an International Atomic Energy Agency (IAEA) coordinated research project [66] and showed that the homogenization of the compact material notably underestimates the multiplication factor. On the other hand, the open literature has not widely investigated the impact of such simplification over the homogenized group constants.

### 2.1.2 Summary of Prismatic HTGR Diffusion Solvers

Section 2.1 introduced several deterministic diffusion classes, including FDM, nodal methods, and FEM. The fundamental motivation for the development of nodal methods and FEM was the impractical application of the FDM to three-dimensional problems. Section 2.1 also discussed the main characteristics of these methods, directing the reader's attention to the advantages of the FEM. Although nodal methods are efficient, most applications make

FEMs preferable due to their flexibility in the treatment of irregular geometries. Additionally, FEMs have a firm mathematical basis, its formulation eases the extension to multi-group applications. Moltres relies on the FEM, counting with all the advantages of the method.

Section 2.1 summarized previous efforts in deterministic diffusion solvers of prismatic HTGRs. This thesis draws two main conclusions from those earlier efforts. The first conclusion is that several authors validated their solvers by comparison to other tools. In the context of this thesis, Chapter 4 describes two exercises: first, a comparison between Moltres and Serpent-derived results, and second, a comparison between Phase I Exercise 1 of the OECD/NEA MHTGR-350 Benchmark results calculated by Moltres and the exercise's published results. The second conclusion is that several prismatic HTGRs count with an integrated thermal-fluids solver. Due to strong thermal feedback, modeling prismatic HTGRs with Moltres requires incorporating a thermal-fluids solver. Section 2.2 discusses previous work in the thermal-fluids modeling of prismatic HTGRs.

Section 2.1.1 outlined the importance of the right choice of energy group structure for group constant homogenization. Diffusion calculations use homogenized group constants previously generated by neutron transport solvers. Previous studies focused on nodal diffusion calculations of HTGRs. Although further analyses can extrapolate those studies' conclusions to FEM diffusion calculations, such an analysis might be valuable to this thesis. Chapter 4 studies the accuracy of Moltres diffusion calculations for multiple energy group structures.

## 2.2 Prismatic HTGR Thermal-fluids

This section of the literature review summarizes previous work on the thermal-fluids modeling of prismatic HTGRs. Thermal-fluid calculations enable the correct design of HTGRs. Predicting the maximum fuel temperature at steady-state is of paramount importance to succeed in that task. I emphasize this statement in the case that hydrogen production is desirable, as that process requires higher coolant temperatures, leading to high fuel and reactor vessel temperatures. This literature review analyzed several approaches that helped to choose a thermal-fluids model to implement in Moltres simulations.

The complex geometry of the hexagonal fuel assembly requires numerical calculations for obtaining accurate evaluations. Thermal-fluids studies for early HTGRs consisted mainly of support calculations for Nuclear Regulatory Commission (NRC) safety analysis reports. The analyses employed sets of independent solvers that relied on simplified approximations. Simplified models help understand some fundamental aspects of prismatic HTGRs and have the advantage of reducing the computational expense of the calculations.

General Atomics [67] developed the first set of software libraries that relied on simplified approximations. The following list introduces and summarizes some of these and their features:

- FLAC: It determines the coolant flow distribution in the coolant channels and gaps. It solves the one-dimensional momentum equation for incompressible flow and the continuity equations for mass and energy.
- POKE: It determines the coolant mass flow, coolant temperature, and fuel temperature distribution. It solves the steady-state mass and momentum conservation equations for parallel channels.
- DEMISE: It determines the steady-state three-dimensional temperature distribution in a standard element. It solves the temperature in a network model.
- TAC2D: It is a general-purpose thermal analysis software. It solves the two-dimensional heat conduction equation.

Several studies have used these software programs. For example, INL conducted in 2003 a design study [21] in support of the NGNP project. The authors conducted several parametric studies on the GT-MHR [68], with the objective of increasing the coolant temperature. Using POKE and TAC2D, they evaluated three major design modifications: reducing the bypass flow, controlling the inlet coolant flow distribution, and increasing the reactor's height.

This thesis differentiates the *flow network*, *equivalent cylindrical*, and *unit cell* models among the simplified approaches. The flow network model treats the coolant flow paths in the core as a cross-connected flow network [67]. Constant pressure nodes connected to flow branches make up the network. The model uses the one-dimensional conservation equations to solve the pressure loss and coolant temperature in each network node. The equivalent cylinder model uses a geometrically simpler one-dimensional or two-dimensional design model [67][27]. The unit cell model divides the fuel blocks into triangular-shaped unit cells. The model assumes that the coolant removes all the heat generated in the cell [27].

Using the flow network analysis tool RELAP5-3D/ATHENA [69], Reza et al. [70] conducted a thermal-fluids study of the GT-MHR. Reza et al. increased the reactor outlet temperature to enable hydrogen production. Additionally, they evaluated alternative inlet coolant flow configurations in an attempt to reduce the reactor vessel temperatures. After finding an optimal configuration, they assessed the fuel and the reactor vessel's maximum temperatures during the low-pressure conduction cool-down (LPCC) and the high-pressure conduction cool-down (HPCC) events.

An example of an application using the equivalent cylindrical approach is GAMMA [71][72], a system thermal-fluids analysis tool. GAMMA's primary motivation is simulating the air ingress event following a LOCA. Following the depressurization of helium in the core, air could enter the core through the break and oxidize the in-core graphite structure. Graphite oxidation is an exothermic chemical reaction and, thus, it is a significant concern. GAMMA solves heat conduction, fluid flow, chemical reactions, and multi-component molecular diffusion. Together with a multi-dimensional analysis feature, GAMMA has a one-dimensional analysis capability for modeling a flow network.

Takada et al. [73] carried out another study using the flow network and the equivalent cylindrical model. They developed a thermal-fluids design tool for modeling the HTTR. This tool used the flow network analysis software FLOWNET [74] for calculating the coolant flow and temperature distributions. TEMDIM [74] solved the fuel temperatures using the equivalent cylindrical model. Finally, the authors validated the calculation scheme by comparing its results with the experimental data from the HTTR.

Nakano et al. [75] studied different fuel assembly configurations using several simplified approximations. The authors used FLOWNET and TAC2D for determining the flow distribution and fuel temperature. The fuel temperature calculation used the equivalent cylindrical model of a unit cell. However, the unit cell's asymmetry makes the temperature distribution asymmetric in the graphite block, behavior that the equivalent cylindrical model fails to capture.

In 2006, In et al. [76] conducted a more detailed analysis using a three-dimensional model of the unit cell in the hot-spot of the GT-MHR 600, spot in the core with the largest power density. The study predicted the maximum fuel temperature at steady-state at the end of the equilibrium cycle. The computational fluid dynamics (CFD) software CFX 10 [77] calculated the three-dimensional temperature profile. The results showed that the maximum fuel temperature surpassed the design limits, so the authors proposed decreasing the power density or the axial power peak as countermeasures.

To recapitulate, previous work used simplified approaches to evaluate different aspects of prismatic HTGRs. Some of those evaluations include thermal-fluids design, analysis of alternative coolant flow configurations, and accident analysis. Such simplified approaches are helpful to understand essential aspects of prismatic HTGRs but may yield inaccurate temperature distributions [27]. More detailed thermal-fluids evaluations were rare in the open literature until the last 15 years. This thesis summarizes some of those evaluations down below.

In 2008, an article by Tak et al. [27] conducted a three-dimensional CFD analysis of a fuel column of the PMR600, a pre-conceptual reactor designed by KAERI whose reference design is the GT-MHR. The commercial software CFX 11 [78] performed the calculations. The study considered a  $1/12^{th}$  section of the fuel due to its symmetry. Using the one-dimensional thermal-fluid equations, the model determined the coolant distribution, which served as input to CFX. However, the friction in the channels is dependent on the viscosity, which is highly dependent on the temperature. Therefore, obtaining the mass flow rates from a separate solver may introduce errors [79].

Another article [79] studied a  $1/12^{th}$  section of the fuel column of the GT-MHR with the commercial tool FLUENT [80]. The authors conducted parametric studies of several factors, such as bypass-gap width, turbulence model, axial heat generation profile, and geometry changes due to irradiation. In this study, FLUENT obtained the coolant distribution as part of the solution. Their most relevant results showed that the bypass flow caused a large lateral temperature gradient in the block. Large temperature gradients cause excessive thermal stresses, which raise

potential structural issues.

Despite the recent developments in CFD tools, a detailed full-core analysis of prismatic HTGRs still requires a tremendous computational expense. This requirement is mostly due to the three-dimensional CFD modeling of the coolant flow. This drawback motivated the implementation of simplified methods that reduce the computational time and memory requirements while maintaining accurate results. Such methods combine the accuracy from CFD tools and the light computational expense of system analysis approaches.

Cioni et al. [81] presented an article in 2005 in which they conducted three-dimensional simulations of HTGR fuel assemblies. The study's objective was to investigate the blockage of cooling channels in the core. They used the thermal-fluids tool Trio\_U [82] to carry out the calculations. The numerical scheme solved the three-dimensional conduction equation in the solid coupled to the coolant's one-dimensional thermal-fluid equations. The one-dimensional thermal-fluid approximation does not resolve the boundary layer avoiding finer meshes near the walls as well as turbulence conservation equations [83]. Their results showed that the blockage increased the blocked fuel assembly's temperature only and did not affect the surrounding elements due to the bypass flow. This study proves the importance of the modeling of the bypass flow.

Travis et al. [84] presented a comparison between a simplified method and detailed CFD simulations. Their method solved the three-dimensional heat conduction equation in the solid and the one-dimensional thermal-fluid equations in the coolant channels. The method's validation analyzed a fuel column and compared the results to those of a three-dimensional CFD simulation using the commercial software STAR-CCM+ [85]. Their simplified scheme reduced the computation time to 2.5% of the CFD simulation time. Overall, the method showed good accuracy and less than a 2% difference to the CFD simulation.

Simoneau et al. [86] analyzed the transient behavior of an HTGR during the depressurized conduction cool-down (DCC) and HPCC event. The CFD tool STAR-CD [87] performed the calculations using the porous media model [88] to accommodate the different spatial scales. STAR-CD solved the conductive, convective, and radiation heat transfer in a  $1/12^{th}$ -section of the core and reactor vessel.

Tak et al. [89] [83] developed the thermal-fluids tool CORONA. CORONA solves the three-dimensional heat conduction equation in the solid and the one-dimensional thermal-fluid equations in the coolant. To validate CORONA, the authors analyzed a fuel column and compared their results against the CFD tool CFX and experimental results. The validation results showed that CORONA provided reasonably accurate results.

### 2.2.1 Summary of Prismatic HTGR Thermal-fluids

Section 2.2 summarizes previous work on the thermal-fluids modeling of prismatic HTGRs. Early studies relied on simplified approximations to carry out the simulations. These approaches may yield inaccurate temperature

distributions requiring more accurate methods, such as CFD techniques. Although CFD techniques compute detailed temperature profiles, their fine mesh requirement restricts the use of such methods to studies of the local behavior of a fuel column. However, a whole-core thermal analysis has many advantages over local models. In general, the problem set up includes more accurate boundary conditions. For example, without whole-core modeling, the local models' mass flow distributions are average values of the core flow rate instead of their exact value [90]. This simplification leads to under-predicted fuel temperatures for the assemblies with a lower flow rate than the average. Additionally, a coupled analysis with a reactor physics tool requires a full-core model [89]. An alternative for an explicit whole-core analysis are approaches that combine the accuracy from CFD tools and the light computational expense of system analysis applications.

CFD analyses' high computational expense is mostly due to the three-dimensional CFD simulation of the coolant flow [84]. Section 2.2 presents two alternatives: the porous media model or the combination of the three-dimensional heat conduction equation for the solid structures to the one-dimensional thermal-fluid conservation equations for the coolant. Due to the more extensive use of the second alternative in the open literature, this thesis focuses on it. Chapter 5 studies the implementation of this alternative in Moltres for studying the thermal-fluids of prismatic HTGRs.

## 2.3 Prismatic HTGR Multi-physics

Historically, stand-alone simulations have solved the neutronics and thermal-fluids of HTGRs separately. Nonetheless, these physical phenomena rely heavily on one another. Hence, a coupled analysis is necessary to consider the interaction between the neutronics and thermal-fluids behavior [91].

In 2008, Damian et al. [53] studied the passive safety features of a prismatic HTGR using the coupled software NEPTHIS/CAST3M[54][55]. The study analyzed a three-dimensional core model using the software libraries NEPTHIS and CAST3M/Arcturus for calculating the neutronics and the thermal-fluids, respectively. NEPTHIS used a transport-diffusion calculation scheme that relied on the transport application APOLLO2 [92] and the diffusion application CRONOS2. CAST3M/Arcturus solved the thermal-fluids using the porous media model. The authors conducted several parametric studies, including the variation of the bypass flow, the average power density, the core geometry, and fuel loading strategy.

In 2011, Lee et al. published an article [51] in which they extended the functionalities of CAPP to prismatic HTGRs. To consider the thermal feedback, the authors integrated into CAPP a simplified thermal-fluids tool based on Stansby's approach [93]. This approach uses different length scale models to solve the temperature distribution. The model divided a fuel column into six triangular prisms, each of them hosting a representative coolant channel, to

calculate the axial coolant temperature distribution. The coolant temperature served as input to a two-dimensional conduction model that solved the moderator and fuel compact temperatures. Through a TRISO particle conduction model, the model obtained the fuel temperature. Finally, a three-dimensional conduction model based on the FDM calculated the reflector temperature. To validate this model, the authors solved a two-dimensional model of the PMR-200 and compared the results against HELIOS [94].

Tak et al. [91] coupled CAPP and GAMMA+. GAMMA uses the one-dimensional form of the mass, momentum, energy, and species conservation equations to solve the fluid's flow and temperature distribution. For solids, it uses three different models: (1) heat conduction model of a TRISO particle, (2) implicit coupling to consider the heat exchange between a fuel compact and TRISO particle, and (3) multi-dimensional heat conduction model of the hexagonal fuel and reflector blocks. In this study, the authors applied the coupled software to study the steady-state performance of the PMR-200. Some of their most relevant results revealed that neglecting the bypass flow decreased the active core temperatures; consequently, the multiplication factor increased by approximately 300 pcm. These results prove the importance of the right modeling of the thermal-fluids in coupled simulations of prismatic HTGRs.

A recent article by Yuk et al. [95] added to CAPP the capability to conduct transient analyses. This capability solved the time-dependent neutron diffusion equation with the FEM. The primary motivation behind this feature was to perform reactivity insertion accident simulations. To take into account the thermal feedback, the authors developed a simplified thermal-fluids analysis tool based on Stansby's approach. To test the new transient capabilities, they analyzed two control rod ejection scenarios and compared the results to those of CAPP/GAMMA+.

The prismatic HTGR simulation tools available have lagged behind tools and methods developed for LWRs. The evolution of HTGR technology demands the development of more accurate and efficient simulation tools. Additionally, the definition of appropriate benchmarks is essential to compare various tools' capabilities. In 2012, the Organisation for Economic Co-operation and Development (OECD)/Nuclear Energy Agency (NEA) defined a benchmark for the MHTGR-350 MW reactor [4]. The purpose of this benchmarking exercise is to compare various reactor physics and thermal-fluid analysis methods. The MHTGR-350 design serves as a basis for this benchmark. The scope of the benchmark is twofold: (1) to establish a well-defined problem, based on a common given data set, to compare methods and tools in core simulation and thermal-fluid analysis, and (2) to test the depletion capabilities of various lattice physics tools available for prismatic HTGRs. Section 3.3 describes the benchmark in more detail.

In 2012, INL published a study [96] that coupled Pronghorn and RELAP-7 [97]. Pronghorn solved the coupled equations defining the neutron diffusion, fluid flow, and heat transfer in a three-dimensional model of the core. RELAP-7 is a MOOSE-based system application and simulated the plant system layout, including the hot and cold ducts, the helium circulator, and the steam generator. It solved the one-dimensional continuity, momentum, and

energy equations for a compressible fluid. To test the coupling, INL's team carried out the OECD/NEA MHTGR-350 Benchmark [98]. The original benchmark provides a set of 26 neutron energy group and temperature-dependent cross-sections. To simplify the debugging, the authors collapsed the 26 groups into two groups. Although using two groups reduces the model's accuracy, the lower number of groups decreases the calculation time by at least a factor of ten. In their study, a two-dimensional cylindrical model replaced the three-dimensional geometry defined by the benchmark. The integrated system testing included two stages: (1) both stand-alone tools underwent several convergence studies, and (2) the integrated system solved the steady-state problem in an integrated manner. The authors concluded that the coupling between Pronghorn and RELAP-7 was successful.

Tak et al. [99] developed a neutronics/thermal-fluids coupled software using DeCART [100] and CORONA. DeCART is a whole-core neutron transport tool, and it was responsible for calculating the power distribution and the fast neutron fluence. CORONA calculated the temperature distribution. The authors conducted the OECD/NEA MHTGR-350 benchmark to validate their software and identify technical challenges for future development. The authors presented an interesting analysis in which they compared the coupled simulation results and the stand-alone simulations. The difference in the multiplication factor was as high as 2597 pcm. The axial offset and maximum fuel temperature exhibited significant differences as well. This study highlights the importance of the integration of neutronics and thermal-fluid solvers for simulating prismatic HTGRs.

Sensitivity analysis and uncertainty analysis methods assess the predictive capabilities of coupled neutronics/thermal-fluids simulations. In 2013, the IAEA launched a coordinated research project [66] on the HTGR Uncertainty Analysis in Modeling. The coordinated research project's objective was to determine the uncertainty in HTGR calculations at all stages of coupled reactor physics/thermal-fluids and depletion calculations. This coordinated research project is a natural continuation of the previous IAEA and OECD/NEA international activities [101][56] on Verification and Validation of available HTGR simulator capabilities. The technical approach is to establish and utilize a benchmark for uncertainty analysis. The benchmark defines a series of well-defined problems with complete sets of input specifications and reference experimental data. The coordinated research project adopted the MHTGR-350 as the reference design using the OECD/NEA MHTGR-350 Benchmark [4] design specifications.

### 2.3.1 Summary of Prismatic HTGR Multi-physics

Section 2.3 introduced several prior studies of prismatic HTGR multi-physics. These studies highlight the importance of the proper integration of the neutronics and thermal-fluids in HTGR modeling. The neutronics and thermal-fluids physical phenomena rely heavily on each other. Hence, a coupled analysis is necessary to capture the interaction between the neutronics and the thermal-fluids. Chapter 5 discusses a coupling strategy for the neutronics and thermal-fluids phenomena in Moltres. For that exercise, Section 5.4.3 follows a simplified version of

Phase I Exercise 3 of the OECD/NEA MHTGR-350 Benchmark.

# Chapter 3

## Methodology

This chapter describes the methodology followed in the development of this thesis. This chapter comprehends the following sections: Section 3.1 describes the computational tools utilized in this work, Section 3.2 presents Moltres' mathematical basis, Section 3.3 outlines the organization of the OECD/NEA MHTGR-350 Benchmark, and Section 3.4 summarizes the characteristics of the MHTGR-350.

### 3.1 Computational tools

The following sections describe the computational tools that participated in the development of this thesis. The main computational tool was Moltres [26], described in Section 3.1.2. However, a description of Moltres is incomplete if not accompanied by an introduction to the underlying framework MOOSE [32], presented in Section 3.1.1. Additionally, Chapter 4 uses Serpent [102][103] for obtaining group constants that serve as an input to Moltres. Section 3.1.3 summarizes Serpent's most important features.

#### 3.1.1 MOOSE

MOOSE is a computational framework that supports engineering analysis applications. In a nuclear reactor, several partial differential equations describe the physical behavior. These equations are typically nonlinear, and they are often strongly coupled to each other. MOOSE targets such systems and solves them in a fully coupled manner.

MOOSE is an open-source FEM framework under a Lesser GNU Public License (LGPL). The framework itself relies on LibMesh [104], an LGPL finite element library, and PetSc, a Berkeley Software Distribution (BSD)-licensed toolkit for solving nonlinear equations [105]. MOOSE applications define weak forms of the governing equations and modularize the physics expressions into "Kernels." Kernels are C++ classes containing methods for computing the residual and Jacobian contributions of individual pieces of the governing equations. MOOSE and LibMesh translate them into residual and Jacobian functions. These functions become inputs into PetSc solution routines.

MOOSE utilizes the Jacobian-Free Newton-Krylov (JFNK) method [106] mathematical structure [32]. JFNK methods are synergistic combinations of Newton-type methods for superlinearly convergence of nonlinear equations

and Krylov subspace methods for solving the Newton correction equations. The Jacobian-vector product links the two methods. JFNK methods compute such products approximately without forming and storing the elements of the true Jacobian. The ability to perform a Newton iteration without forming the Jacobian gives JFNK methods potential for application throughout problems governed by nonlinear partial differential equations.

All the software built on the MOOSE framework shares the same Application Programming Interface (API). The applications, by default, utilize monolithic and implicit methods [26]. This feature facilitates relatively easy coupling between different phenomena and allows for great flexibility, even with a great variance in time scales [33]. Additionally, the framework and its applications use Message Passing Interface (MPI) for parallel communication and allow deployment on massively-parallel cluster-computing platforms.

### 3.1.2 Moltres

*Moltres* is a MOOSE-based application initially designed for modeling fluid-fuelled MSRs. Moltres inherits all the attributes from MOOSE as its application. Moltres is an open-source simulation tool that operates under an LGPL. It uses *git* for version control, emphasizing its openness and promoting quality through peer review. Moltres openness is an important feature and contrasts previous multi-physics applications, which operated under restrictive licenses.

Moltres solves arbitrary-group neutron diffusion, delayed neutron precursor concentration, and temperature governing equations. It can solve the equations in a fully-coupled way or solve each system independently, allowing for great flexibility and making it applicable to a wide range of nuclear engineering problems.

Moltres is the primary tool in the development of this thesis. Its role is to simulate prismatic HTGRs. Chapter 4 and 5 compare the results calculated by Moltres and other software to validate Moltres' calculation scheme. This work also intends to identify Moltres flaws in prismatic HTGR simulations and sets a basis for future work.

### 3.1.3 Serpent

The Serpent Monte Carlo code [102] [44] is a three-dimensional continuous-energy neutron transport application developed by the VTT Technical Research Centre of Finland, and it has been in public distribution since 2009. Monte Carlo neutron transport tools have several reactor physics applications related to criticality safety analyses, radiation shielding problems, detector modeling, and validation of deterministic solvers. The Monte Carlo method's main advantage is its capability to model geometry and interaction physics without significant approximations. The main disadvantage is that simulating complex systems is computing-intensive, restricting applications to some extent.

In general, Serpent serves two purposes: (1) reactor modeling and (2) group constant generation. In reactor modeling, the Monte Carlo simulation itself represents the solution to the full-scale problem. In group constant

generation, the transport simulation produces input parameters for a deterministic solver. Based on a few energy groups, deterministic solvers allow for carrying out coupled full-core analyses.

In this work, Serpent produces group constants that serve as an input for Moltres and solves for neutron fluxes in high geometric fidelity and continuous energy cross-sections. This last step provides the reference solutions for the validation of the Moltres calculation scheme. This work used Serpent 2.1.31 and the cross-section library JEFF3.1.2 for the calculations. The reason for using Serpent to generate group constants is due to its ability to run explicit simulations of randomly located TRISO particles. Applying a simple volume homogenization proves inaccurate due to the resonant scattering effect of the kernel and coated layers [65]. Although the particles' explicit modeling is time-consuming, costly, and impractical for most applications, it is necessary.

## 3.2 Mathematical basis

The last section introduced Moltres as the primary computational tool utilized in this thesis. This section presents this thesis' mathematical basis, which are the equations that describe the neutronics and thermal-fluids of prismatic HTGRs in the steady-state limit. For a more detailed explanation, refer to Section 7.2. Moltres and MOOSE heat conduction module translate these equations into kernels.

### 3.2.1 Diffusion and precursors equations

Moltres translates the multi-group diffusion equations into kernels, equations that describe the steady-state behavior of the neutron flux and calculates the multiplication factor [64]

$$\nabla \cdot D_g \nabla \phi_g - \Sigma_g^r \phi_g + \sum_{g \neq g'}^G \Sigma_{g' \rightarrow g}^s \phi_{g'} + \chi_g^t \sum_{g'=1}^G \frac{1}{k_{eff}} v \Sigma_{g'}^f \phi_{g'} = 0 \quad (3.1)$$

where

$D_g$  = group  $g$  diffusion coefficient [ $cm$ ]

$\phi_g$  = group  $g$  neutron flux [ $n \cdot cm^{-2} \cdot s^{-1}$ ]

$\Sigma_g^r$  = group  $g$  macroscopic removal cross-section [ $cm^{-1}$ ]

$\Sigma_{g' \rightarrow g}^s$  = group  $g'$  to group  $g$  macroscopic scattering cross-section [ $cm^{-1}$ ]

$\chi_t^p$  = group  $g$  total fission spectrum [-]

$G$  = number of discrete energy groups [-]

$k_{eff}$  = multiplication factor [-]

$v$  = number of neutrons produced per fission [-]

$\Sigma_g^f$  = group  $g$  macroscopic fission cross-section [ $cm^{-1}$ ].

In different sections of this thesis, Moltres imposes several boundary conditions. The vacuum boundary condition [64] states that no neutrons penetrate the boundary in the inward direction — the incoming current density is equal to zero

$$J_g^-(r_s) = \frac{1}{4}\phi_g(r_s) + \frac{D}{2}\hat{n}_s \cdot \nabla\phi_g(r_s) = 0 \quad (3.2)$$

where

$J_g^-(r)$  = incoming current density [ $n \cdot cm^{-2} \cdot s^{-1}$ ]

$r_s$  = position of the boundary [ $cm$ ]

$\hat{n}_s$  = normal direction to the boundary [-].

The reflective boundary condition states that no neutrons penetrate the boundary — the current density is equal to zero

$$J_g(r_s) = 0 \quad (3.3)$$

where

$r_s$  = position of the boundary [cm]

$J_g(r)$  = current density [ $n \cdot cm^{-2} \cdot s^{-1}$ ].

The periodic boundary condition states that the flux and current density are equal on both sides of the boundary

$$\phi_g(r_{s^-}) = \phi_g(r_{s^+}) \quad (3.4)$$

$$J_g(r_{s^-}) = J_g(r_{s^+}) \quad (3.5)$$

where

$J_g(r)$  = current density [ $n \cdot cm^{-2} \cdot s^{-1}$ ]

$r_{s^\pm}$  = left and right side of  $r_s$  boundary [cm].

### 3.2.2 Thermal-fluids

The three-dimensional steady-state heat conduction equation solves the temperature in the fuel, helium gap, moderator, coolant film, and reflector [3]

$$k_i \nabla^2 T_i + Q_i = 0 \quad (3.6)$$

where

$i = f$  (fuel),  $g$  (helium gap),  $m$  (moderator),  $cf$  (coolant film),  $r$  (reflector)

$k_i$  = material  $i$  thermal conductivity [ $W \cdot cm^{-1} \cdot K^{-1}$ ]

$T_i$  = material  $i$  temperature [ $^{\circ}C$ ]

$Q_i$  = material  $i$  volumetric heat source [ $W \cdot cm^{-3}$ ].

Equations 3.7 and 3.8 define the heat source in the stand-alone and coupled calculations, respectively

$$Q_f = Q_0 \quad (3.7)$$

$$Q_f = \sum_{g=1}^G \epsilon_g^f \Sigma_g^f \phi_g \quad (3.8)$$

$$Q_g = Q_m = Q_{cf} = Q_r = 0 \quad (3.9)$$

where

$Q_i$  = material  $i$  volumetric heat source [ $W \cdot cm^{-3}$ ]

$\epsilon_g^f$  = energy released per fission [J]

$\Sigma_g^f$  = group  $g$  macroscopic fission cross-section [ $cm^{-1}$ ]

$\phi_g$  = group  $g$  neutron flux [ $n \cdot cm^{-2} \cdot s^{-1}$ ].

The governing equation of the coolant is the one-dimensional steady-state energy conservation equation [107][89]

$$\rho_{c,i} u_i \frac{\partial}{\partial z} (c_{p,c} T_c) = q''_{conv} \quad (3.10)$$

$$q''_{conv} = h \frac{\epsilon}{A} (T_i - T_c) \quad (3.11)$$

where

$\rho_{c,i}$  = inlet coolant density [ $kg \cdot cm^{-3}$ ]

$u_i$  = inlet coolant velocity [ $cm \cdot s^{-1}$ ]

$c_{p,c}$  = coolant specific heat capacity [ $J \cdot kg^{-1} \cdot K^{-1}$ ]

$T_c$  = coolant temperature [ $^{\circ}C$ ]

$q''_{conv}$  = convective heat transfer [ $W \cdot cm^{-3}$ ]

$A$  = cross-sectional area [ $cm^2$ ]

$h$  = heat transfer coefficient [ $W \cdot cm^{-2} \cdot K^{-1}$ ]

$T_i$  = solid temperature [ $^{\circ}C$ ].

Equation 3.14 calculates the film thermal conductivity  $k_f$  [3]

$$Nu = 0.023 Re^{0.8} Pr^{0.4} \quad (3.12)$$

$$h = \frac{Nu \cdot k_c}{D_h} \quad (3.13)$$

$$k_f = h R_{cf} \ln(R_{cf}/R_c) \quad (3.14)$$

where

$Nu$  = Nusselt number [-]

$Re$  = Reynolds number [-]

$Pr$  = Prandtl number [-]

$h$  = heat transfer coefficient [ $W \cdot cm^{-2} \cdot s^{-1}$ ]

$D_h$  = hydraulic diameter [ $cm$ ]

$k_c$  = coolant thermal conductivity [ $W \cdot cm^{-1} \cdot K^{-1}$ ]

$k_{cf}$  = coolant film thermal conductivity [ $W \cdot cm^{-1} \cdot K^{-1}$ ]

$R_{cf}$  = coolant film radius [ $cm$ ]

$R_c$  = coolant channel radius [ $cm$ ].

### 3.3 OECD/NEA MHTGR-350 Benchmark

Chapters 4 and 5 conduct several exercises of the benchmark [4] using Moltres. The OECD/NEA defined such a benchmark using the MHTGR-350 reactor [18] as the reference design. The scope of the benchmark is twofold: (1) establish a well-defined problem, based on a common given data set, to compare methods and tools in core simulation and thermal fluids analysis, and (2) test the depletion capabilities of various lattice physics tools available for prismatic HTGRs. The benchmark defines several phases and exercises, summarized in Table 3.1.

### 3.4 MHTGR-350 Reactor Description

This section describes the MHTGR-350 reactor. The core consists of an array of hexagonal fuel elements in a cylindrical arrangement, pictured in Figure 3.1. Nineteen graphite replaceable reflector elements compose the

Table 3.1: Description of the OECD/NEA MHTGR-350 Benchmark phases and exercises.

Phase	Exercise	Description
I	1	Neutronics solution with fixed cross-sections
	2	Thermal fluids solution with given heat sources
	3	Coupled neutronics-thermal fluids steady state solution
II	1	Depressurized Conduction Cooldown without reactor trip
	2	Pressurized Conduction Cooldown with reactor trip
	3	Water ingress with reactor trip
	4	Power 100-80-100 load follow
III	-	Lattice Depletion Calculation

inner reflector region. A ring of identically sized graphite replaceable reflector elements surrounds the fuel elements. Then, a region of permanent reflector elements surrounds the replaceable reflectors. The reactor vessel encases all the elements. Ten layers of fuel elements stacked on top of each other compose the 66 fuel columns that integrate the active core. Figure 3.1b shows an axial view of the reactor. Table 3.2 summarizes the reactor's main characteristics.

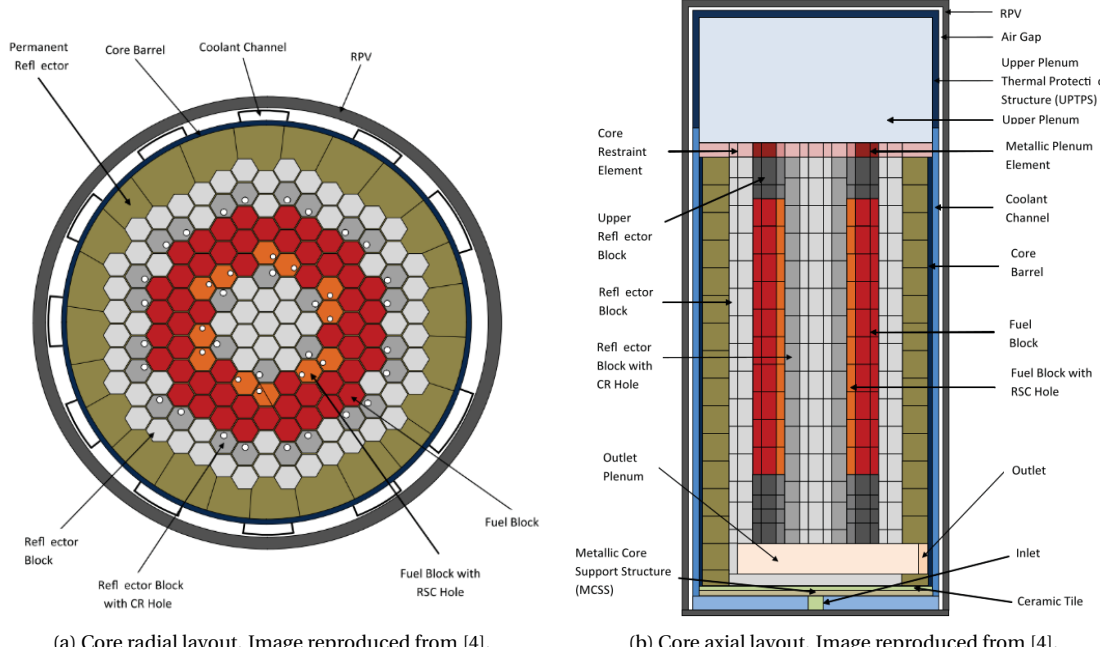


Figure 3.1: MHTGR-350 reactor layout.

The core has two types of fuel elements: a standard element and a reserve shutdown element that contains a channel for Reserve Shutdown Control, Figure 3.2. Table 3.3 specifies the details of the MHTGR-350 fuel elements. Twelve columns in the core contain Reserve Shutdown Control channels for borated graphite pellets. Hoppers

Table 3.2: MHTGR-350 Characteristics [4].

Characteristics	Value
Installed Thermal Capacity	350 MWth
Installed Electric Capacity	165 MWe
Core inlet/outlet Temperature	259/687 °C
Power Density	5.9 MW·m <sup>-3</sup>
Reactor Vessel Outside diam.	6.8 m
Reactor Vessel Height	22 m
Active core radius	2.97 m
Active core height	7.93 m
Top reflector height	1.20 m
Bottom reflector height	1.60 m
Number of fuel columns	66
Number of inner reflector columns	19
Number of outer reflector columns	78

above the core house the pellets, and if the control rods become inoperable, the pellets drop into the channels [4].

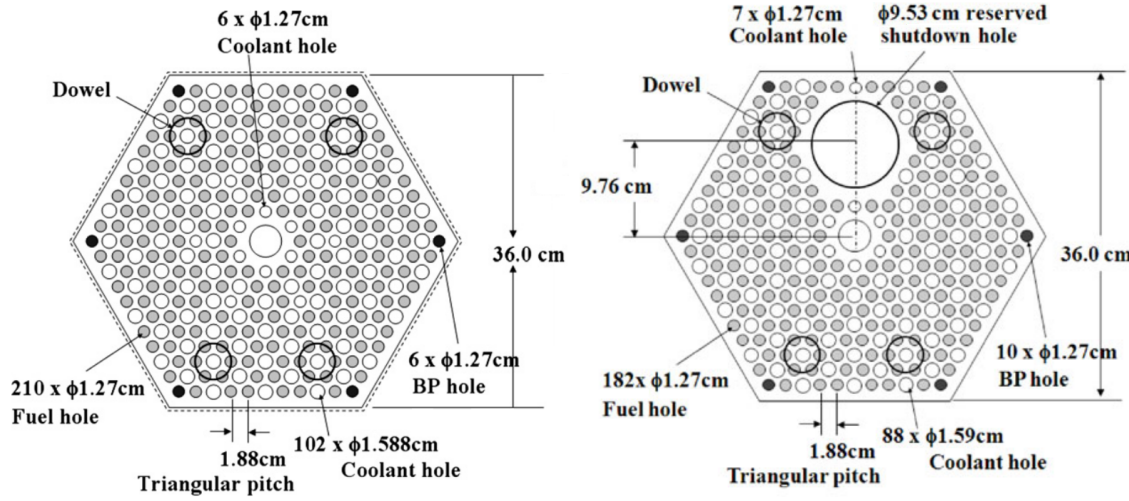


Figure 3.2: MHTGR-350 fuel assembly layout.

The fuel elements contain blind holes for fuel compacts and full-length channels for helium coolant flow. Table 3.4 specifies the details of the TRISO particle and fuel compact designs of the MHTGR-350.

A combination of lumped burnable poison and control rods manages the core reactivity. The lumped burnable poison consists of boron carbide (B<sub>4</sub>C) granules dispersed in graphite compacts. The current design uses six lumped burnable poison rods per element. Table 3.5 displays the characteristics of the lumped burnable poison compacts. The reactor has 30 control rods. Six are for reactor start-up and are in the inner reflector, while the remaining 24 are operating control rods and manage the reactivity during power operation and reactor trips.

Table 3.3: MHTGR350 fuel element characteristics [4].

Shared characteristics	Value	Units
Block pitch (flat-to-flat)	36	cm
Fuel length	79.3	cm
Fuel handling diameter	3.5	cm
Fuel handling length	26.4	cm
RSC hole diameter	9.525	cm
RSC center to assembly center	9.756	cm
Fuel/coolant pitch	1.879	cm
Fuel hole radius	0.635	cm
Compacts per fuel hole	15	-
Large coolant hole radius	0.794	cm
Small coolant hole radius	0.635	cm
Burnable posion hole radius	0.635	cm
Block graphite density	1.85	$\text{g} \cdot \text{cm}^{-3}$
<hr/>		
Standard element		
Number of large coolant holes	120	-
Number of small coolant holes	6	-
Number of fuel holes	210	-
<hr/>		
RSC element		
Number of large coolant holes	88	-
Number of small coolant holes	7	-
Number of fuel holes	186	-

Table 3.4: TRISO and fuel compact characteristics [4].

Characteristic	Value	Units
Fuel	$\text{UC}_{0.5}\text{O}_{1.5}$	-
Enrichment (average)	15.5	wt%
Packing fraction (average)	0.35	-
Kernel radius	0.02125	cm
Buffer radius	0.03125	cm
IPyC radius	0.03475	cm
SiC radius	0.03825	cm
OPyC radius	0.04225	cm
Compact radius	0.6225	cm
Compact gap radius	0.6350	cm
Compact length	4.9280	cm
Kernel density	10.50	$\text{g} \cdot \text{cm}^{-3}$
Buffer density	1.00	$\text{g} \cdot \text{cm}^{-3}$
IPyC density	1.90	$\text{g} \cdot \text{cm}^{-3}$
SiC density	3.20	$\text{g} \cdot \text{cm}^{-3}$
OPyC density	1.90	$\text{g} \cdot \text{cm}^{-3}$
Compact matrix density	1.74	$\text{g} \cdot \text{cm}^{-3}$

Table 3.5: Burnable poison compact characteristics [4].

Characteristic	Value	Units
Absorber	B <sub>4</sub> C	-
Packing fraction	0.109	-
Kernel radius	0.0100	cm
Buffer radius	0.0118	cm
PyC radius	0.0141	cm
Compact radius	0.5715	cm
Compact gap radius	0.6350	cm
Rod length	72.187	cm
Kernel density	2.47	g · cm <sup>-3</sup>
Buffer density	1.00	g · cm <sup>-3</sup>
PyC density	1.87	g · cm <sup>-3</sup>
Compact matrix density	0.94	g · cm <sup>-3</sup>

## 3.5 Organization of the Simulations

This thesis separates the description of Moltres simulations into Chapters 4 and 5. Chapter 4 focuses on stand-alone neutronics simulations in which Moltres solves equations 3.1 and 3.8 to calculate the multiplication factor, the neutron flux, and the radial power distribution. Chapter 4 discusses two main validation exercises. The first exercise compares a Serpent and Moltres model  of the MHTGR-350. Serpent obtains the multiplication factor, the neutron flux in arbitrary locations of the reactor, and the radial power distribution in the reactor core. Serpent also generates the group constants of the MHTGR-350 that serve as an input for Moltres simulations. The second exercise follows Phase I Exercise 1 of the OECD/NEA MHTGR-350 Benchmark using Moltres. The benchmark exercise specifies the group constants that Moltres uses in the simulations.

Chapter 5 focuses on stand-alone thermal-fluids and coupled neutronics/thermal-fluid simulations. Chapter 5 discusses several exercises to validate the thermal-fluids model, in which Moltres solves equations 3.6-3.14 to calculate the solid and coolant temperatures. The first validation exercises study the accuracy of the thermal-fluids model in several configurations, including an equivalent cylindrical model of a unit cell, a three-dimensional unit cell, and a three-dimensional fuel column. The next exercise follows Phase I Exercise 2 of the OECD/NEA MHTGR-350 Benchmark using Moltres. Chapter 5 also describes a coupling exercise that follows Phase I Exercise 3 of the OECD/NEA MHTGR-350 Benchmark using Moltres.

# Chapter 4

## Neutronics

This chapter presents several studies that use Moltres as a stand-alone neutronics solver. The objective of the chapter is to validate Moltres' calculation scheme by comparing Moltres results to Serpent and the OFCD/NEA MHTGR-350 Benchmark. This chapter comprehends the following sections: Section 4.1 describes some preliminary studies that help set up Serpent and Moltres simulations, Section 4.2 presents several studies comparing Moltres and Serpent results, Section 4.3 discusses Moltres results of Phase I Exercise 1 of the benchmark, and Section 4.4 concludes the chapter with a summary of the chapter and its key points.

### 4.1 Preliminary studies

This section's purpose is to find the right set up of Serpent and Moltres input files. Section 4.1.1 focuses on the definition of the materials in Serpent input file for obtaining the group constants for Moltres. Section 4.1.2 analyzes different ways to set up Moltres input files.

#### 4.1.1 Homogeneous vs. heterogeneous isotope distribution

This section determines the proper way to treat the fuel compact heterogeneities in Serpent. This study modeled in Serpent two different material distributions in a fuel compact: a homogeneous distribution of the isotopes and a heterogeneous distribution that explicitly modeled the TRISO particles. The study used a hexagonal unit cell model that included the fuel compact, a helium gap, and the surrounding graphite, exhibited in Figure 4.1. Table 3.4 specifies the model input parameters. The material temperature was 1200K, a case that represents the Hot Full Power (HFP) core state. The Serpent simulations included  $5 \times 10^4$  neutrons per cycle, 500 active cycles, and 50 inactive cycles for the calculations. The homogeneous distribution simulation took 1.73 minutes and the heterogeneous distribution simulation 2.21 minutes using 256 cores — the heterogeneous calculation took 28% longer.

The multiplication factor ( $k_{eff}$ ) was  $1.17527 \pm 0.00021$  for the homogeneous distribution and  $1.25107 \pm 0.00020$  for the heterogeneous distribution. Serpent generated the group constants using the three energy group structure

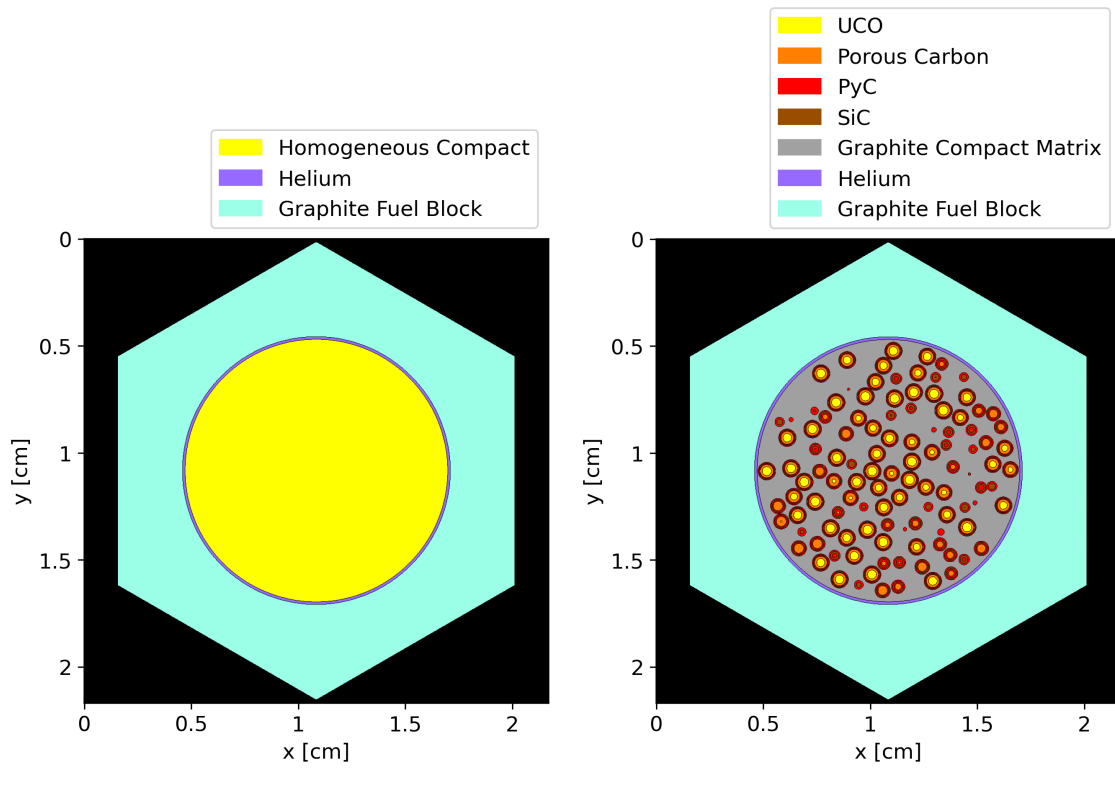


Figure 4.1: Comparison of different Serpent models of the fuel compact.

[0, 2.38eV, 111keV, 20MeV]. Using the heterogeneous distribution as the reference, a Python script calculated the group constants' relative error. The evaluated parameters were  $D_g$ ,  $\Sigma_g^r$ ,  $v\Sigma_g^f$  and  $\chi_g^t$  (see Equation 3.1). Figure 4.2 displays the relative errors for  $\Sigma_g^r$  and  $v\Sigma_g^f$ , which were the group constants that changed the most. The figure does not include  $D_g$  and  $\chi_g^t$  because their relative errors were less than 1%. The relative errors of  $\Sigma_g^r$  and  $v\Sigma_g^f$  were less than 6%.

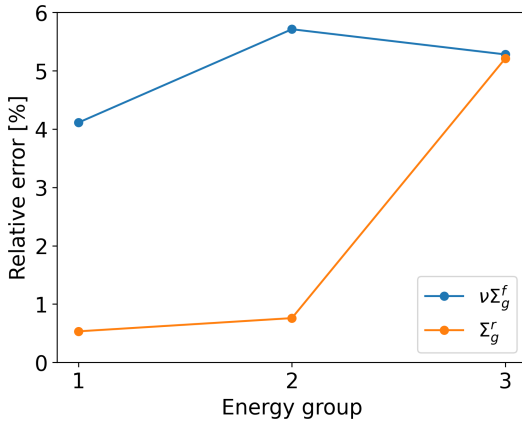


Figure 4.2: Relative error of the group constants generated with a homogeneous isotope distribution vs. explicit TRISO modeling.

The results show that the homogenization of the fuel compact isotopes decreases the multiplication factor considerably. The impact on the group constants does not seem to be substantial; however, the multiplication factor's considerable difference suggests that the combined effect of the small variations in the group constants is significant. Based on these results, Serpent models the TRISO particles explicitly for generating the group constants in the following sections.

#### 4.1.2 Problem set-up

Diffusion calculations necessitate a spatial homogenization of the group constants. Depending on the desired level of detail, the type of homogenization could vary. For example, in PWR core calculations, the homogenization in space could be per assembly or pin-by-pin [108]. In a per-assembly homogenization, the diffusion solver represents the assembly as a single material neutronically (we will refer to diffusion calculations using this type as homogeneous calculations). A pin-by-pin homogenization treats the pin or assembly heterogeneities, yielding a more detailed neutronic representation of the fuel assembly (we will refer to diffusion calculations of this type as heterogeneous calculations).

Previous work [26][109] used Moltres for simulating MSRs, which allow for heterogeneous calculations. In those calculations, the authors defined two materials in Moltres input files: the moderator and the fuel. For such a

configuration, a moderator mesh node holds the neutronics and temperature information only of the moderator.

The same is true for the fuel.

Keeping in mind Moltres proven capabilities, this work aimed for a heterogeneous calculation of a prismatic HTGR. For this study, Serpent modeled a fuel column of the MHTGR-350 and generated the group constants. Figure 4.3 displays the Serpent model geometry. Serpent generated the group constants for three materials: moderator, coolant, and fuel compact. The Serpent simulations included  $5 \times 10^5$  neutrons per cycle, 400 active cycles, and 100 inactive cycles for the calculations. Taking advantage of the problem's symmetry, Moltres modeled only  $1/12^{th}$  of the fuel column, shown in Figure 4.3. I made the geometry and mesh using Gmsh [110]. The diffusion calculation had  $1.84 \times 10^5$  degrees of freedom (DoFs) per energy-group.

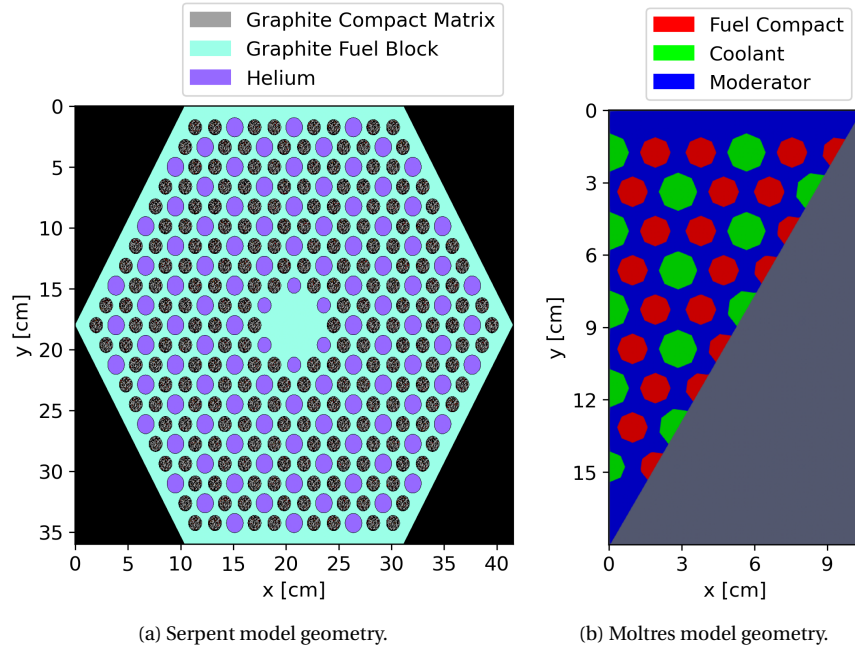


Figure 4.3: Fuel column of the MHTGR-350.  $xy$ -plane in the active core region.

Moltres simulation **obeyed** the eigenvalue convergence tolerance of  $1 \times 10^{-8}$ , defined by equation 4.1

$$\frac{k^{(n)} - k^{(n-1)}}{k^{(n)}} < \varepsilon \quad (4.1)$$

where

$k^{(n)}$  = eigenvalue at iteration  $n$  [-]

$\varepsilon$  = convergence tolerance [-].

The calculation used two energy groups with the structure [0, 0.625eV, 20MeV]. The eigenvalue calculation did not converge. Although several factors could contribute to this behavior, I focused on the validity of the diffusion calculations in this system.

In diffusion theory, the current density  $J$  is proportional to the gradient of the flux [102]

$$J = -D \nabla \phi \quad (4.2)$$

where

$J$  = current density [ $n \cdot cm^{-2} \cdot s^{-1}$ ]

$D$  = diffusion coefficient [ $cm$ ]

$\phi$  = neutron flux [ $n \cdot cm^{-2} \cdot s^{-1}$ ].

This approximation relies on the following assumptions:

- the angular flux does not depend strongly on the angular variables,
- the fission source is isotropic,
- the time derivative of the current density is small compared to the mean collision time,
- and the anisotropic energy-transfer due to scattering is negligible in group-to-group scattering.

More detailed studies of the transport equation indicate that the following cases violate the assumption of a weak angular dependence [64]:

- regions near vacuum boundaries and low-density material regions,
- regions near strongly absorbing media,
- and regions near localized sources.

The diffusion theory applies best to geometries consisting of large homogeneous regions where the flux gradient is small, which is the case for material regions whose geometrical scales are considerably larger than the neutron

mean free path. For this reason, Table 4.1 compares the neutron mean free path in the different fuel assembly materials. The mean free path in the fuel compact and the moderator are in the order of the centimeters, while in the coolant, the mean free path is comparable to the fuel column dimensions. These results suggest that a heterogeneous diffusion calculation of the prismatic fuel column challenges some of the diffusion theory assumptions.

Table 4.1: Neutron mean free path in different materials. Values expressed in [cm].

	Fuel compact	Moderator	Coolant	Homogeneous fuel
Fast	2.71	2.70	1137.31	3.37
Thermal	2.22	2.36	1945.49	2.89



Next, I conducted a feasibility study for the homogeneous calculation of the fuel assembly in Moltres. Serpent calculated the fuel assembly's homogeneous group constants by homogenizing the fuel, coolant, and moderator. This material's mean free path is in the order of the centimeters, shown in Table 4.1. Next, Moltres simulation used the homogeneous group constants to carry out an eigenvalue calculation. Comparing Moltres results with Serpent results, Serpent's  $k_{eff}$  was  $1.41942 \pm 0.00007$  while Moltres' was 1.40788. Equation 4.3 calculates the reactivity difference ( $\Delta\rho$ ) between the eigenvalues calculated by Serpent and Moltres

$$\Delta\rho = |\rho_1 - \rho_2| = \left| \frac{k_1 - 1}{k_1} - \frac{k_2 - 1}{k_2} \right| = \left| \frac{k_1 - k_2}{k_1 k_2} \right| \quad (4.3)$$

where

$k_1$  = Serpent-derived eigenvalue[–]

$k_2$  = Moltres-derived eigenvalue[–].

The eigenvalue calculated by Moltres is 577 pcm smaller than the calculated by Serpent. Additionally, Figure 4.4 displays the axial flux in the fuel column obtained with Serpent and Moltres. Note that Serpent's flux is the average value of the flux in each bin of the detector, while Moltres flux is the point-wise flux over the  $z$ -axis

$$\phi_s(z) = \frac{\int_{\Delta V} \phi(x, y, z) dV}{\Delta V} \quad (4.4)$$

$$\phi_m(z) = \phi(x, y, z) \quad (4.5)$$

where

$$\phi_s(z) = \text{Serpent axial flux } [n \cdot cm^{-2} \cdot s^{-1}]$$

$$\Delta V = \text{volume of the detector bins } [cm^3]$$

$$\phi_m(z) = \text{Moltres axial flux } [n \cdot cm^{-2} \cdot s^{-1}].$$

The fluxes are similar in shape and magnitude. I emphasize that this was a feasibility study and the analysis remains qualitative. The following sections present a more in-depth analysis of more detailed results. Based on these results and discussion, the following sections study homogeneous calculations using Moltres.

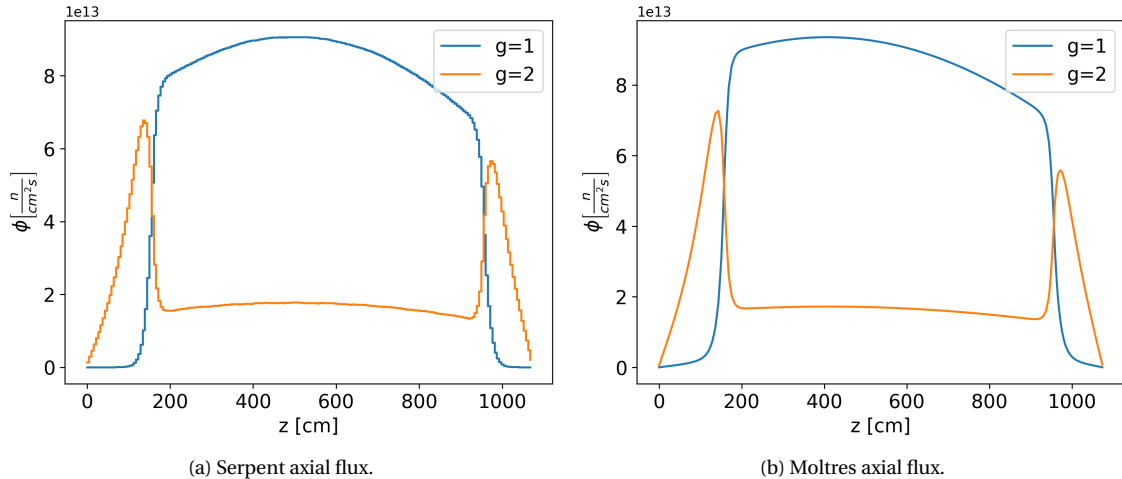


Figure 4.4: Two energy group axial flux in the fuel column calculated with Serpent and Moltres.

## 4.2 Serpent-Moltres comparison

In this section, Serpent modeled a fuel column and the full-core of the MHTGR-350. Serpent obtained the homogenized group constants that served as input to Moltres. The following sections compare Moltres and Serpent results as a validation exercise.

### 4.2.1 Fuel column

This section investigates the effects of the energy group structure on the diffusion simulations. A first analysis varied the number of energy groups, while a second analysis varied the energy group structures with a constant number of energy groups. The analyses focused on a fuel column of the MHTGR-350, shown in Figure 4.3. To reduce the

computational expense. Tables 3.3 and 3.4 specify the model input parameters.

The first step in the calculation obtained the group constants using Serpent. Serpent model did not consider the fuel handling holes or the bottom and top reflectors' coolant channels for simplicity. HTGRs use burnable poisons to reduce the power peaking factors in various active core regions. Some reactors have burnable poisons in the rings closer to the reflectors and no burnable poisons in the middle rings. This characteristic motivated the analysis of two cases: one fuel column that does not have burnable poisons and one that does. The burnable poisons' locations are the six corners of the fuel assembly, shown in Figure 3.2. The material temperatures were 600 and 1200K, cases that represent the Cold Zero Power (CZP) and the HFP core states. The Serpent simulations included  $4 \times 10^5$  neutrons/cycle, 360 active cycles, and 40 inactive cycles for the calculations.

Taking advantage of the problem's symmetry, Moltres modeled a  $1/12^{th}$ -section of the homogenized fuel column. I chose the geometry and mesh, which had  $3.71 \times 10^4$  elements and  $2.29 \times 10^4$  nodes, using Gmsh. The diffusion calculations had  $2.29 \times 10^4$  DoFs per energy-group. The Moltres simulations obeyed an eigenvalue and a flux convergence tolerance of  $1 \times 10^{-8}$ . Moltres calculations used the different energy group structures listed in Table 4.2.

Table 4.2: Energy group structure [101].

Upper boundary [eV]	Group structure												
	26	21	18	15a	15b	15c	15d	15e	12	9	6	3	
$1.49 \times 10^7$	1	1	1	1	1	1	1	1	1	1	1	1	1
$7.41 \times 10^6$	2												
$3.68 \times 10^6$	3	2	2	2	2	2	2	2					
$6.72 \times 10^5$	4												
$1.11 \times 10^5$	5	3	3	3	3	3	3	3	3	3	2	2	2
$1.93 \times 10^4$	6	4	4	4	4						4		
$3.35 \times 10^3$	7												
$1.58 \times 10^3$	8	5	5				4						
$7.48 \times 10^2$	9	6	6	5	5			4	4	5	3		
$2.75 \times 10^2$	10	7	7	6	6	5				6	4		
$1.30 \times 10^2$	11	8	8	7	7		5	5	7	5	3		
$6.14 \times 10^1$	12	9			8	6							
$2.90 \times 10^1$	13	10	9	8	9		6	6					
$1.37 \times 10^1$	14	11	10	9						8	6		
8.32	15	12	11	10	10	7	7	7	7	9			
5.04	16												
2.38	17	13	12	11	11	8	8	8	10	7	4	3	
1.29	18	14											
$6.50 \times 10^{-1}$	19	15	13	12	12	9	9	9	11	8	5		
$3.50 \times 10^{-1}$	20	16				10	10						
$2.00 \times 10^{-1}$	21	17	14	13	13	11	11	10					
$1.20 \times 10^{-1}$	22							11					
$8.00 \times 10^{-2}$	23	18	15	14	14	12	12	12					
$5.00 \times 10^{-2}$	24	19	16			13	13	13					
$2.00 \times 10^{-2}$	25	20	17	15	15	14	14	14	12	9	6		
$1.00 \times 10^{-2}$	26	21	18			15	15	15					

Summarizing, the analyses included four operational cases:

- Operational case 1: fuel column with no burnable poisons at 600K.
- Operational case 2: fuel column with no burnable poisons at 1200K.
- Operational case 3: fuel column with burnable poisons at 600K.
- Operational case 4: fuel column with burnable poisons at 1200K.

To compare the results from Serpent and Moltres, we review the three-group axial fluxes found by each of them.

Moltres ran the calculations for 26 energy groups and a Python script collapsed the results into three energy groups to facilitate the results' visualization. Figures 4.5 to 4.8 display the axial flux from the Serpent and the Moltres simulations for all cases. The figures also display the difference between Serpent and Moltres results, where  $\phi_S$  and  $\phi_M$  correspond to the Serpent-derived flux and the Moltres-derived flux. The analysis uses the absolute difference instead of the relative difference because the large errors in the reflector hinder the visualization of the errors in the active core.

For all the operational cases, the fluxes from Serpent and Moltres are close in shape and magnitude. For operational case 1, the largest error is  $1.54 \times 10^{12}$ , located at the interface between the bottom reflector and the homogeneous fuel. For the operational case 2, 3, and 4, the largest error is  $3.81 \times 10^{12}$ ,  $8.49 \times 10^{12}$ , and  $1.52 \times 10^{13}$ , respectively. The largest error for cases 2, 3, and 4 occurs in the bottom reflector close to the homogeneous fuel interface. In all the operational cases, the largest errors occur for the thermal flux. This behavior is expected, as the diffusion theory assumptions are weaker at interfaces between different materials.

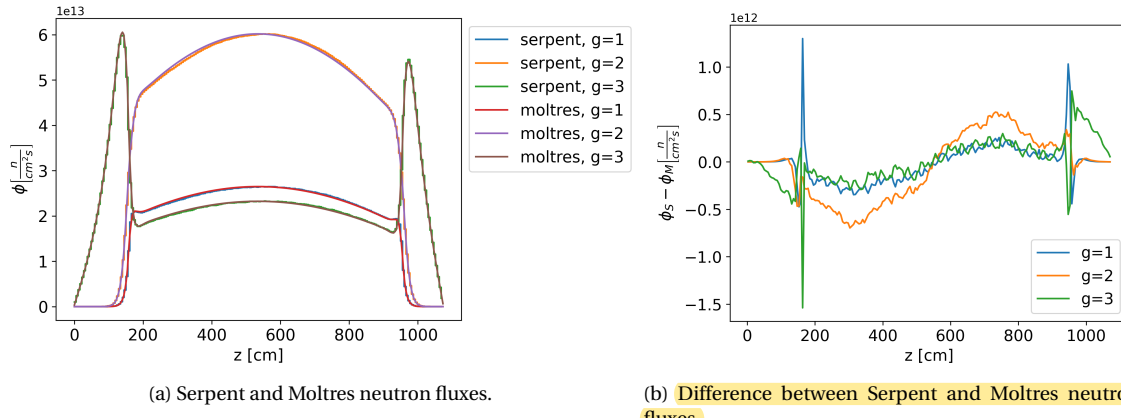


Figure 4.5: Operational case 1: fuel column with no burnable poisons at 600K. Comparison of Serpent and Moltres-derived 3-group axial neutron fluxes.

Table 4.3 exhibits the eigenvalues calculated by Serpent and  $\Delta\rho$ , calculated with equation 4.3, for the different energy group structures. The eigenvalues in Moltres differ slightly from the eigenvalues in Serpent, and overall, the

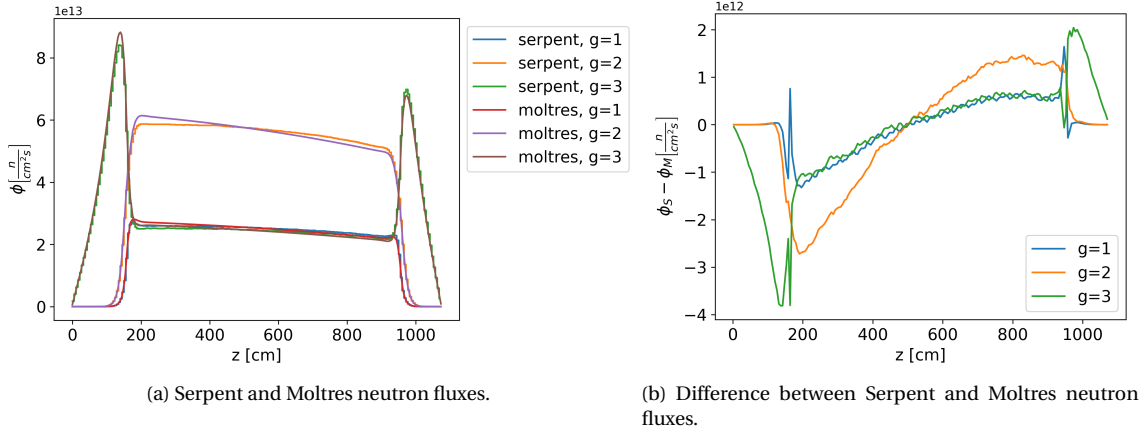


Figure 4.6: Operational case 2: fuel column with no burnable poisons at 1200K. Comparison of Serpent and Moltres-derived 3-group axial neutron fluxes.

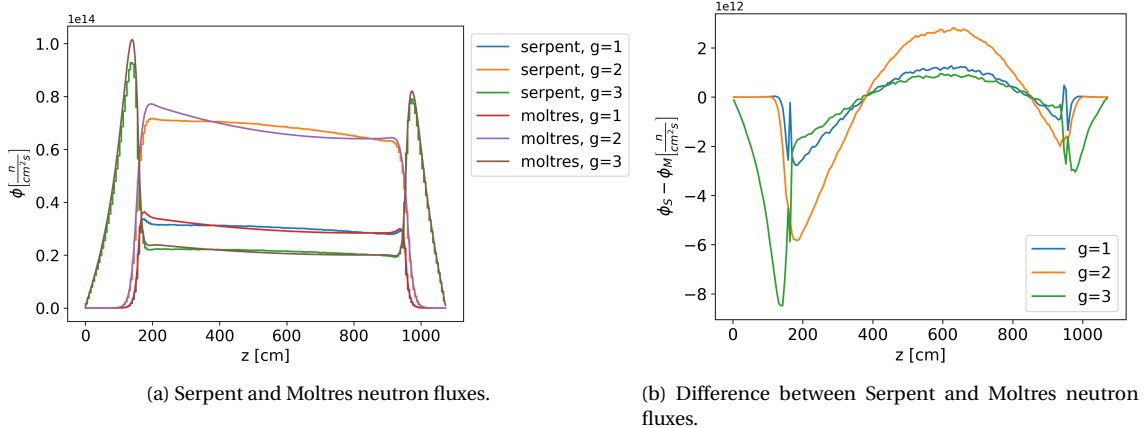


Figure 4.7: Operational case 3: fuel column with burnable poisons at 600K. Comparison of Serpent and Moltres-derived 3-group axial neutron fluxes.

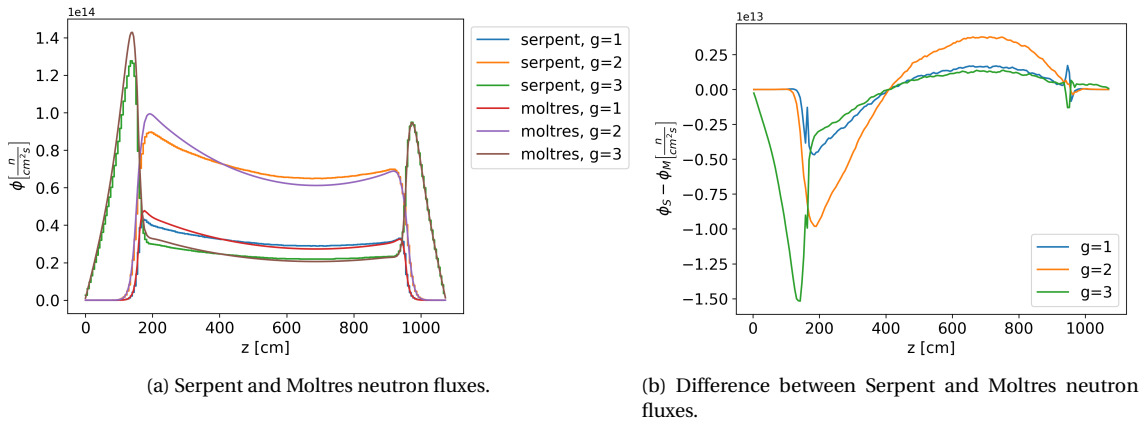


Figure 4.8: Operational case 4: fuel column with burnable poisons at 1200K. Comparison of Serpent and Moltres-derived 3-group axial neutron fluxes.

reactivity difference is less than 50 pcm. The number of energy groups does not affect the accuracy of the eigenvalue calculations in Moltres.

Table 4.3: Eigenvalues calculated by Serpent and reactivity difference between eigenvalues calculated by Moltres and Serpent, see equation 4.3, for the different energy group structures. 

Operational case	Serpent eigenvalues	$\Delta\rho$ [pcm]/Energy groups							
		3	6	9	12	15	18	21	26
1	$1.43800 \pm 0.00008$	10	7	6	6	5	6	6	12
2	$1.37771 \pm 0.00008$	23	15	4	3	2	2	1	11
3	$1.12861 \pm 0.00009$	44	21	24	25	25	24	19	9
4	$1.06554 \pm 0.00010$	36	40	29	32	44	43	25	25

The last analysis is for the Moltres axial flux. Considering the 26 group structure as the reference value, equation 4.6 obtained the  $L_2$ -norm of the active core's axial flux relative difference

$$\Delta_{L_2} = \left\| \frac{\phi_G(z) - \phi_{ref}(z)}{\phi_{ref}(z)} \right\| \quad \wedge \quad z \in L_a \quad (4.6)$$

where

$\Delta_{L_2}$  =  $L_2$ -norm relative difference [-]

$\phi_G(z)$  = G-energy groups axial flux [ $n \cdot cm^{-2} \cdot s^{-1}$ ]

$\phi_{ref}(z)$  = reference axial flux [ $n \cdot cm^{-2} \cdot s^{-1}$ ]

$L_a$  = active core length [cm].

Figures 4.9 and 4.10 show  $\Delta_{L_2}$  for the various energy group structures. Overall, the relative error decreases with an increase in the number of energy groups. Nonetheless, this is not always the case. For example, in Figure 4.9b, the thermal flux agreement improves from 12 to 15-energy groups, but the fast flux agreement worsens. Additionally, the relative error of the cases with no burnable poisons is smaller than the relative error of the cases with burnable poison. The treatment of the burnable poisons challenges the accuracy of the homogenized simulations in Moltres. Three, six, and nine energy-groups yield more than 50% error when treating the burnable poison, Figure 4.10.

The analysis also included the computational time and the peak memory usage during the simulations, as shown in Figure 4.11. All the simulations used 128 cores. This section presents only the cases at 600K because the impact of the temperature change was not significant. The computational requirements rise with an increase in the number of energy groups. As the geometry uses a constant number of elements, the number of DoFs per energy-group remains constant for all the simulations. Figure 4.11 also shows that the overall time of the cases with

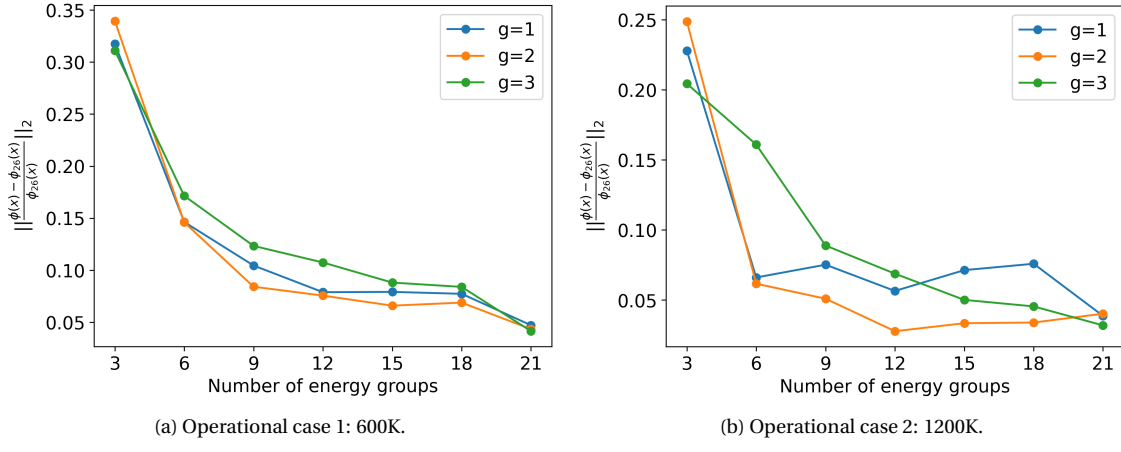


Figure 4.9: L<sub>2</sub>-norm relative error for different number of energy group structures for the operational cases with no burnable poisons.

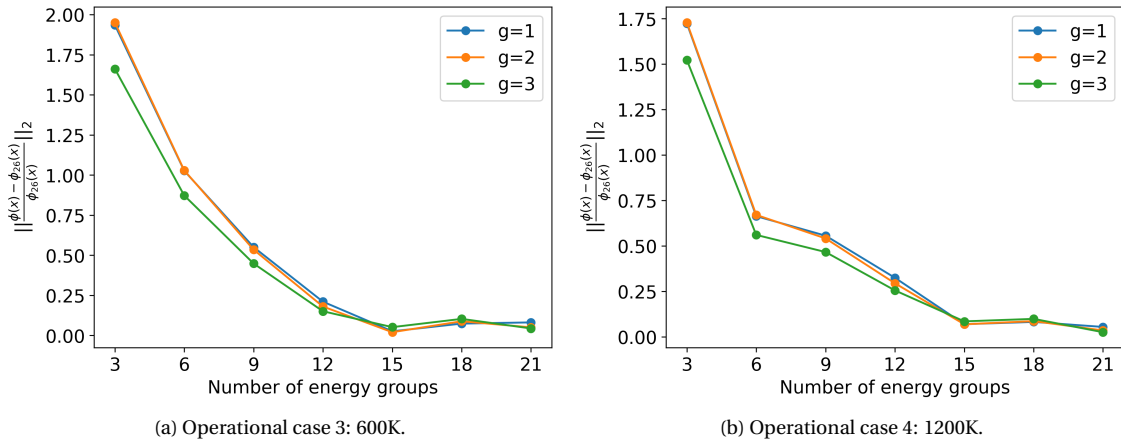


Figure 4.10: LBP case. L<sub>2</sub>-norm relative error for different number of energy group structures for the operational cases with burnable poisons.

burnable poison is higher than the cases without them.

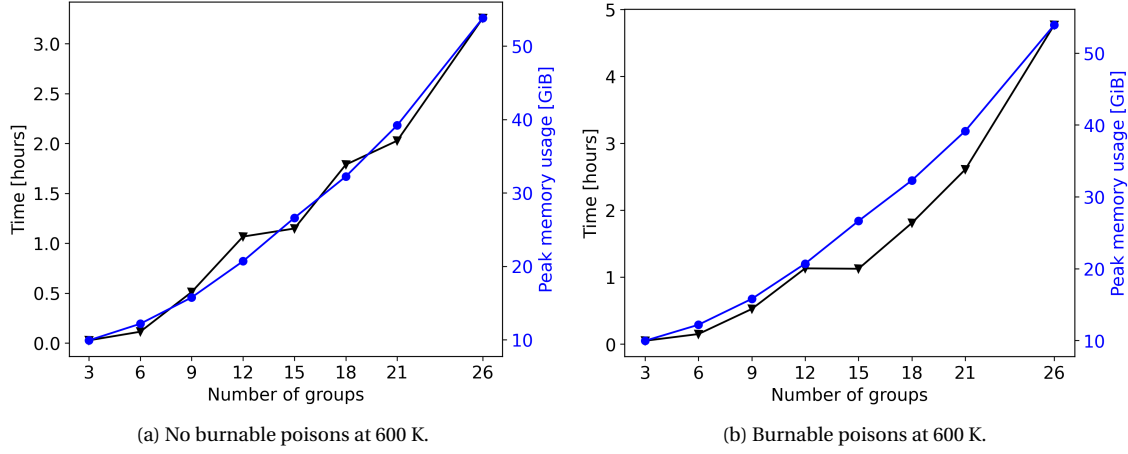


Figure 4.11: Computational time and memory requirements for different number of energy group structures.

The last study analyzed the impact of the energy group structure on the flux accuracy for a constant number of energy groups. I chose 15 energy groups, as it yields a good overall accuracy and a practical computational expense. Table 4.2 defines various energy group structures. Table 4.4 exhibits  $L_2$ -norm of the relative error for the various energy group structures. Some energy group structures yield better results for some cases while giving worse results for others. For example, the 15d structure gives better results at 600K with burnable poisons than without them. To choose the best performing structure, equation 4.7 calculated a weighted average for the different groups

$$W_{ave} = w_{th}\Delta_{th} + w_{epi}\Delta_{epi} + w_f\Delta_f \quad (4.7)$$

where

$W_{ave}$  = weighted average [-]

$w_{th}$  = thermal flux weight [-]

$w_{epi}$  = epithermal flux weight [-]

$w_f$  = fast flux weight [-]

$\Delta_{th}$  =  $L_2$ -norm relative difference of the thermal flux [-]

$\Delta_{epi}$  =  $L_2$ -norm relative difference of the epithermal flux [-]

$\Delta_f$  =  $L_2$ -norm relative difference of the fast flux [-].



I arbitrarily chose the weights to be 0.5, 0.3, and 0.2 for the thermal, epithermal, and fast fluxes. For this averaging scheme, the energy group structure 15d is the best one.

Table 4.4: Axial flux relative difference  $L_2$ -norm for various energy group structures. Values expressed in [%].

Burnable poisons	Temperature [K]	Flux	15a	15b	15c	15d	15e
No	600	Fast	7.9	8.0	8.2	8.1	9.1
		Epithermal	6.6	6.5	8.6	8.2	9.2
		Thermal	8.8	8.5	10.6	10.7	12.9
	1200	Fast	7.1	7.7	5.7	5.1	4.5
		Epithermal	3.3	3.9	6.2	5.1	3.4
		Thermal	5.0	4.7	8.5	8.2	8.4
Yes	600	Fast	24.0	24.8	2.6	2.3	3.7
		Epithermal	21.0	21.7	2.0	1.6	2.7
		Thermal	18.1	18.8	5.2	5.5	5.7
	1200	Fast	36.2	37.3	6.9	6.6	25.9
		Epithermal	33.2	34.2	6.9	6.5	25.1
		Thermal	29.6	30.6	8.5	8.3	20.3
Weighted average			17.3	17.8	6.3	6.0	10.8

## 4.2.2 Full-core

This section compares the results from Serpent and Moltres simulations of a full-core model. Figure 4.12 displays a  $xy$ -plane of the model, which includes the bottom and top reflectors. Due to symmetry, Moltres' model included only a  $1/6^{th}$  of the reactor. The first step in the calculation obtained the group constants using Serpent. Tables 3.2, 3.3, and 3.4 specify the model input parameters. For simplicity, the model considered only standard fuel assemblies for all the fuel columns. The model considered a fresh core, and it did not include the fuel handling holes nor the bottom and top reflector coolant channels. Based on the previous section analyses, this analysis uses the energy group structure 15d from Table 4.2. The material temperatures were 600K and 1200K, cases that represent the CZP and the HFP core states. The Serpent simulations included  $8 \times 10^5$  neutrons per cycle, 500 active cycles, and 100 inactive cycles for the calculations.

Moltres model mesh had  $3.0 \times 10^5$  elements and  $1.60 \times 10^5$  nodes. The diffusion calculations had  $1.60 \times 10^5$  DoFs per energy-group and a total of  $2.4 \times 10^6$  DoFs. The Moltres simulations obeyed an eigenvalue and flux convergence tolerance of  $1 \times 10^{-8}$ .

This study compares the  $k_{eff}$ , the power distribution, and the flux shape and magnitude in different zones of the reactor calculated by Serpent and Moltres. Table 4.5 exhibits the  $k_{eff}$  calculated by Serpent and Moltres. The differences between the eigenvalues calculated by Moltres and Serpent are smaller than 300 pcm.

Figures 4.13 and 4.14 show Serpent and Moltres radial power distributions. Figures 4.13b and 4.14b display the difference between Serpent and Moltres radial power distributions. The largest difference is in the inner ring, and it

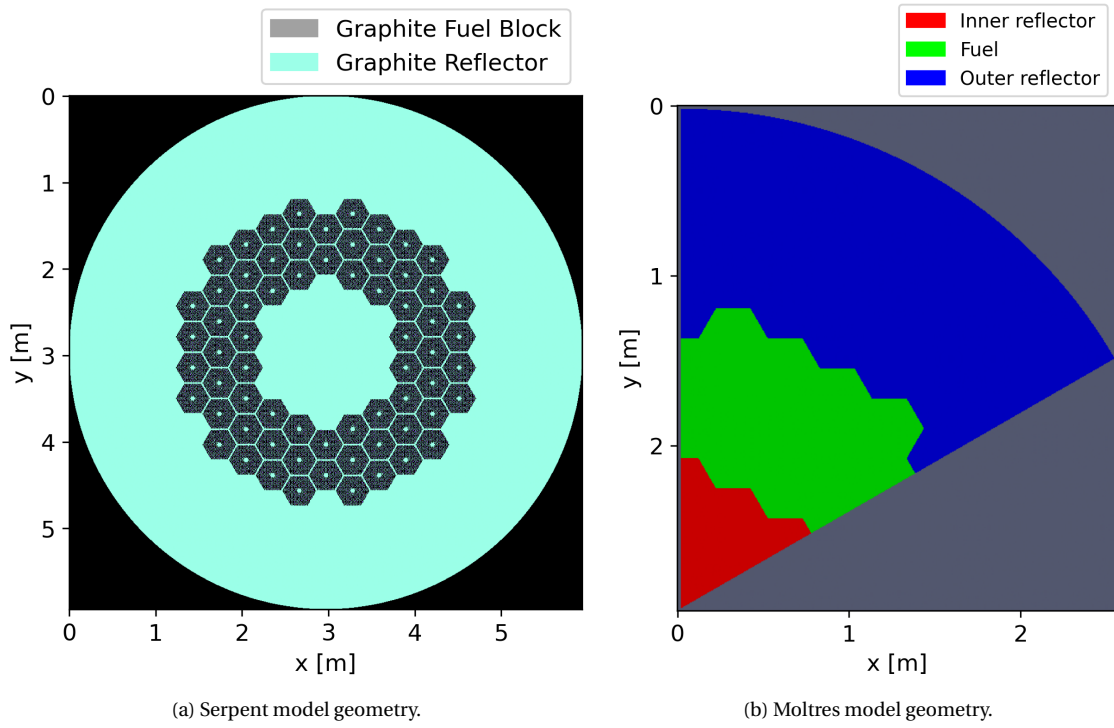
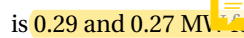


Figure 4.12: MHTGR-350 full-core model layout.

Table 4.5: Comparison between Serpent and Moltres-derived eigenvalues.

Temperature [K]	Serpent	Moltres	$\Delta\rho$ [pcm]
600	$1.10869 \pm 0.00006$	1.11150	228
1200	$1.06138 \pm 0.00006$	1.06468	292



is 0.29 and 0.27  $\text{MV}^{-1}$  at 600K and 1200K, respectively. The negative values in the figures indicate that Moltres' power density is larger than Serpent's in the inner and outer rings, whereas it is lower in the middle ring.

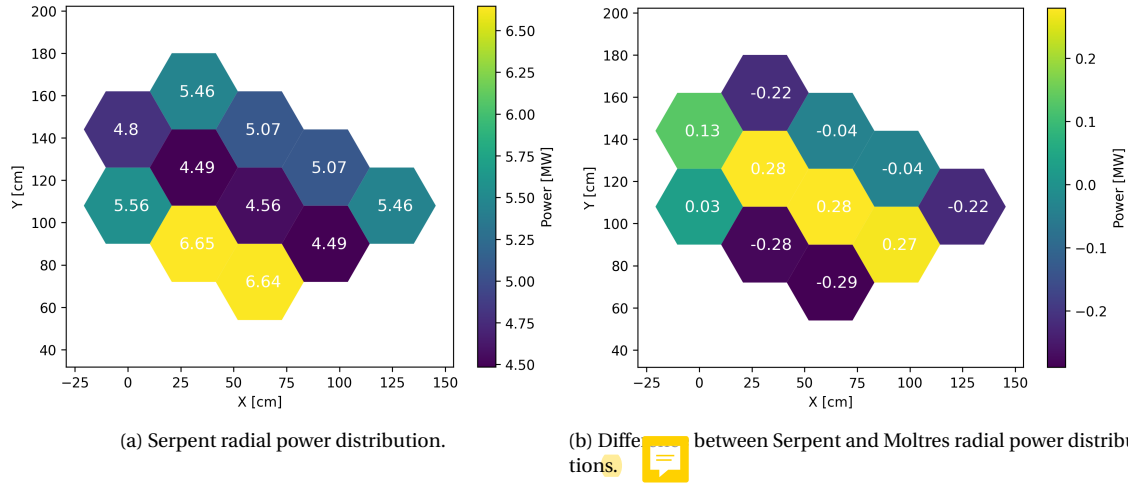


Figure 4.13: Comparison of the MHTGR-350 radial power distribution at 600 K calculated by Serpent and Moltres.

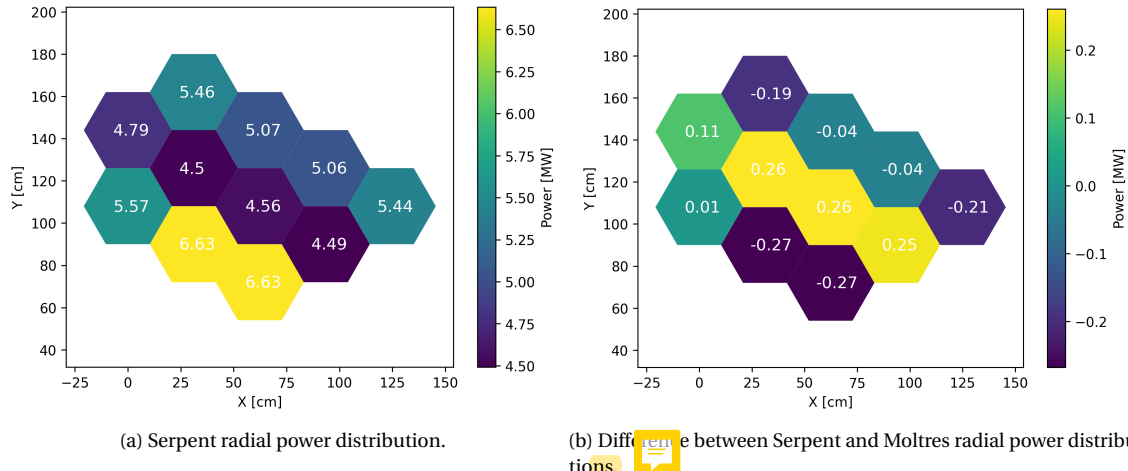
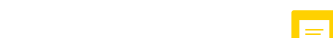


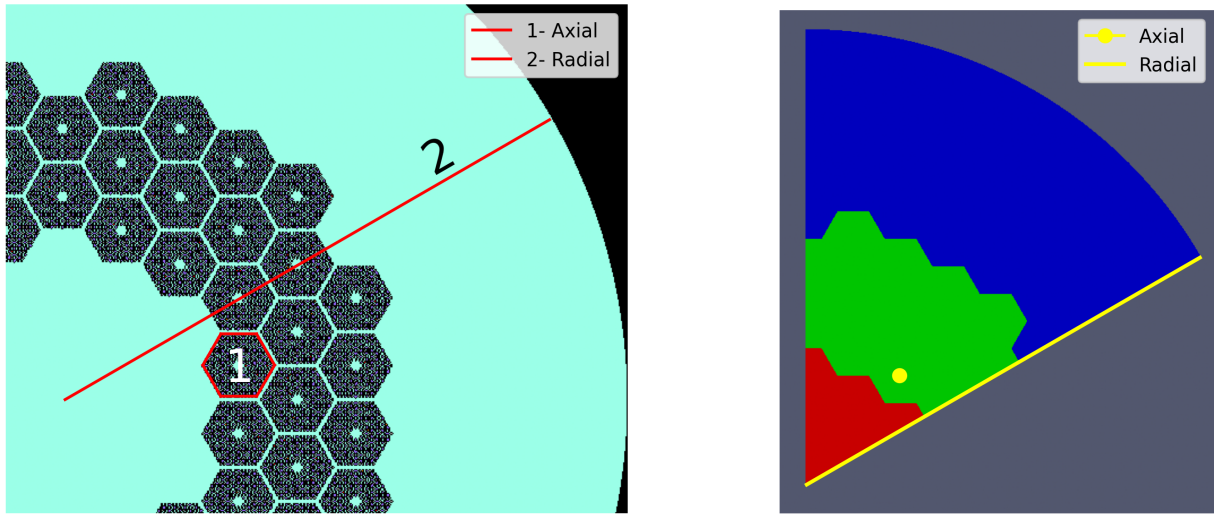
Figure 4.14: Comparison of the MHTGR-350 radial power distribution at 1200 K calculated by Serpent and Moltres.



The simulations recorded the neutron flux in axial and radial flux detectors in arbitrary regions of the reactor, shown in Figure 4.15. Serpent simulation's axial detector has the volume of a fuel column, while the radial detector has a  $2^\circ$ -opening and a fuel assembly height. Both the Serpent and Moltres radial detector's axial location was the middle of the active core's height.



The following analysis compares the flux calculated by Serpent and Moltres. Section 4.2.1 analysis was able to study the difference between Serpent and Moltres' results because the fuel column problem uses reflective boundary conditions, making the radial profile relatively flat. Given a flat radial profile, Moltres axial flux is independent of



(a) Flux detectors in Serpent model. 1- Axial detector has the volume of a fuel column. 2- Radial detector has a  $2^\circ$ -opening and a fuel assembly height.

(b) Flux detectors in Moltres model. Axial detector computes the flux over the line 'Axial'. Radial detector computes the flux over the line 'Radial'.

Figure 4.15: Axial view of the flux detector locations.

the location of the detector. In the full core problem, the radial profile is far from being flat, making Moltres axial flux sensitive to the detector's location. For this reason, the fluxes comparison remains qualitative.

Moltres simulations used 15 energy groups, and a Python script collapsed the results into three groups to facilitate the results' visualization. Figure 4.16 show the axial and radial fluxes at 600K. The fast and epithermal fluxes in Moltres results are larger than Serpent's, while the axial thermal flux is smaller. Serpent's radial flux present some 'noise.' A higher number of generations per cycle in Serpent simulations or using a detector with a larger volume would eliminate this. Additionally, the radial flux in Serpent reveals the location of the burnable poisons in the fuel assemblies. This diffusion simulation fails to capture such localized effects as the group constants are homogeneous in the fuel assembly. The fast radial flux in Moltres results is larger than Serpent's, while the radial epithermal and thermal fluxes have almost the same magnitudes. Figure 4.17 display the fluxes at 1200K, which differ from the 600K case. Still, the 1200K case exhibits the same behavior for both axial and radial fluxes. Overall, Moltres and Serpent fluxes are comparable in magnitude and shape.

### 4.3 OECD/NEA MHTGR-350 Benchmark: Phase I Exercise 1

This section discusses Phase I Exercise 1 of the OECD/NEA MHTGR-350 Benchmark conducted with Moltres and compares the results with those already published [98]. The benchmark specifies the group constants required to conduct the exercise, ensuring a common dataset among various benchmark participants and allowing stand-

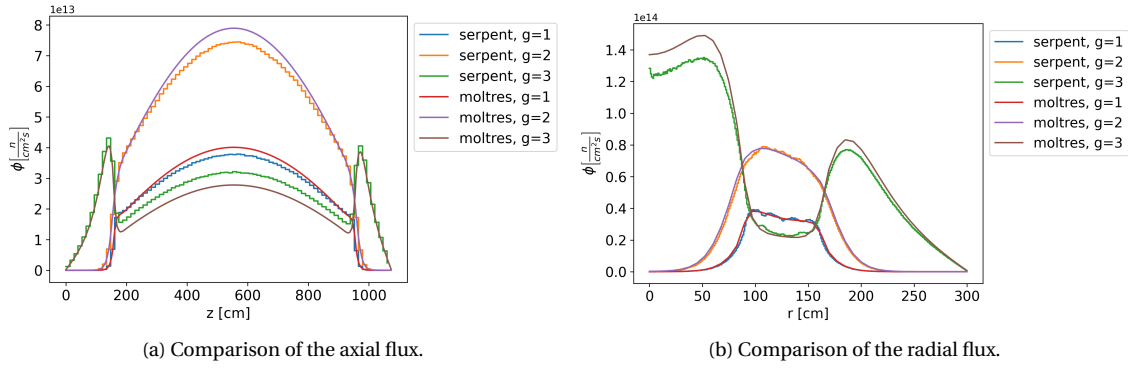


Figure 4.16: Comparison of the axial and radial fluxes calculated by Serpent and Moltres at 600 K.

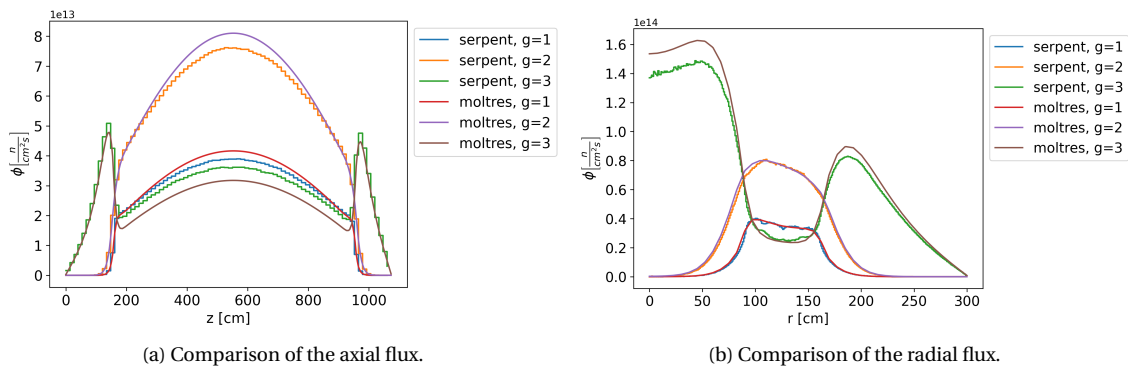


Figure 4.17: Comparison of the axial and radial fluxes calculated by Serpent and Moltres at 1200 K.

alone neutronic comparison without thermal-fluids feedback. The exercise requests the reporting of the global parameters:  $K_{eff}$ , control rod worth ( $\Delta\rho_{CR}$ ), axial offset ( $AO$ ), and the power distribution map [4]. Equations 4.8 and 4.9 define  $\Delta\rho_{CR}$  and  $AO$

$$\Delta\rho_{CR} = \frac{k_{eff,out} - k_{eff,in}}{k_{eff,out}k_{eff,in}} \quad (4.8)$$

where

$\Delta\rho_{CR}$  = control rod worth [-]

$k_{eff,out}$  = eigenvalue with control rod (CR) out (at position z=911.7 cm) [-]

$k_{eff,in}$  = eigenvalue with CR in (at position z=99 cm) [-]

and

$$AO = \frac{P_{top} - P_{bottom}}{P_{top} + P_{bottom}} \quad (4.9)$$

where

$AO$  = axial offset [-]

$P_{top}$  = total power produced in the top half core [W]

$P_{bottom}$  = total power produced in the bottom half core [W].

The Moltres simulation modeled  $1/3^{rd}$  of the reactor, shown in Figure 4.18, including the bottom and top reflectors. Two hundred and thirty-two hexagonal subdomains comprised the core, for which the benchmark provides group constants. The simulations required two meshes: one for the control rod out and one for the control rod in. The control out simulation had  $2.7 \times 10^5$  DoFs per energy-group, and a total of  $7.0 \times 10^6$  DoFs, while the control rod in simulation had  $2.3 \times 10^5$  DoFs per energy-group, and a total of  $5.9 \times 10^6$  DoFs. The Moltres simulations obeyed an eigenvalue convergence tolerance of  $1 \times 10^{-8}$ .

The benchmark exercise specifies the group constants and a map with their location. The benchmark definition used DRAGON-4 [111] to obtain the group constants from a full block configuration. The dataset contains 26 energy groups. Because the benchmark group constant format differs from the Moltres format, I made a Python script to handle the differences as part of this thesis. The benchmark specifies the following group constants:  $\Sigma_g^t$ ,  $D_g$ ,  $v\Sigma_g^f$ ,

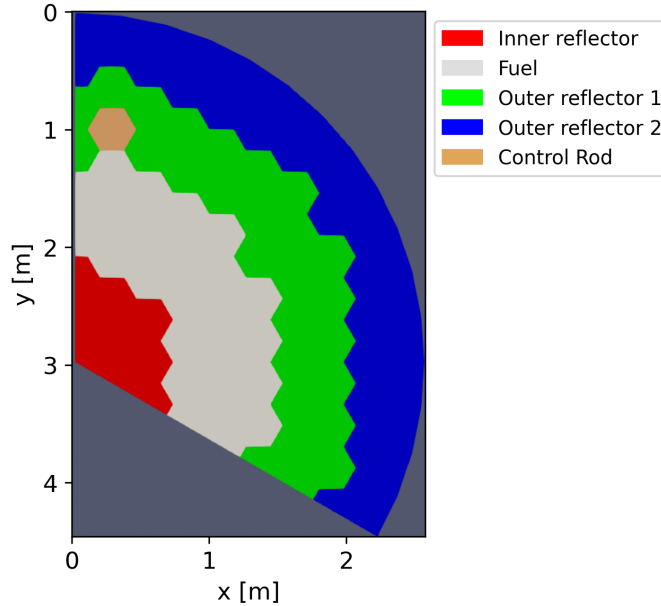


Figure 4.18: Moltres model, 1/3<sup>rd</sup> section of the MHTGR-350.

$\Sigma_g^f$ ,  $\chi_g^t$ , and  $\Sigma_{g' \rightarrow g}^s$  (see equation 3.1).

The benchmark exercise sets periodic boundary conditions (BCs) on the sides of the geometry; however, a memory issue did not allow for implementing those BCs in our 26-group Moltres input file. Moltres simulations approximated the periodic BC with the reflective BC. Section 4.3.1 discusses further the use of periodic and reflective BCs.

On average, the simulations took 4.22 hours using 1024 cores. Table 4.6 shows the main results. These include: Moltres predicting a  $k_{eff}$  larger than the reference result, a reactivity disparity 9 pcm, Moltres yielding a smaller control rod worth (the difference being 312 pcm), and the axial offset for the Moltres simulation being 4% higher than the reference result. The use of the reflective BCs instead of the periodic BCs may be the cause of the discrepancies. Once again, Section 4.3.1 discusses further the use of periodic and reflective BCs.

Table 4.6: Global parameters.

Parameter	Benchmark	Moltres
$k_{eff,out}$	1.06691	1.06804
$\Delta\rho_{CR}$ [pcm]	822.1	509.8
AO	0.168	0.1753

Figure 4.19 shows the radially averaged axial power distribution. Figure 4.20 shows the axially averaged radial power distribution. In both figures, Moltres' values are similar to the reference results. Moltres' power distribution in the inner ring is larger. The differences are within  $0.25 \text{ W/cm}^3$ .

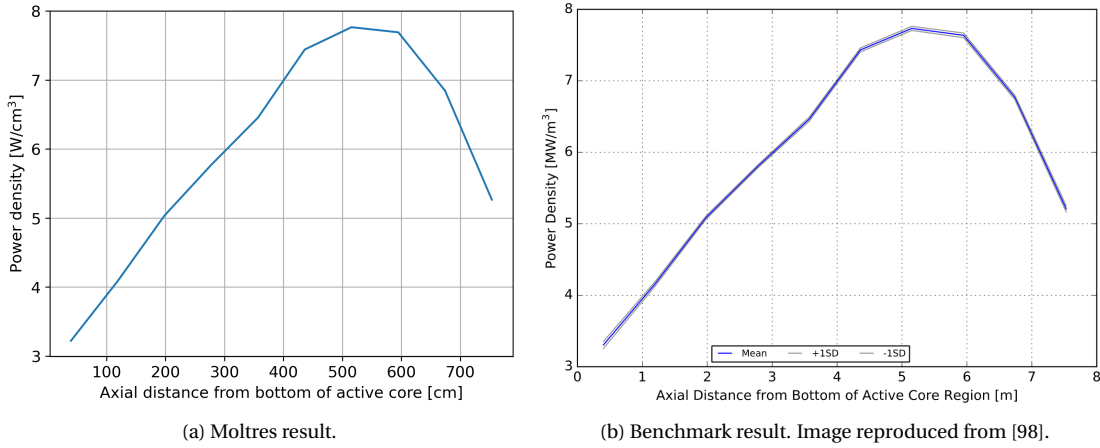


Figure 4.19: Comparison between the radially averaged axial power distribution calculated by Moltres and the benchmark published result [98].

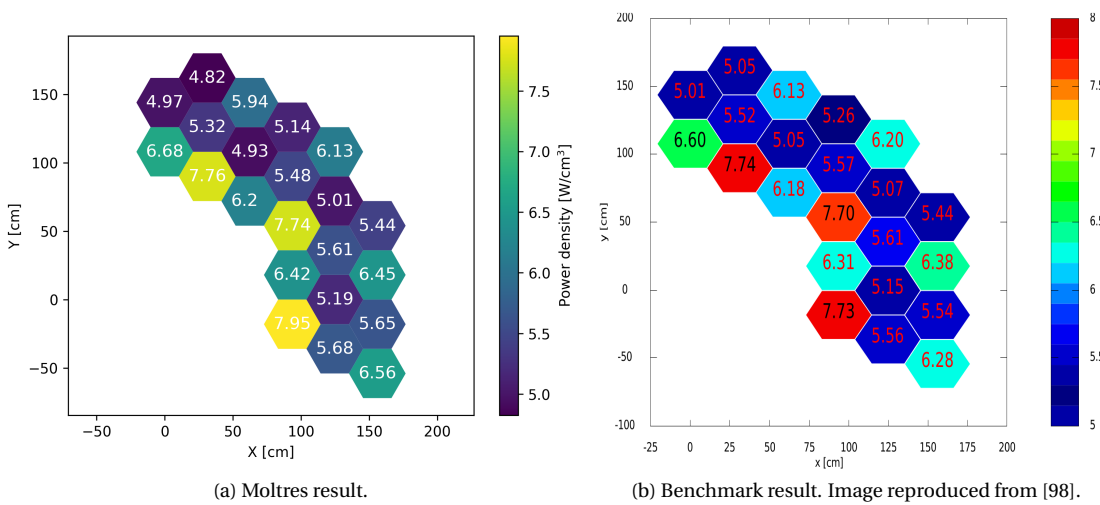


Figure 4.20: Comparison between the axially averaged radial power distribution calculated by Moltres and the benchmark published result [98].

### 4.3.1 Periodic vs Reflective Boundary Conditions

In the last section, we observed deviations in Moltres results for the Phase I Exercise 1 of the OECD/NEA MHTGR-350 Benchmark. This section analyzes the discrepancies that the reflective BC approximation may have introduced in the simulations. As the previous section mentioned, the simulation's memory requirements restrict the use of periodic BCs. A Python script collapsed the group constants to a smaller number of energy groups to reduce the memory requirements (refer to Section 9.2 for further detail on group constants handling). The simulations used 3- and 6-energy group structures (see Table 4.2).

The simulations required two meshes each: one for the control rod out and one for the control rod in. The 3-energy group simulation had  $6.2 \times 10^4$  DoFs per energy-group (total of  $1.9 \times 10^5$  DoFs) and  $6.2 \times 10^4$  DoFs per energy-group (total of  $1.8 \times 10^5$  DoFs) for the control rod out and the control rod in simulations, respectively. The 6-group simulation had  $1.7 \times 10^4$  DoFs per energy-group (total of  $1.0 \times 10^5$  DoFs) and  $1.9 \times 10^4$  DoFs per energy-group (total of  $1.1 \times 10^5$  DoFs) for the control out and the control rod in simulations, respectively. The 6-group simulation had to use a coarser mesh; otherwise, it would not run. This fact confirmed the suspicion that the simulation's memory requirements prevented it from running.

Table 4.7 compares the results from the simulations using periodic and reflective BCs.  $k_{eff}$  rises with the reflective BC. With the control rod out, the raise is small, while with the control rod in, the increase is considerable. The combined effect of both increases leads to a decrease in the control rod worth. The BC approximation barely affects the axial offset.

Table 4.7: Global parameter comparison for different types of BCs.

Energy groups	Type of BCs	$k_{eff,out}$	$k_{eff,in}$	$\Delta\rho_{CR}$ [pcm]	AO
3	Periodic	1.07571	1.06776	692.6	0.237
	Reflective	1.07586	1.07021	490.5	0.237
6	Periodic	1.07182	1.06356	724.3	0.185
	Reflective	1.07197	1.06610	513.3	0.186

## 4.4 Conclusions

This chapter addressed several objectives of this thesis by presenting the results of several stand-alone neutronics simulations of prismatic HTGRs using Moltres.

The preliminary studies focused on several aspects of the simulations. The first aspect was the effect of distributing the fuel compact isotopes homogeneously in the Serpent model. The results showed that the fuel compact isotopes' homogenization decreased the multiplication factor considerably and that the heterogeneous

calculation took 28% longer. Additionally, the homogeneous distribution appeared not to have a substantial impact on the group constants. However, the multiplication factor's considerable difference suggested that the combined effect of the group constants' small variations was significant. Although explicit modeling of the TRISO particles is time-consuming, it is necessary.

The next section studied the problem set-up in Moltres. Previous work used Moltres for simulating MSRs, which allow for heterogeneous diffusion calculations. This work aimed to use Moltres to solve prismatic HTGRs using a heterogeneous diffusion calculation. Nevertheless, the diffusion approximation fails to properly model regions where the mean free path is comparable to the region's dimensions. The presence of helium in the prismatic HTGR fuel assembly challenges some of the diffusion theory assumptions. Based on this discussion, this work adopted a homogeneous diffusion calculation scheme for Moltres simulations.

Focusing on a fuel column of the MHTGR-350, Section 4.2.1 investigated the effects of the energy group structure on the diffusion calculations. The analysis considered four operational cases: a fuel column without burnable poisons and a fuel column with burnable poisons, both cases at 600K and 1200K. The first study compared the Moltres-derived axial flux to Serpent-derived axial flux. Overall, the axial fluxes showed good agreement. A different study focused on the effects of the energy group structure on the  $k_{eff}$ . The number of energy groups did not affect the accuracy of the Moltres eigenvalue calculations. Another study compared the  $L_2$ -norm of the axial flux relative difference in the active core using various energy group structures. For the four operational cases, increasing the number of energy groups improved accuracy. The last study concerning the fuel column analyzed the impact of using different 15-energy group structures on the  $L_2$ -norm of the axial flux relative error. The  $L_2$ -norm of the various operational cases responded differently to the various 15-energy group structures. The analysis concluded that the 15d energy group structure was the best-performing one.

Section 4.2.2 compared Moltres full-core model results to Serpent reference results for two operational temperatures: 600K and 1200K. The first analysis compared the eigenvalues calculated by Serpent and Moltres — Moltres results were bigger, but the overall differences were less than 300 pcm. The second analysis compared the radial power distributions from both applications, whose maximum difference was 0.27 MW and located in the inner ring. The last analysis of the section compared Moltres and Serpent fluxes in two directions (axial and radial) in arbitrary core regions. The axial fluxes showed small discrepancies, mostly in their magnitude. The radial fluxes were close in shape and magnitude; however, the radial flux in the diffusion calculation failed to capture the flux variation near the burnable poisons. For the most part, Moltres axial and radial fluxes showed proximity to the Serpent's results.

Section 4.3 describes the results of Phase I Exercise 1 of the OECD/NEA MHTGR-350 Benchmark using Moltres. The group constants of the exercise have a 26-energy group structure, and the exercise sets periodic BCs on the sides of the geometry. The simulation's high memory requirements challenged such implementation in Moltres.

The simulations approximated the periodic BC with a reflective BC to reduce the memory requirements. Two out of three global parameters exhibited good agreement with the reference results; however, the control rod worth presented a large discrepancy, resulting from the BC approximation. Reducing the problem's size by collapsing the group constants to 3 and 6-energy groups, we compared the  $k_{eff}$  using the periodic and reflective BCs. A reflective BC for the CR out case did not substantially impact the  $k_{eff}$ , but the BC choice for the control rod in case had a significant effect. Their combined effect led to a large error in the control rod worth, while it had only a small influence on the axial offset.

This chapter met several objectives of this thesis by demonstrating Moltres' ability to predict HTGR neutronics, analyzing the impact of the energy group structure on the diffusion calculations, and calculating the power distribution of HTGRs properly.

# Chapter 5

## Thermal-fluids

This chapter focuses on the thermal-fluids modeling of prismatic HTGRs using Moltres. This chapter comprehends the following sections: Section 5.1 presents a verification and validation of the model in simplified geometries, Section 5.2 discusses the implementation of the model in a fuel column of a prismatic HTGR, Section 5.3 describes various efforts in conducting Phase I Exercise 2 of the OECD/NEA MHTGR-350 Benchmark, Section 5.4 introduces a simplified coupling scheme to solve Phase I Exercise 3 of the benchmark, and Section 5.5 concludes the chapter with a summary and the main points of the chapter.

### 5.1 Preliminary studies

This section describes various preliminary studies using Moltres and MOOSE heat conduction modules (Moltres/MOOSE) to simulate the heat transfer in prismatic HTGRs.

#### 5.1.1 Verification of the thermal-fluids model

This section analyzed a simplified cylindrical model whose analytical solution is known to verify the thermal-fluids model adopted in this work (see Section 10.1 for a description of the analytical solution). Moltres/MOOSE obtained the numerical solution of the thermal-fluid equations from Section 3.2.2.

Figure 5.1 displays the model geometry, which differentiates five subregions: fuel compact, helium gap, moderator, film, and coolant. Table 5.1 summarizes the geometry dimensions and the input parameters. The model reference design was the GT-MHR. The calculated moderator radius is the minimum distance between the fuel and coolant channels in the unit cell — the fuel/coolant pitch minus the fuel compact and coolant channel radii. The calculated coolant radius preserves the coolant channel volume. The model assumed a sinusoidal power profile in the  $z$ -direction.

Note that this is a simplified model only for verifying that the numerical solution agrees with the analytical solution. Figure 5.2 shows the axial and radial temperature profiles and demonstrates that both the analytical and numerical solutions exhibit good agreement. The outlet coolant temperature is 770.2 °C, whereas the maximum

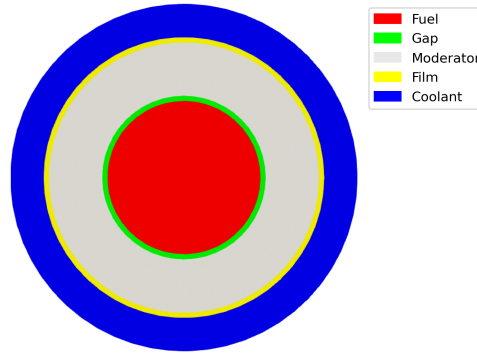


Figure 5.1: Model geometry axial layout.

Table 5.1: Problem characteristics.

Parameter	Symbol	Value	Units	Reference
Fuel compact radius	$R_f$	0.6225	cm	[76]
Fuel channel radius	$R_g$	0.6350	cm	[76]
Coolant channel radius	-	0.7950	cm	[76]
Fuel/coolant pitch	-	1.8850	cm	[76]
Fuel column height	L	793	cm	[76]
Coolant mass flow rate	$\dot{m}$	0.0176	$\text{kg} \cdot \text{s}^{-1}$	[76]
Average power density	$q_{ave}$	35	$\text{W} \cdot \text{cm}^{-3}$	[76]
Coolant inlet temperature	$T_{in}$	400	$^{\circ}\text{C}$	[76]
Helium inlet pressure	P	70	bar	[76]
Helium density	$\rho_c$	$4.940 \times 10^{-6}$	$\text{kg} \cdot \text{cm}^{-3}$	[112]
Helium heat capacity	$c_{p,c}$	5188	$\text{J} \cdot \text{kg}^{-1} \cdot \text{K}^{-1}$	[112]
Fuel compact thermal conductivity	$k_f$	0.07	$\text{W} \cdot \text{cm}^{-1} \cdot \text{K}^{-1}$	[27]
Gap thermal conductivity	$k_g$	$3 \times 10^{-3}$	$\text{W} \cdot \text{cm}^{-1} \cdot \text{K}^{-1}$	[27]
Moderator thermal conductivity	$k_m$	0.30	$\text{W} \cdot \text{cm}^{-1} \cdot \text{K}^{-1}$	[27]
Calculated parameters				
Calculated moderator radius	$R_m$	1.080	cm	-
Coolant film radius	$R_{cf}$	1.090	cm	-
Calculated coolant radius	$R_c$	1.349	cm	-
Coolant average velocity	$v_c$	1794.33	$\text{cm} \cdot \text{s}^{-1}$	-
Film thermal conductivity	$k_{cf}$	$1.722 \times 10^{-3}$	$\text{W} \cdot \text{cm}^{-1} \cdot \text{K}^{-1}$	-

fuel temperature is 874.7 °C.

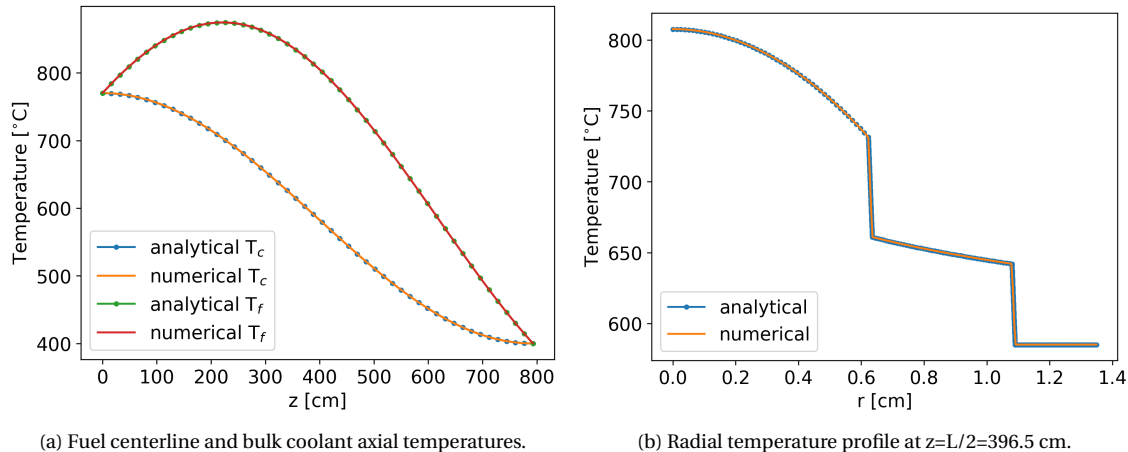


Figure 5.2: Comparison of the analytical and numerical temperature profiles.

### 5.1.2 Unit cell problem

This section solved the unit cell problem in the hot spot of the GT-MHR, which is the spot in the core with the largest power density. This section intended to reproduce the results found by In et al. [76] to validate the unit-cell model. I chose this article because it solves a three-dimensional unit-cell model and gives one of the most thorough descriptions in the open literature. Table 5.2 presents the problem characteristics. The article does not specify the solid's material properties, so the model used parameters from Tak et al. 2008 [27]. Figure 5.3 displays the model geometry, and Figure 5.4 the temperature-dependent material properties. Additionally, In et al. used a chopped cosine as the power profile, which the model used the average value of to simplify the analysis.

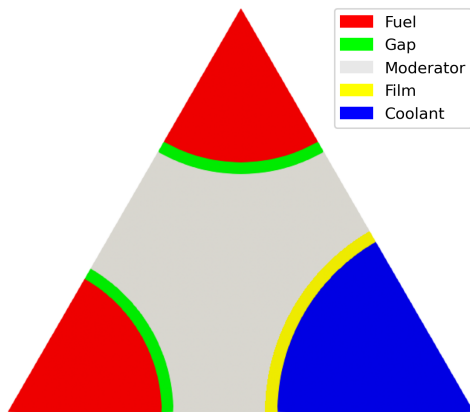


Figure 5.3: Axial layout of the model geometry.

Table 5.2: Problem characteristics.

Parameter	Symbol	Value	Units	Reference
Fuel compact radius	$R_f$	0.6225	cm	[76]
Fuel channel radius	$R_g$	0.6350	cm	[76]
Coolant channel radius	$R_c$	0.7950	cm	[76]
Fuel/coolant pitch	$p$	1.8850	cm	[76]
Fuel column height	$L$	793	cm	[76]
Coolant channel mass flow rate	$\dot{m}$	0.0176	$\text{kg} \cdot \text{s}^{-1}$	[76]
Average power density	$q_{ave}$	35	$\text{W} \cdot \text{cm}^{-3}$	[76]
Inlet coolant temperature	$T_{in}$	400	°C	[76]
Helium inlet pressure	$P$	70	bar	[76]
Helium density	$\rho$	$4.94 \times 10^{-6}$	$\text{kg} \cdot \text{cm}^{-3}$	[112]
Helium heat capacity	$c_p$	5188	$\text{J} \cdot \text{kg}^{-1} \cdot \text{K}^{-1}$	[112]
Calculated parameters				
Coolant film radius	$R_{cf}$	0.8050	cm	-
Coolant average velocity	$v_c$	1794.33	$\text{cm} \cdot \text{s}^{-1}$	-
Film thermal conductivity	$k_{cf}$	$1.731 \times 10^{-3}$	$\text{W} \cdot \text{cm}^{-1} \cdot \text{K}^{-1}$	-

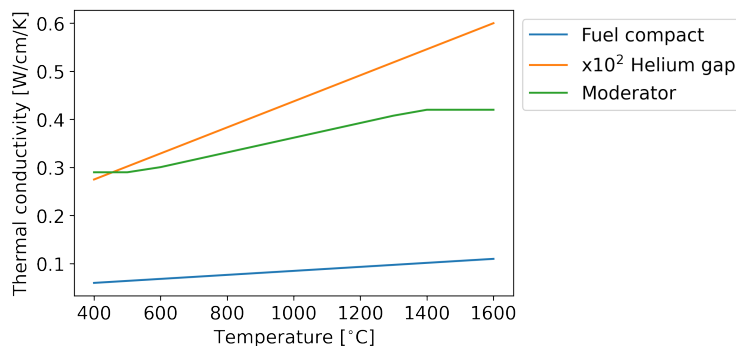


Figure 5.4: Temperature-dependent material properties [27].

Figure 5.5 shows the temperature profiles. From the top to the bottom of the reactor, the axial temperatures increase, the moderator and coolant temperatures remain parallel, and the difference between the fuel and moderator temperatures decreases. The model assumes a film thermal conductivity independent of the temperature; thus, the moderator-to-coolant temperature difference is constant. The solids' thermal conductivity increases with temperature; as shown in Figure 5.4, the thermal resistance between the moderator and the fuel decreases, so their temperature difference decreases as well.

Table 5.3 summarizes the results. Equation 5.1 evaluates the relative difference to the reference results

$$\Delta_T = \left| \frac{T_M - T_{ref}}{T_{ref}} \right| \cdot 100 \quad (5.1)$$

where

$\Delta_T$  = relative difference [%]

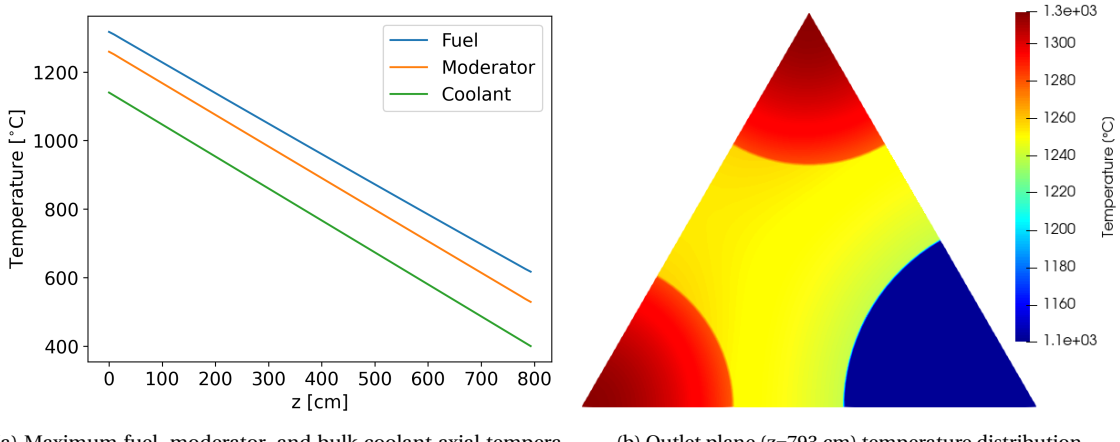
$T_M$  = temperature determined by this work [ $^{\circ}$ C]

$T_{ref}$  = reference temperature [ $^{\circ}$ C].

Small discrepancies arise in the results: Moltres/MOOSE coolant temperature is smaller than In's by  $4^{\circ}$ C. The moderator temperature is larger by  $9^{\circ}$ C, and the fuel temperature is larger by  $22^{\circ}$ C. The cause of the fuel temperature discrepancy is the power profile simplification. As the previous section's analysis has shown, the fuel-to-coolant temperature difference is small in the outlet for a sinusoidal power profile. The opposite extreme scenario is the uniform power profile, where the fuel-to-coolant temperature difference is larger. In et al. used a chopped cosine power profile, which is between the two former cases. Hence, this model yields a fuel-to-coolant temperature difference at the outlet larger than In et al. Overall, Moltres results are close to In's results as the maximum difference between them is  $22^{\circ}$ C, which corresponds to less than 2% relative difference.

Table 5.3: Comparison between In et al. [76] and Moltres/MOOSE results.

Parameter	In et al. [ $^{\circ}$ C]	Moltres/MOOSE [ $^{\circ}$ C]	$\Delta_T$ [%]
Maximum coolant temperature	1144	1140	0.3
Maximum moderator temperature	1250	1259	0.7
Maximum fuel temperature	1295	1317	1.7



(a) Maximum fuel, moderator, and bulk coolant axial temperatures.  
(b) Outlet plane ( $z=793$  cm) temperature distribution.

Figure 5.5: Unit cell temperature profile calculated by Moltres.

## 5.2 Fuel column

This section discusses an HTGR fuel column analysis aimed at validating the fuel column model by reproducing some of Sato et al. [79] analyses. I use this article because it gives a thorough description of the problem, making it easier to reproduce. A first analysis studied a column with no bypass-gap between assemblies, while a second analysis studied a column with a 3mm bypass-gap between assemblies.

Figure 5.6 exhibits model geometry. The model only considered a  $1/12^{th}$  portion of the column due to symmetry. The study used the GT-MHR as the reference reactor for the calculations. The GT-MHR shares the geometry dimensions with the MHTGR, which Table 3.3 specifies.

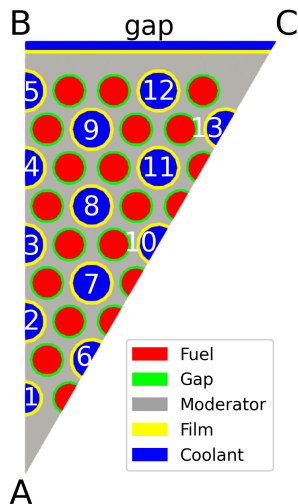


Figure 5.6: Model geometry axial layout.

Equation 5.2 evaluates the solid material properties [113]

$$\phi(T) = A_1 + A_2 T + A_3 T^2 + A_4 T^3 + A_5 T^4. \quad (5.2)$$

Table 5.4 displays the fuel compact and moderator coefficients of equation 5.2.

Table 5.4: Thermal conductivity coefficients [113].

Temperature range [K]	Moderator			Fuel compact
	255.6-816	816-1644.4	1644.4-1922.2	255.6-2200
A1	28.6	$1.24 \times 10^2$	41.5	3.94
A2		$-3.32 \times 10^{-1}$		$3.59 \times 10^{-3}$
A3		$4.09 \times 10^{-4}$		$-1.98 \times 10^{-9}$
A4		$-2.11 \times 10^{-7}$		$3.19 \times 10^{-12}$
A5		$4.02 \times 10^{-11}$		$-9.77 \times 10^{-16}$

Table 5.5 lists the remaining input parameters. The model assigns a number to each coolant channel and the bypass-gap, as shown in Figure 5.6. The calculations adopted the mass flow distribution from Sato et al [79], shown in Table 5.6.

Table 5.5: Constant problem characteristics.

Parameter	Symbol	Value	Units	Reference
Inlet coolant temperature	$T_{in}$	490	°C	[79]
Helium inlet pressure	P	70	bar	[79]
Helium density	$\rho$	$4.37 \times 10^{-6}$	$\text{kg} \cdot \text{cm}^{-3}$	[112]
Helium heat capacity	$c_p$	5188	$\text{J} \cdot \text{kg} \cdot \text{K}$	[112]
Average power density	$q_{ave}$	27.88	$\text{W} \cdot \text{cm}^{-3}$	[79]
<hr/>				
Calculated parameters				
Coolant film radius	$R_{cf}$	0.804	cm	-
Film thermal conductivity	$k_{cf}$	$2.09 \times 10^{-3}$	$\text{W} \cdot \text{cm}^{-1} \cdot \text{K}^{-1}$	-

Table 5.6: Mass flow rate determined from Sato's calculation [79]. Values expressed in [g/s].

Channel	1	2	3	4	5	6	7
No bypass-gap	6.18	11.34	11.37	11.38	11.43	11.33	22.70
3mm bypass-gap	5.88	10.80	10.85	10.91	11.08	10.80	21.58
Channel	8	9	10	11	12	13	Gap
No bypass-gap	22.73	22.73	11.38	22.77	22.91	11.44	-
3mm bypass-gap	21.67	21.83	10.88	21.81	22.20	11.10	16.56

Table 5.7 compares the results determined in this work using Moltres/MOOSE to Sato's results [79]. In the case with no bypass-gap, Moltres/MOOSE's maximum coolant temperature is 2 °C lower, and the maximum fuel

temperature is 4°C higher. In the case with a 3mm bypass-gap, Moltres/MOOSE's maximum coolant temperature is 2 °C lower, and the maximum fuel temperature is 1°C lower. The results are within the 1% difference to those in [79].

Figure 5.7 displays the outlet temperature along lines A-B and A-C from Figure 5.6. The bypass-flow reduces the peripheral temperature causing the center's temperature to rise. The presence of the gap between assemblies produces a larger temperature gradient in the assembly.

Table 5.7: Comparison of the maximum temperatures calculated by this work and the reference values from Sato et al. [79]. Temperature values expressed in [°C].

	No gap			3mm gap		
	$T_{ref}$	Moltres/MOOSE	$\Delta_T$ [%]	$T_{ref}$	Moltres/MOOSE	$\Delta_T$ [%]
Coolant	985	983	0.2	1007	1005	0.2
Fuel	1090	1094	0.4	1115	1114	0.1

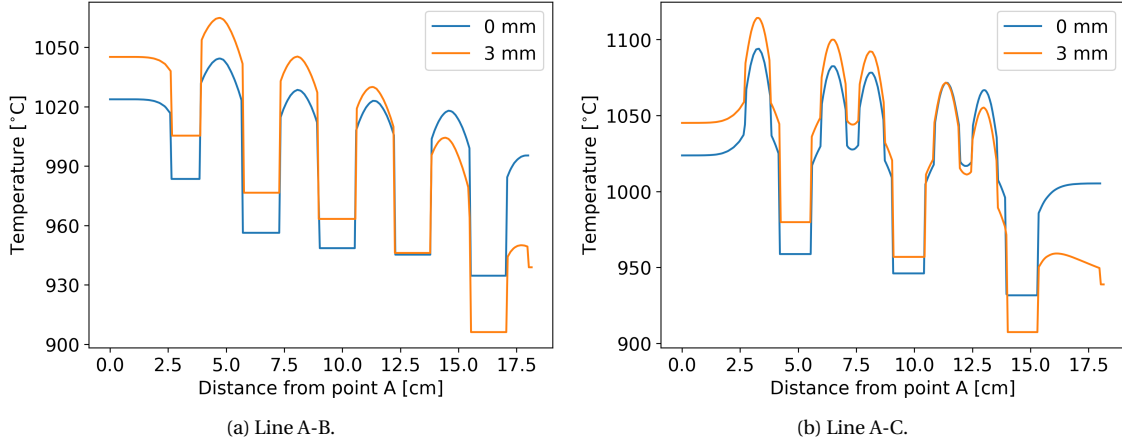


Figure 5.7: Outlet plane temperature along the line A-B and line A-C.

### 5.2.1 Flow distribution analysis

As described in Section 2.2, several methods are available to calculate the coolant flow distribution in prismatic HTGRs. This section compares a few such methods. The metrics chosen for this comparison are the maximum coolant and fuel temperatures and the mass flow distribution. The model assigns a number to each coolant channel and the bypass-gap (see Figure 5.6). Note that Channel 1 is a small coolant channel while Channels 2 to 13 are large coolant channels. This study adopted the mass flow distribution from Sato et al. [79] as the reference and analyzed the following cases:

- Case 1: uses a flat velocity profile (every channel and gap has the same velocity).

- Case 2: uses the incompressible flow model with temperature-independent helium viscosity.
- Case 3: uses the incompressible flow model with a temperature-dependent helium viscosity.
- Case 4: uses the low-Mach number model with a temperature-dependent helium viscosity.

Case 1 assumes a flat velocity profile in all coolant paths and calculated the mass flow using equation 5.3

$$\dot{m}_i = \frac{A_i}{\sum_j A_j} \dot{m}_T \quad (5.3)$$

where

$\dot{m}_i$  = channel  $i$  mass flow rate [ $kg \cdot s^{-1}$ ]

$A_i$  = channel  $i$  cross-sectional area [ $cm^2$ ]

$\dot{m}_T$  = total mass flow rate [ $kg \cdot s^{-1}$ ].

Case 2 and 3 used equation 5.4 [3] to calculate the pressure drop

$$\Delta P = \frac{\dot{m}_i^2}{\rho_i A_i^2} f \frac{2L}{D_h} \quad (5.4)$$

$$B_i = \frac{1}{\rho_i A_i^2} f \frac{2L}{D_h} \quad (5.5)$$

where

$\Delta P$  = pressure drop [ $Pa$ ]

$\rho_i$  = channel inlet coolant density [ $kg \cdot m^{-3}$ ]

$f$  = friction factor [-]

$L$  = channel length [ $m$ ]

$D_h$  = hydraulic diameter [ $m$ ].

Case 3 differs from Case 2 as the friction factor  $f$  depends on the average channel temperature. Case 4 used

equation 5.6 [3] to calculate the pressure drop

$$\Delta P = \frac{\dot{m}_i^2}{2\rho_i A_i^2} \left[ \frac{4fL(T_i + T_o)}{2DT_i} + \frac{T_o - T_i}{T_i} \right] \quad (5.6)$$

$$B_i = \frac{1}{2\rho_i A_i^2} \left[ \frac{4fL(T_i + T_o)}{2DT_i} + \frac{T_o - T_i}{T_i} \right] \quad (5.7)$$

where

$T_i$  = channel inlet coolant temperature [ $^{\circ}\text{C}$ ]

$T_o$  = channel outlet coolant temperature [ $^{\circ}\text{C}$ ].

(5.8)

Equations 5.4 and 5.6 used an iterative solver to obtain  $\dot{m}_i$  [3](for further detail refer to Section 8.3)

$$B_i^{(n)} = f\left(\dot{m}_i^{(n)}\right) \quad (5.9)$$

$$\Delta P^{(n)} = \frac{\dot{m}_T}{\sum_i \frac{1}{\sqrt{B_i^{(n)}}}} \quad (5.10)$$

$$\dot{m}_i^{(n+1)} = \sqrt{\frac{\Delta P^{(n)}}{B_i^{(n)}}} \quad (5.11)$$

with a convergence criterion of

$$|\Delta P^{(n+1)} - \Delta P^{(n)}| < 10^{-4}. \quad (5.12)$$

The solution of Cases 3 and 4 depend on temperature, requiring a second level of iterations that updates the material properties for the computed temperatures. The convergence criteria were  $1^{\circ}\text{C}$  for the maximum coolant and fuel temperatures. A Python script external to Moltres holds these iterative solvers.

Table 5.8 displays the results achieved in this thesis for the mass flow rates. Equation 5.13 evaluates the relative difference to the reference results

$$\Delta_m = \left| \frac{\dot{m}_i - \dot{m}_{r,i}}{\dot{m}_{r,i}} \right| \cdot 100 \quad (5.13)$$

where

$\Delta_m$  = relative difference [%]

$\dot{m}_i$  = channel  $i$  mass flow rate determined by this work [ $g \cdot s^{-1}$ ]

$\dot{m}_{r,i}$  = reference mass flow rate [ $g \cdot s^{-1}$ ].

Case 1 yields the largest differences to reference results, yielding a 13.3% difference to the reference small coolant channel mass flow. Additionally, Case 1 yields the smallest large coolant channel mass flow, the differences being within 6.2%. Case 2 and 3 results are within the 3.3% difference to the reference results. Case 2 and 3 barely differ, proving that not considering the viscosity's temperature dependency yields a more straightforward method with acceptable accuracy. Case 4 results are within 1% of the reference results except for the gap mass flow that yields a difference of 4.2%. For the most part, Case 4 arrives at the values closest to the reference solution. 

Table 5.9 summarizes the maximum temperatures and the relative difference to the reference values using equation 5.1. Case 1 yields the largest difference for the maximum coolant temperature, which is less than 10°C. Case 4 yields the results closest to the reference values, showing a difference of 0.2%. For the maximum fuel temperature, Case 1 and 4 yield the best results. Again, Case 2 and 3 results barely differ.

The low-Mach number model (Case 4) yielded the closest results to the reference solution. However, such a method required a two-level iterative solver. From a computational perspective, the Case 1 model is the most straightforward as it does not require an iterative solver. Additionally, the Case 1 model yields the simplest Moltres input file. For these reasons, the rest of the thesis adopts the flat velocity approximation for the fluid flow distribution.

### 5.2.2 Mesh convergence analysis

The remainder of this chapter intends to solve the full-core problem. This section aims to identify some possible problems introduced by the full-core problem's large mesh size requirement. This section studies a mesh convergence analysis of the full-fuel column problem. Figure 5.8 displays the model geometry, and Table 5.10 presents the results. The convergence criteria were 1°C for the maximum coolant and fuel temperatures. The coolant temperature converged for the fifth mesh, but the fuel temperature did not converge. Further refinement of the mesh was not possible as the simulation memory requirements were too high.

This analysis reveals a potential problem. The high level of detail in the geometry requires a large number of elements in the mesh. In the full-scale problem, the dimensions and the number of elements in the mesh both increase. This method will potentially be unable to solve the three-dimensional full-scale problem due to a high memory requirement. For this reason, the next section intends to solve the full-scale problem using a

Table 5.8: Comparison of the calculated flow rates and the reference values [79]. Mass flow rates values expressed in  $[g \cdot s^{-1}]$ .

Channel	Case 1			Case 2			Case 3			Case 4	
	$\dot{m}_{r,i}$	$\dot{m}_i$	$\Delta_m [\%]$								
1	5.88	6.66	13.3	5.98	1.7	5.97	1.5	5.83	0.9		
2	10.80	10.41	3.6	10.91	1.0	10.90	0.9	10.75	0.5		
3	10.85	10.41	4.1	10.91	0.6	10.90	0.5	10.81	0.4		
4	10.91	10.41	4.6	10.91	0.0	10.91	0.0	10.90	0.1		
5	11.08	10.41	6.0	10.91	1.5	10.92	1.4	11.09	0.1		
6	10.80	10.41	3.6	10.91	1.0	10.90	0.9	10.73	0.6		
7	21.58	20.82	3.5	21.82	1.1	21.80	1.0	21.58	0.0		
8	21.67	20.82	3.9	21.82	0.7	21.81	0.6	21.71	0.2		
9	21.83	20.82	4.6	21.82	0.0	21.83	0.0	21.92	0.4		
10	10.88	10.41	4.3	10.91	0.3	10.91	0.3	10.84	0.4		
11	21.81	20.82	4.5	21.82	0.0	21.82	0.0	21.87	0.3		
12	22.20	20.82	6.2	21.82	1.7	21.85	1.6	22.26	0.3		
13	11.10	10.41	6.2	10.91	1.7	10.92	1.6	11.08	0.2		
Half-gap	8.28	8.20	1.0	8.55	3.3	8.55	3.3	8.63	4.2		

Table 5.9: Comparison of the maximum temperatures between Moltres-derived and the reference results. Temperature values expressed in  $^{\circ}\text{C}$ .

	Case 1			Case 2			Case 3			Case 4	
	$T_{ref}$	T	$\Delta_T [\%]$	T	$\Delta_T [\%]$	T	$\Delta_T [\%]$	T	$\Delta_T [\%]$	T	$\Delta_T [\%]$
Coolant	1005	994	1.1	999	0.6	1000	0.5	1007	0.2		
Fuel	1114	1116	0.2	1109	0.4	1110	0.4	1116	0.2		

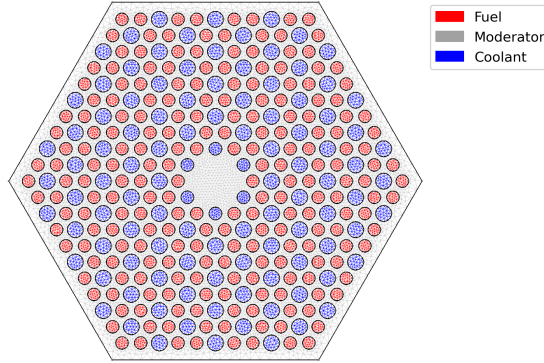


Figure 5.8: Axial view of the full-fuel column model geometry.

Table 5.10: Mesh characteristics and maximum temperatures of the full-fuel column model.

	Mesh 1	Mesh 2	Mesh 3	Mesh 4	Mesh 5
Number of elements [ $\times 10^6$ ]	1.025	1.306	1.833	2.596	3.006
Number of DoFs [ $\times 10^6$ ]	0.524	0.666	0.932	1.317	1.525
Maximum coolant temperature	1060.41	1062.23	1064.00	1065.13	1065.32
Maximum fuel temperature	1204.49	1217.32	1225.57	1233.44	1234.93

two-dimensional cylindrical model.

### 5.3 OECD/NEA MHTGR-350 Benchmark: Phase I Exercise 2

This section describes Phase I Exercise 2 of the OECD/NEA MHTGR-350 Benchmark [4] and the undertaking as part of this thesis to conduct it using Moltres. Phase I Exercise 2 defines a thermal-fluid stand-alone calculation. The exercise aims to ensure that the thermal-fluid model differences between participants are negligible and will not affect the coupled exercises. The benchmark specifies the power density of each fuel region and defines the type of mass flow distribution and material properties for four sub-cases:

- Exercise 2a: No bypass flow and fixed thermo-physical properties. The model does not account for the bypass flow, and the thermo-physical properties are constant.
- Exercise 2b: Bypass flow type I and fixed thermo-physical properties. This exercise prescribes the bypass flow distribution, and the thermo-physical properties are constant.
- Exercise 2c: Bypass flow type I and variable thermo-physical properties. This exercise prescribes the bypass flow distribution, and the thermo-physical properties depend on different simulation parameters.
- Exercise 2d: Bypass flow type II and variable thermo-physical properties. This exercise solves the bypass flow distribution through the explicit modeling of the bypass gaps. The thermo-physical properties depend on different simulation parameters.

The exercise requires reporting the average and maximum temperature values of the reflector, Reactor Pressure Vessel (RPV), fuel, moderator, and coolant. It also requires reporting the RPV heat flux and the mass flow rate distribution in the coolant channels and the bypass gaps. These data are helpful to trace the source of possible differences in the primary parameters between participants. Since OECD/NEA did not publish the results for this exercise, this section compares Moltres/MOOSE results against INL's benchmark results [57]. This section presents only a subset of available data that illustrate the main characteristics of the exercise.

Figure 5.9 displays the model geometry. The model uses several simplifications to conduct the exercise. In the axial direction, it does not consider the upper plenum and the outlet plenum, and the axial boundaries are the top reflector's upper face and the bottom reflector's lower face. The top reflector's upper face and the inlet coolant flow are at 259 °C, while the bottom reflector's lower face is adiabatic. The outlet coolant uses an outflow boundary condition. In the radial direction, the model does not consider the core barrel and the helium gap. The model includes the RPV, followed by the outside air. The outside air region outer boundary is at 30 °C.

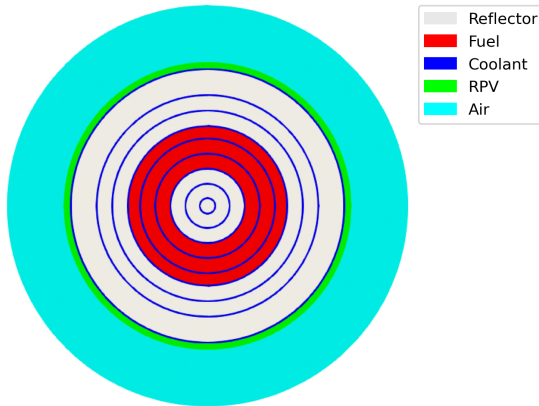


Figure 5.9: Phase I Exercise 2 model geometry for simulation in Moltres.

The core model geometry uses INL's model as the reference design. Nine rings define the solid structures in the core, and the other nine rings the coolant flow in the core. The radii of the rings preserve the assemblies' volume. The coolant thickness is constant for all the rings and preserves the coolant volume in the core. Table 5.11 presents the material properties. All the graphite regions assume the grade H-451 graphite material properties.

Table 5.11: Problem characteristics.

Parameter	Value	Units	Reference
Fuel compact thermal conductivity	20	$\text{W} \cdot \text{m}^{-1} \cdot \text{K}^{-1}$	[4]
Fuel block thermal conductivity	37	$\text{W} \cdot \text{m}^{-1} \cdot \text{K}^{-1}$	[4]
Graphite thermal conductivity	66	$\text{W} \cdot \text{m}^{-1} \cdot \text{K}^{-1}$	[4]
RPV thermal conductivity	40	$\text{W} \cdot \text{m}^{-1} \cdot \text{K}^{-1}$	[4]
Coolant thermal conductivity	0.41	$\text{W} \cdot \text{m}^{-1} \cdot \text{K}^{-1}$	[4]
Air thermal conductivity	0.068	$\text{W} \cdot \text{m}^{-1} \cdot \text{K}^{-1}$	[4]
Helium density	5.703	$\times 10^{-6} \text{ kg} \cdot \text{cm}^{-3}$	[112]
Helium heat capacity	5188	$\text{J} \cdot \text{kg}^{-1} \cdot \text{K}^{-1}$	[112]

Table 5.12 displays the results. The model considerably under-predicts the inner reflector rings temperature, while it over-predicts the coolant rings temperature. With the purpose of better understanding this behavior, Figure 5.10 shows the temperature across the reactor on the bottom of the active core ( $z=200 \text{ cm}$ ). This figure exposes that the temperatures in the active core are well above the other region temperatures. Although such behavior is expected, the temperature profile reveals some heat transfer disconnection between the different rings. In other words, the heat transfer from the fuel rings to the rest of the core structures is smaller than the heat transfer to the coolant rings in the active core region. This thermal disconnection causes the reflector temperatures to be too low and the coolant temperatures in the fuel rings too high. These results indicate that Moltres' model fails to capture some heat transfer mechanisms that INL's model captures. The most obvious difference between the models is the inclusion of the radiative heat transfer. Future Moltres development efforts will focus on confirming

this supposition and adding the capability to model the radiative heat transfer.

Table 5.12: Comparison of this work and INL [57] first bottom core level average temperatures.

	Reflector				Coolant	
	Ring 1	Ring 2	Ring 3	Ring 4	Ring 5	Ring 6
INL [°C]	790	794	802	797	636	673
Moltres/MOOSE [°C]	268	313	769	1424	1597	1157
$\Delta T [\%]$	66	61	4	79	151	72

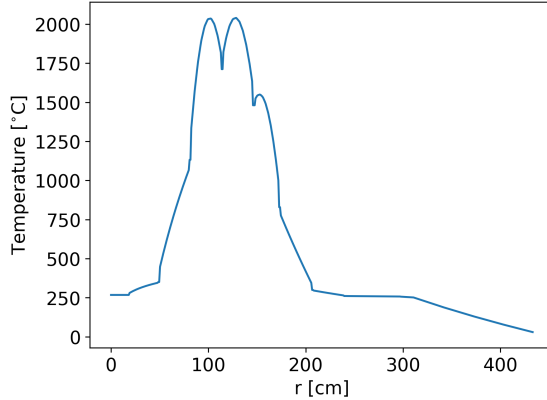


Figure 5.10: Radial temperature at the bottom of the active core ( $z=200$  cm) determined by Moltres.

To circumvent this barrier, the following analysis considered a second model based on Stainsby's approach [93]. The calculation used a global model to obtain the coolant temperature in the core and then a sub-channel model to get the fuel and moderator average temperatures. The sub-channel model used half of the unit cell from Section 5.1.2. Figure 5.11 displays the global model geometry. Three fuel rings represent the three rings of fuel assemblies in the MHTGR-350 (see Figure 3.1). In the middle of each fuel ring, a coolant ring defines the coolant flow in that fuel ring. The rings' radii preserve the assemblies' volume, and the coolant ring volumes preserve the coolant volume in each of the fuel rings. The model uses the material properties from Table 5.11.

Figure 5.12 presents the coolant and average solid temperatures in the different fuel rings. The coolant temperature increases from the top to the bottom of the active core, and it is constant in the bottom and top reflector regions. The highest coolant, fuel, and moderator temperatures are in Fuel Ring 1.

Table 5.13 compares Moltres/MOOSE results to INL's [57]. For the coolant temperature, Moltres results are 9.9% smaller in Fuel Ring 1, and 1.6% higher in Fuel Rings 2 and 3. Although the discrepancies are small, for some reason, the global model fails to correctly distribute the heat produced in the fuel rings into the coolant rings. A possible cause of this discrepancy is the flat velocity approximation. Section 5.2.1 showed that a flat velocity distribution of the coolant is reasonable in the fuel column model; however, one of the assumptions of that model was a uniform power density. In this exercise, the power density is not uniform, which could explain the

discrepancies. Further studies might confirm their cause.

Additionally, Moltres predicts a smaller coolant-to-moderator temperature difference for Fuel Rings 1 and 2. The most considerable discrepancy is in Fuel Ring 1. INL's model coolant-to-moderator temperature difference is 46°C while Moltres/MOOSE predicts a difference of 30°C. The flat velocity approximation might be again the source of these discrepancies. Finally, the moderator-to-fuel temperature differences from INL and Moltres/MOOSE are close. In Fuel Ring 1, the differences are 20°C and 22°C for INL and Moltres/MOOSE results. In fuel ring 2, the differences are 16°C and 17°C for INL and Moltres/MOOSE results.

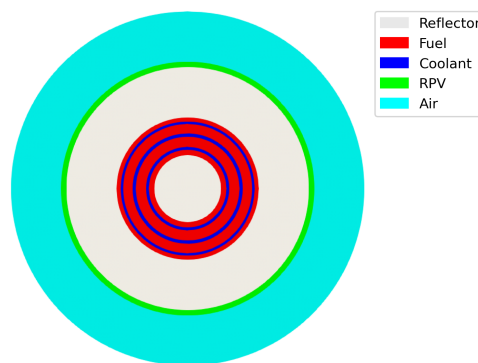


Figure 5.11: Model geometry.

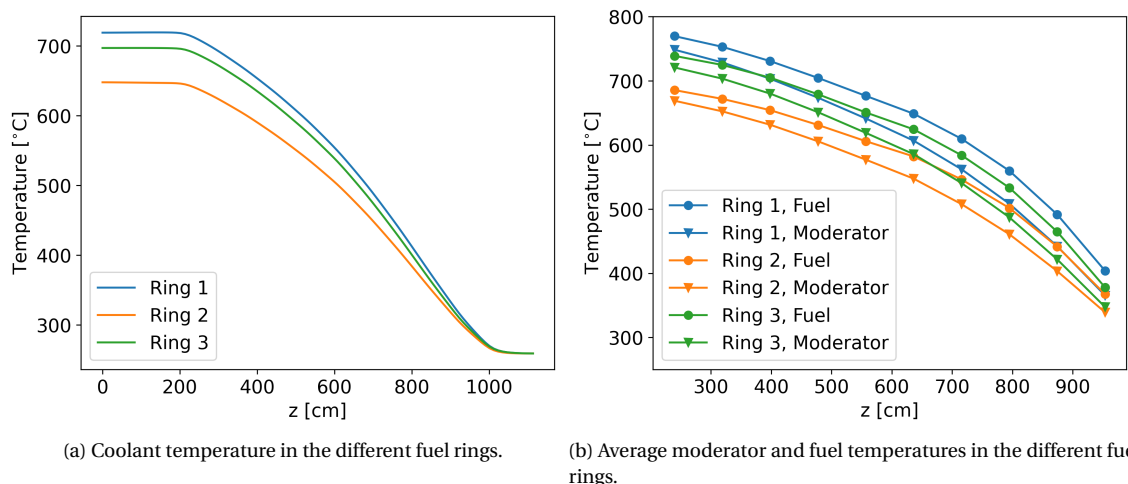


Figure 5.12: Axial temperatures determined by Moltres.

Table 5.13: Comparison of this work and INL [57] first bottom core level average temperatures. Temperature values expressed in  $^{\circ}\text{C}$ .

	Fuel Ring 1			Fuel Ring 2			Fuel Ring 3		
	Coolant	Moderator	Fuel	Coolant	Moderator	Fuel	Coolant	Moderator	Fuel
INL	797	843	863	636	672	688	673	Not shown	722
This thesis	718	748	770	646	669	686	696	721	739
$\Delta_T$ [%]	9.9	11.3	10.8	1.6	0.4	0.3	3.4	-	2.4

## 5.4 Coupled simulations

This section sets the roadmap for conducting neutronics and thermal-fluids coupled simulations of prismatic HTGRs in Moltres.

### 5.4.1 OECD/NEA MHTGR-350 Benchmark: Phase I Exercise 3

This section presents Phase I Exercise 3 of the OECD/NEA MHTGR-350 Benchmark and describes the exercise conducted with Moltres/MOOSE. Exercise 3 combines all the data from the first two exercises of the benchmark, in which the participants need to determine a coupled neutronic and thermal-fluids solution. The exercise requires the reporting of the same parameters reported in Exercises 1 and 2 combined. The benchmark specifies the group constants necessary to conduct the exercise. The group constants depend on four state parameters: moderator ( $T_m$ ) and fuel temperature ( $T_f$ ) and xenon-135 ( $C_{Xe}$ ) and hydrogen concentration ( $C_H$ ). In addition to these data, the benchmark provides fluence maps to determine the thermal conductivity of graphite.

Two sub-cases compose Exercise 3:

- Exercise 3a: Same thermal-fluids problem definition from Exercise 2c. This exercise prescribes the bypass flow distribution and the thermo-physical properties depend on the temperature and fluence.
- Exercise 3b: Same thermal-fluids problem definition from Exercise 2d. This exercise solves the bypass flow distribution through the explicit modeling of the bypass gaps. The thermo-physical properties depend on the temperature and fluence.

Section 5.3 solved the thermal-fluids stand-alone problem using a global and a sub-channel model. Those simulations required running two separate input files, where the output of the global model served as an input to the sub-channel model. Exercise 3 requires modeling the temperature feedback. Using the Section 5.3 approach for the temperature feedback would require the fully-coupled simulation of both input files. However, MOOSE framework did not have the capability to couple these specific input files when carrying out this exercise.

To solve Exercise 3, I used a simplified global model, requiring the simulation of only one input file. The global model homogenizes the fuel and moderator materials. The explicit modeling of the fuel in the global model requires

the conversion of the fuel dimensions in the three-dimensional geometry to the simplified cylindrical model. This conversion requires the conservation of two parameters: the fuel volume and the fuel thickness. The fuel volume preservation ensures that the reactor power does not change in the approximation. On the other hand, the maximum fuel temperature is sensitive to the fuel thickness, requiring conservation. A cylindrical model cannot preserve both parameters simultaneously, and the global model homogenizes the fuel and moderator materials. Hence, the solution of this model did not differentiate between moderator and fuel.

Figure 5.13 presents the model geometry. The model includes 28 fuel and 29 coolant rings. I calculated the radii of the rings by preserving the assemblies' and the coolant volume. The coolant ring pitch is the coolant channel pitch in a fuel assembly. Exercise 3a requires using material properties from Exercise 2c. This simplified model used the material properties from Exercise 2a, as shown in Table 5.11. Regarding the group-constants, the benchmark prescribes them for 232 regions in the reactor. Table 5.14 shows what benchmark sub-domains integrate each model region. The model did not include the control rod region (sub-domain 232). The simulations used a three energy-group structure. Table 5.15 indicates what benchmark group numbers integrate each model group. Conducting this exercise required developing a Python tool to translate the benchmark group constants to Moltres format. The tool was responsible for homogenizing and collapsing the group constants as well. For further detail on the group constants handling, refer to Sections 9.1 to 9.3. The problem assumed the same boundary conditions from Section 5.3.

Because Moltres can decouple the neutronics from the thermal-fluid effects, and for the sake of comparison, I conducted the exercise with and without thermal feedback. The calculations without thermal feedback assumed the group constants at 550 °C. Figure 5.14 and 5.15 display the results on two arbitrarily located lines across the core, axial line on  $r = 85\text{cm}$  and radial line on  $z = 556.5\text{cm}$ . The thermal feedback affects the flux, which consequently affects the thermal-fluids. The axial flux peak moves towards the reactor top, where the temperatures are lower than the bottom. Thus, the heat production shifts towards the reactor top, and the temperatures near the reactor outlet decrease. The radial temperature profile has a similar shape to the thermal flux, as this group is the main contributor to fission and thus the power profile. The radial flux does not change considerably; hence the temperature profile does not change much either. The thermal feedback moves the radial temperature profile up because the heat production shifts towards the top.

### 5.4.2 Discussion

This section analyzes Moltres' flaws in conducting prismatic HTGR coupled simulations. Moltres' initial development targeted MSRs, allowing them to rely on heterogeneous diffusion calculations. In a heterogeneous solver, each mesh node holds the information of each variable. In an MSR simulation, Moltres defines the neutron flux and the

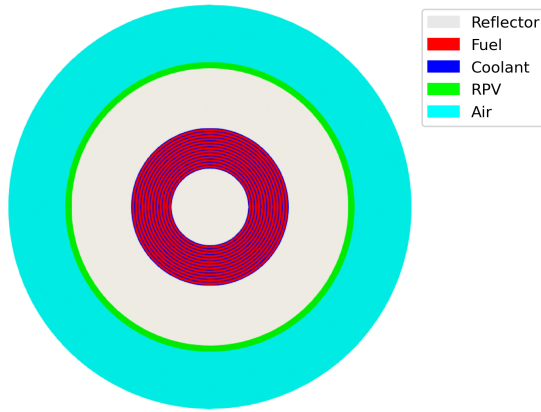


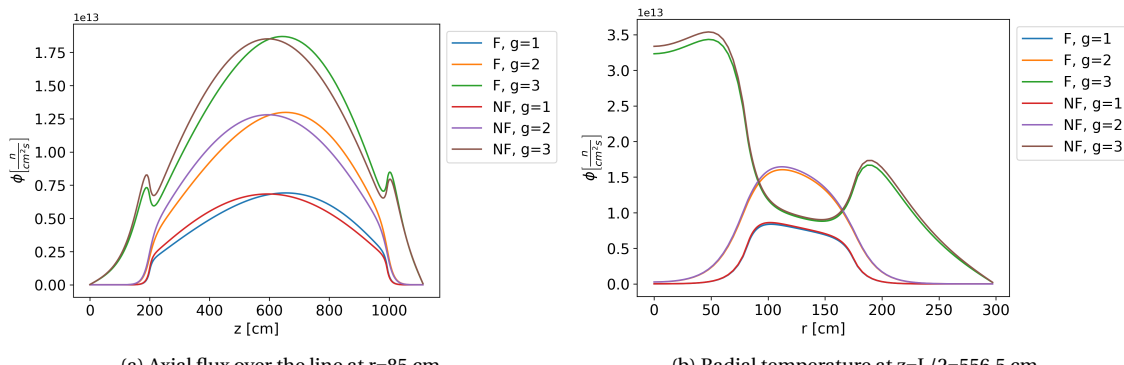
Figure 5.13: Axial view of the model geometry.

Table 5.14: Homogenization scheme.

Model homogenized region	Benchmark sub-domains
Fuel	1-220
Bottom reflector	221-224
Top reflector	228-231
Inner reflector	225
Outer reflector	226-227

Table 5.15: Energy group condensation scheme.

Model group number	Benchmark group number
1	1-4
2	5-15
3	16-26



(a) Axial flux over the line at  $r=85$  cm.

(b) Radial temperature at  $z=L/2=556.5$  cm

Figure 5.14: Flux profile comparison. F: thermal feedback, NF: no thermal feedback.

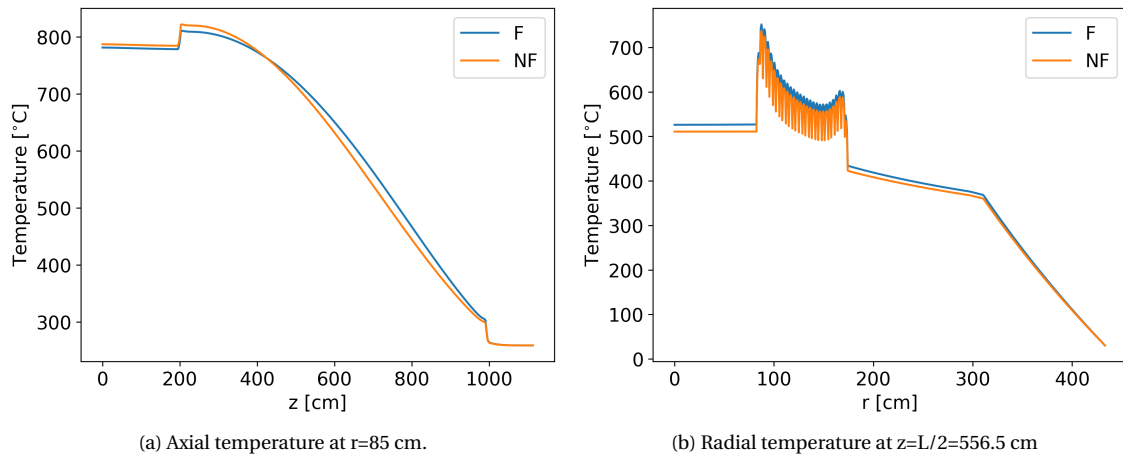


Figure 5.15: Temperature profile comparison. F: thermal feedback, NF: no thermal feedback.

temperature on each node, and each node uses its temperature to compute the thermal feedback on the neutron flux.

As discussed in Chapter 4, in a prismatic HTGR simulation, the neutronics calculation requires an assembly-level homogenization of the group constants. Because of the homogenization, a mesh node holds the group constants' combined information from the different materials in the assembly — only the fuel and the moderator as the coolant does not contribute considerably. The fuel group constants depended on the fuel temperature, and the moderator group constants depended on the moderator temperature, the thermal feedback depends on both temperatures. Hence, a mesh node should hold both temperatures.

Section 5.4.1 used a heterogeneous thermal-fluid model to solve the temperature in the reactor. The problem with using a heterogeneous model is that each node only holds the temperature's value in that particular material. A coolant node holds the coolant temperature information and computes the thermal feedback with such information instead of the moderator and fuel temperature. For this reason, Moltres should use the average assembly-level fuel and moderator temperatures instead of the point-wise temperature to compute the thermal feedback.

The thermal-fluids model in Section 5.4.1 homogenized the fuel and the moderator into one material. Such homogenization assumes that both the moderator and fuel are in thermal equilibrium, and therefore have the same temperature. Consequently, the model does not differentiate the fuel temperature from the moderator temperature. However, a coupling model cannot correctly calculate the thermal feedback if it does not differentiate between the moderator and the fuel temperatures [53].

I denote this issue as the 'homogenization dilemma.' To correctly compute neutronics, the diffusion solver must use homogenized parameters that depend on both moderator and fuel temperatures. Simultaneously, to accurately calculate the thermal feedback, a mesh node should differentiate the moderator temperature from the

fuel temperature, which requires a heterogeneous calculation in the thermal-fluids model. A thermal-fluid heterogeneous calculation is still valid, but the thermal feedback should use fuel and moderator average temperatures instead.

### 5.4.3 Coupled exercise with average temperature thermal feedback

The previous discussion led to the development of this section. This section conducted Section 5.4.1 analysis calculating the thermal feedback with the solid average temperatures. Section 5.4.1 calculated the thermal feedback using the point-wise temperatures. This section compares the results from both approaches.

Figure 5.16 exhibits the point-wise temperature and the average temperatures across the reactor. The model used the average temperatures to compute the thermal feedback in the core. The simulations did not compute the average temperature in the RPV and the outside air. Figure 5.17 displays the neutron flux profiles, and Figure 5.18, the temperature profiles. The results are almost identical. The only noticeable difference is in the axial temperature profile, which differs by less than 3°C in the outlet. The radial temperature profile is not affected.

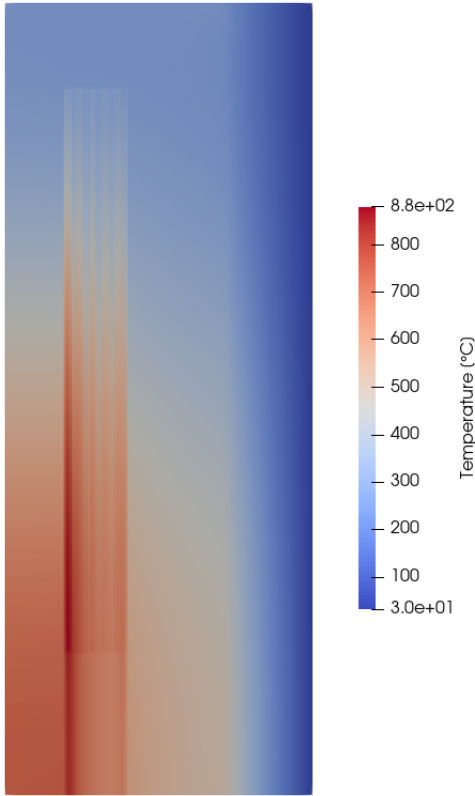
This analysis expected more variations in the results. The point-wise approach arrived at similar results because the difference between the solid and coolant temperature is small (less than 100°C). However, in transient analyses, the temperature difference between the fuel and the coolant may increase, causing more variability in the results. Further studies should analyze this behavior.

## 5.5 Conclusions

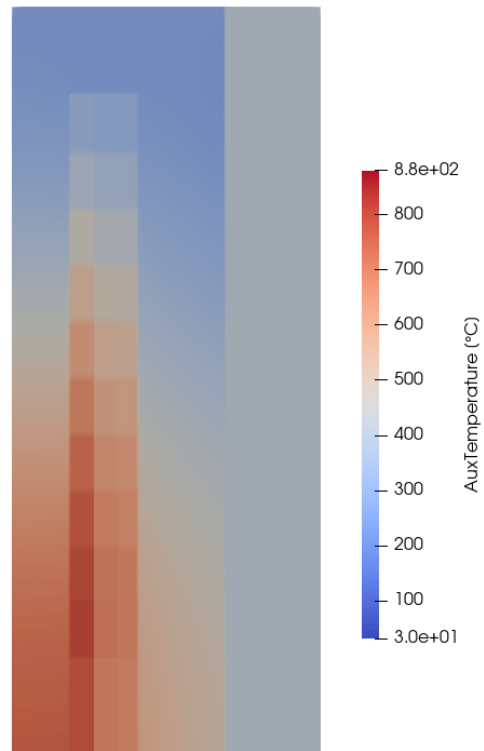
This chapter addressed several objectives of this thesis by presenting the results of several stand-alone thermal-fluids simulations of prismatic HTGRs using Moltres.

The preliminary studies focused on the verification of the thermal-fluids model and the validation of the unit-cell model. The verification of the thermal-fluids model studied a simplified cylindrical model comparing the Moltres/MOOSE numerical solution to the problem analytical solution - both solutions were in agreement. To validate the unit cell model, Section 5.1.2 compared Moltres/MOOSE results to the results from a published article. Moltres/MOOSE results presented some discrepancies, being within 2% of the reference results.

Section 5.2 focus of the analysis was a 1/12<sup>th</sup> section of an HTGR fuel column. To validate the model, Section 5.2 analysis reproduced a published article's results. The analyses comprised two studies: one with no bypass-gap, and one with a 3mm-bypass-gap. To simplify the analysis, the model adopted the mass flow rates from Sato's article. For both case studies, the coolant and the fuel's maximum temperatures were within a 1% difference to the reference temperatures. Section 5.2 also presented the temperature profile in two of the edges of the geometry, exhibiting the

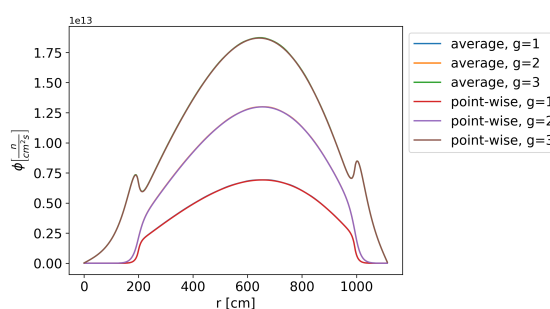


(a) Temperature profile.

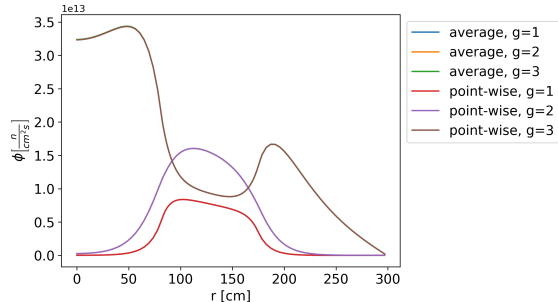


(b) Average temperature in each assembly.

Figure 5.16: Temperature distribution.



(a) Axial flux over the line at  $r=85$  cm.



(b) Radial temperature at  $z=L/2=556.5$  cm

Figure 5.17: Flux profile comparison.

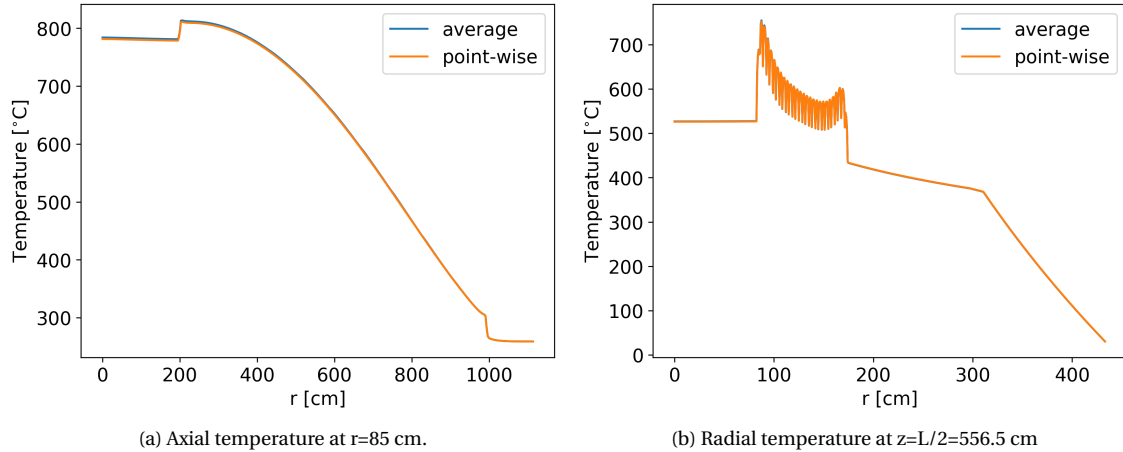


Figure 5.18: Temperature profile comparison.

effects of the bypass flow on the temperature distribution. The bypass-gap makes the center temperature rise while reducing the peripheral temperature, overall, increasing the temperature gradient inside the column.

The next analysis studied different calculation methods for the mass flow distribution in the fuel column. Section 5.2.1 adopted known mass flow distribution values as a reference and calculated the mass flow distribution using four different methods. From Cases 1 to 4, the methods' complexity increased as some required iterative solvers. Overall, Case 1 proved to be the simplest method, and its application did not considerably deteriorate the results' accuracy. For that reason, the following studies adopted the Case 1 mass flow distribution method.

Section 5.2.2 studied the feasibility of extending this methodology to larger meshes and conduct full-scale simulations. Section 5.2.2 studied the mesh convergence of the full-fuel column problem. As the model uses the one-dimensional coolant equations, the coolant temperature converges relatively fast compared to the fuel temperature. The fuel temperature did not reach convergence in this analysis. As the mesh discretization increased, it imposed a high memory requirement on the simulations. This analysis concluded that modeling thermal-fluids with such a detailed level is computationally too expensive, and it suggests searching for other approaches. The following sections adopted a two-dimensional cylindrical model for the full-core analyses.

Section 5.3 described Phase I Exercise 2 of the OECD/NEA MHTGR-350 Benchmark. This exercise encompasses four sub-cases with different definitions of bypass-flow and material properties. The simplest sub-case is Exercise 2a, as it does not model the bypass flow and defines the material properties. Section 5.3 used Moltres/MOOSE to conduct Exercise 2a. As OECD/NEA did not publish this exercise's results, Section 5.3 compared Moltres/MOOSE results to INL benchmark results [57]. Moltres' thermal-fluids model based its definition on INL's model. The large discrepancies between Moltres/MOOSE and INL results suggest that our model does not capture some heat transfer mechanism that the INL model does. One of the known differences between the models is the inclusion of

the radiative heat transfer mechanism. As Moltres does not model that mechanism, it could be the cause of the discrepancies.

A second study in Section 5.3 used a two-level approach, based on a global and a unit cell model [93]. The global model calculated the coolant temperature, while the unit cell model focused on the moderator and fuel temperatures. With this approach, Moltres/MOOSE results were closer to INL results. The results showed some discrepancies, which indicates that some assumption/model simplification is not accurate enough. A flat velocity approximation might be the cause of such discrepancies. Further studies should analyze their origin.

Section 5.4.1 developed a global model to solve a simplified version of Phase 1 Exercise 3 of the OECD/NEA benchmark. Although the model was simple, it allowed visualizing some of the essential aspects of a prismatic HTGR multi-physics simulation in Moltres. This exercise led to Section 5.4.2, which described some of the flaws found in the model. Additionally, Section 5.4.3 addressed some of the flaws found in the model and set the basis for conducting prismatic HTGR coupled exercises in Moltres.

This chapter met the objective to predict the prismatic HTGRs temperature profile accurately; however, it achieved it partially. This work proved Moltres' capability to conduct steady-state thermal-fluid calculations in local models such as the unit cell and the fuel column problems. On the other hand, the full-core results showed several discrepancies that will require further analysis. This chapter arrives at a similar conclusion for the objective of conducting coupled simulation. Nevertheless, an inaccurate thermal-fluids calculation yields inaccurate coupled simulations. For this reason, Section 5.4.1 carried out a simplified exercise with the objective of establishing the roadmap for future simulations.

# Chapter 6

## Hydrogen Production

Two characteristics of HTGRs, high-temperature and high thermal conversion efficiency, motivated the development of this chapter. Those two characteristics enable highly-efficient hydrogen production. This chapter analyzes several hydrogen production processes coupled to various nuclear reactor designs. To find the most efficient strategy, the analysis not only considers HTGRs but also other types of reactors. This chapter comprehends the following sections: Section 6.1 discusses several energy challenges and introduces an alternative based on nuclear reactors and a hydrogen economy, Section 6.2 summarizes the specific objectives of this chapter, Section 6.3 outlines various hydrogen production methods and their energy requirements, Section 6.4 describes the characteristics of microreactors and Small Modular Reactors (SMRs), Section 6.5 presents the methodology followed in the calculations, Section 6.6 displays the results of the different analyses, and Section 6.7 concludes the chapter with a summary and the main points of the chapter.

### 6.1 Introduction

Energy is one of the most vital contributors to economic growth. In the future, economies and populations will continue to expand, and their energy demand will accompany such change [114] [115]. Meeting these future needs requires the development of clean energy sources to ease the increasing environmental concerns. As seen in Figure 6.1, electricity generation was one of the economic sectors that released the most greenhouse gases (GHGs) in the US in 2017. As carbon dioxide ( $\text{CO}_2$ ) is the main component in GHGs, decarbonizing electricity generation will allow us to meet the increases in energy demand and address the environmental concerns simultaneously.

To address these concerns, utility companies rely more and more on renewable energy resources, such as wind and solar [117]. However, high solar adoption creates a challenge. The need for electricity generators to ramp up quickly increases when the sun sets and the contribution from the photovoltaics falls [118]. The "duck curve" (or duck chart) in Figure 6.2 depicts this phenomenon. The California ISO (CAISO) developed the duck curve to illustrate the grid's net load [119]. This thesis defines the net load as the difference between the forecasted load and expected electricity production from solar.

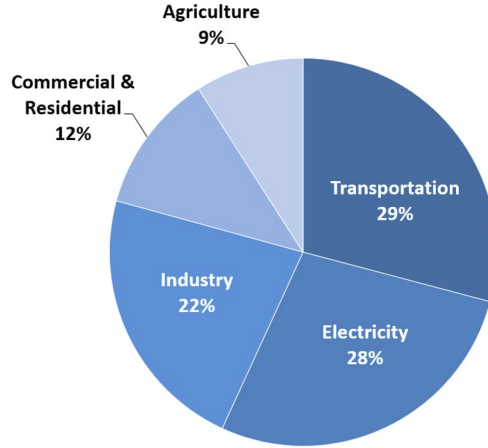


Figure 6.1: Total US GHG emissions by economic sector in 2017. Image reproduced from [116].

Moreover, the duck curve reveals another issue. Over-generation may occur during the middle of the day, and high-levels of non-dispatchable generation may exacerbate the situation. Consequently, the market would experience sustained zero or negative prices during the middle of the operating day [119].

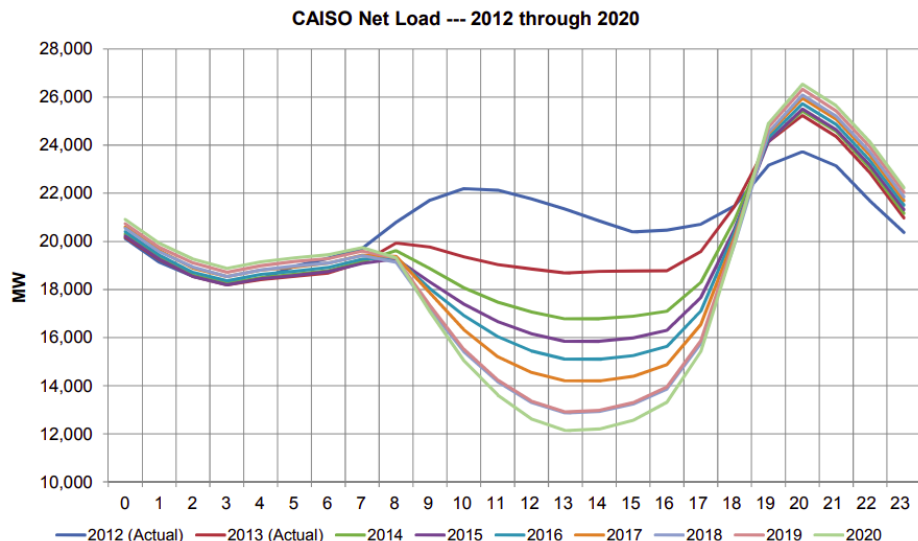


Figure 6.2: The duck curve. Image reproduced from [119].

The simplest solution to a demand ramp-up is to increase dispatchable generation, which uses resources with fast ramping and fast starting capabilities such as natural gas and coal [119], consequently decreasing non-dispatchable generation, such as geothermal, nuclear, and hydro. Nonetheless, an approach like this is inconsistent with the goal of reducing carbon emissions. Hence, our focus drifts to other potential low-carbon solutions, like nuclear generation and electricity storage through H<sub>2</sub> production.

Unfortunately, a carbon-neutral electric grid will be insufficient to halt climate change because transportation

is a significant contributor to GHG emissions. As seen in Figure 6.1, transportation released the most GHGs in the US in 2017. Thus, decarbonizing transportation underpins global carbon reduction. One possible strategy is to develop a hydrogen economy, as Japan is currently doing. Japan's strategy rests on the firm belief that H<sub>2</sub> can be a decisive response to its energy and climate challenges. It could foster deep decarbonization of the transport, power, industry, and residential sectors while strengthening energy security [14]. In the transportation sector, Japan plans to deploy fuel cell vehicles, trucks, buses, trains, and ships. Although H<sub>2</sub> technologies release zero CO<sub>2</sub>, any H<sub>2</sub> production method is only as carbon-free as the energy source it relies on (electric, heat, or both). Nuclear reactors introduce a clean energy option to manufacture H<sub>2</sub>.

UIUC is leading by example and actively working to reduce GHG emissions from electricity generation and transportation (among other sectors) on its campus. In pursuance of those efforts, the university developed the Illinois Climate Action Plan (iCAP).

### 6.1.1 Illinois Climate Action Plan

In 2008, UIUC signed the American College and University Presidents' Climate Commitment, formally committing to becoming carbon neutral as soon as possible, no later than 2050. The university developed the iCAP in 2010 as a comprehensive roadmap toward a sustainable campus environment [120]. The iCAP defines a list of goals, objectives, and potential strategies for six topical areas.

- Energy Conservation and Building Standards:

Focuses on maintaining or reducing campus gross square footage, strengthening conservation efforts, and engaging the campus community in energy conservation.

- Energy Generation, Purchasing, and Distribution:

Explores 100% clean campus energy options. This includes expanding on-campus solar energy production, extending the purchase of clean energy from low-carbon energy sources, and offsetting all emissions from the National Petascale Computing Facility.

- Transportation:

Comprises the efforts to reduce air travel emissions, reduce Urbana-Champaign campus fleet emissions, and study scenarios for the complete conversion of the campus fleet to renewable fuels.

- Water and Stormwater:

Focuses on improving the water efficiency of cooling towers, performing a water audit to establish water conservation targets, determining upper limits for water demand by end-use, and implementing projects to showcase the potential of water and stormwater reuse.

- Purchasing, Waste, and Recycling:

Attempts to standardize purchasing office paper, cleaning products, computers, and other electronics as well as freight delivery services. It also attempts to facilitate recycling by reducing non-durable goods purchases and reducing municipal solid waste going to landfills.

- Agriculture, Land Use, Food, and Sequestration:

Will perform a comprehensive assessment of GHG emissions from agricultural operations, develop a plan to reduce these emissions, implement a project that examines the foodservice carbon footprint for Dining, and increase carbon sequestration in campus soils.

## 6.2 Objectives

This chapter focuses on two areas: transportation and electricity generation on the UIUC campus. Consequently, this work's objective aligns with the efforts in two of the six target areas defined on the iCAP.

Regarding transportation, the objective is to quantify UIUC fleet fuel consumption, determine how much H<sub>2</sub> enables the fleet conversion to Fuel Cell Electric Vehicles (FCEVs), and find reactor designs that meet the H<sub>2</sub> demand.

Regarding electricity generation, the objective is to quantify the magnitude of the duck curve in the UIUC's grid, determine how much H<sub>2</sub> a reactor coupled to a H<sub>2</sub> production process could produce, and how much electricity that H<sub>2</sub> would generate if converted.

## 6.3 Hydrogen production methods

This section introduces several hydrogen production processes and their energy requirements.

### 6.3.1 Electrolysis

The electrolysis of water is a well-known process whose commercial use began in 1890. This process produces approximately 4% of H<sub>2</sub> worldwide. The process is ecologically clean because it does not emit GHGs. However, in comparison with other methods, electrolysis is a highly energy-demanding technology [121].

Three electrolysis technologies exist. Alkaline-based is the most common, the most developed, and the lowest in capital cost. It has the lowest efficiency and, therefore, the highest electrical energy cost. Proton exchange membrane electrolyzers are more efficient but more expensive than Alkaline electrolyzers. Solid Oxide Electrolysis Cells (SOEC) electrolyzers are the most electrically efficient but the least developed. SOEC technology has challenges with corrosion, seals, thermal cycling, and chrome migration [121]. The first two technologies work with liquid water, and the latter requires high-temperature steam, so this work refers to the first two as Low-Temperature Electrolysis (LTE) and the latter as High-Temperature Electrolysis (HTE).

Water electrolysis converts electric and thermal energy into chemical energy stored in hydrogen. The process enthalpy change  $\Delta H$  determines the required energy for the electrolysis reaction to take place, in which part of the energy corresponds to electric energy  $\Delta G$  and to thermal energy  $T \cdot \Delta S$

$$\Delta H = \Delta G + T\Delta S \quad (6.1)$$

where

$$\Delta H = \text{specific total energy } [kWh \cdot kg_{H_2}^{-1}]$$

$$\Delta G = \text{specific electrical energy } [kWh \cdot kg_{H_2}^{-1}]$$

$$T\Delta S = \text{specific thermal energy } [kWh \cdot kg_{H_2}^{-1}].$$

In LTE, electricity generates the thermal energy. Hence,  $\Delta H$  alone determines the process's required energy.  $\Delta H$  is equal to 60 kWh/kg-H<sub>2</sub> considering a 67% electrical efficiency [122].

In HTE, a high-temperature heat source is necessary to provide the thermal energy.  $\Delta G$  decreases with increasing temperatures, as seen in Figure 6.3. Decreasing the electricity requirement results in higher overall production efficiencies since heat-engine-based electrical work has a thermal efficiency of 50% or less [123]. Figure 6.3 shows  $\Delta G$  and  $T\Delta S$ . The analyses considered the SOEC's  $\Delta G$  to have an electrical efficiency of 88% [124].  $T\Delta S$  accounts for the latent heat of water vaporization. Note that the process is at 3.5 MPa. Although  $\Delta G$  increases with pressure, a high pressure saves energy, as compressing liquid water is cheaper than compressing H<sub>2</sub> [125].

Equations 6.2 and 6.3 determine the electrical  $P_{EH2}$  and thermal power  $P_{TH2}$  required by the hydrogen plant

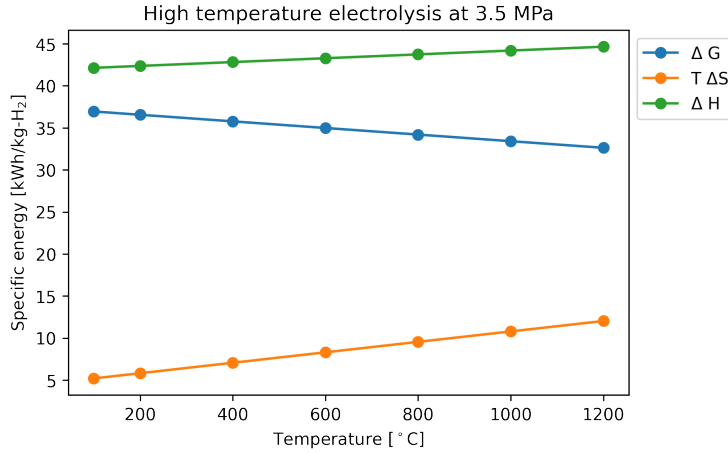


Figure 6.3: Energy required by HTE at 3.5 MPa.

$$P_{EH2} = \dot{m}_{H2} \Delta G \quad (6.2)$$

$$P_{TH2} = \dot{m}_{H2} T \Delta S \quad (6.3)$$

where

$$P_{EH2} = \text{total electrical power [kW]}$$

$$P_{TH2} = \text{total thermal power [kW]}$$

$$\dot{m}_{H2} = \text{H}_2 \text{ production rate [kg} \cdot h^{-1}\text{].}$$

### 6.3.2 Sulfur-Iodine Thermochemical Cycle

A thermochemical water-splitting process converts water into hydrogen and oxygen by a series of thermally driven chemical reactions. The direct thermolysis of water requires temperatures above 2500 °C for significant hydrogen generation. At this temperature, the process can decompose 10% of the water. A thermochemical water-splitting cycle accomplishes the same overall result using much lower temperatures.

General Atomics, Sandia National Laboratories, and the University of Kentucky compared 115 cycles that would use high-temperature heat from an advanced nuclear reactor [126]. The report specified a set of screening criteria used to rate each cycle. Some of the cycles' desirable characteristics were minimal chemical reactions and separation steps, a high abundance of the elements, a minimal solids flow, and good compatibility between heat input temperature and the permitted materials' high temperature. The highest scoring method was the

Sulfur-Iodine (SI) cycle.

The SI cycle consists of the three chemical reactions represented in Figure 6.4. The whole process inputs are water and high-temperature heat, having no need for electricity. The process recycles all reagents and lacks effluents [16]. The chemical reactions are

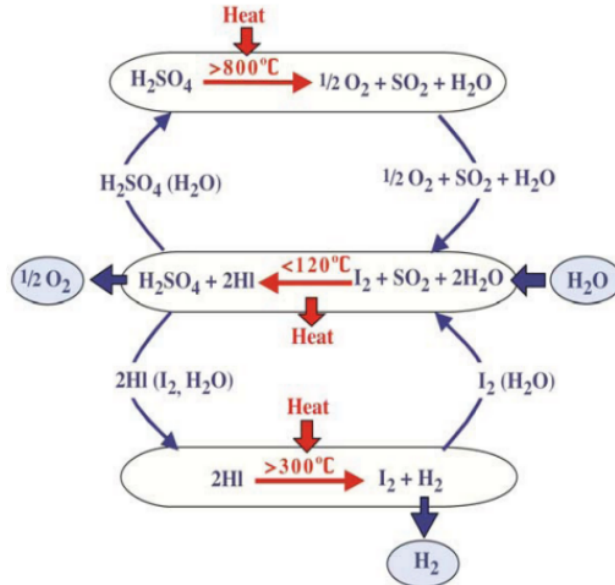


Figure 6.4: Diagram of the Sulfur-Iodine Thermochemical process. Image reproduced from [127].

Figure 6.5 presents the specific energy requirements of the cycle  $\Delta H$ . Several sources disagree on the minimum temperature for the process to be viable. This work considers the process feasible only for temperatures above 800 °C. Finally, equation 6.7 determines the thermal power  $P_{TH2}$  required by the hydrogen plant

$$P_{TH2} = \dot{m}_{H_2} \Delta H \quad (6.7)$$

where

$$P_{TH2} = \text{total thermal power [kW]}$$

$$\dot{m}_{H2} = \text{H}_2 \text{ production rate [kg} \cdot h^{-1}]$$

$$\Delta H = \text{specific energy [kWh} \cdot kg_{H_2}^{-1}\text{].}$$

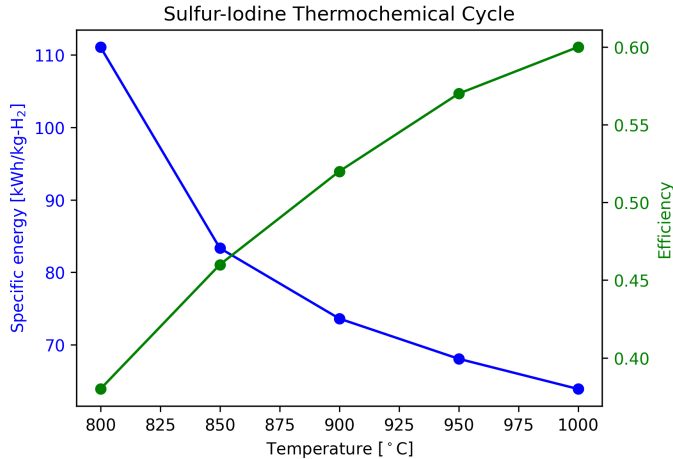


Figure 6.5: Energy required by the Sulfur-Iodine Thermochemical Cycle.

## 6.4 Microreactors and Small Modular Reactors

The typical UIUC's grid demand is smaller than 80 MW [128]. Accordingly, the following analyses consider reactors of small capacities, such as microreactors and SMRs.

These reactor concepts share several features. The reactors require limited on-site preparation as their components are factory-fabricated and shipped out to the generation site. This feature reduces up-front capital costs, enables rapid deployment, and expedites start-up times. These reactors allow for black starts and islanding operation mode. They can start up from an utterly de-energized state without receiving power from the grid. They can also operate connected to the grid or independently. Moreover, these reactors are self-regulating, minimize electrical parts, and use passive safety systems to prevent overheating and safely shutdown.

Microreactors have the distinction that they are transportable. Small designs make it easy for vendors to ship the entire reactor by truck, shipping vessel, or railcar. These features make the technology appealing for a wide range of applications, such as deployment in remote residential locations and military bases.

The DOE defines a microreactor as a reactor that generates from 1 to 20 MWth [129]. The IAEA describes an SMR

as a reactor whose power is under 300 MWe. The IAEA defines, as well, a 'very small modular reactor' as a reactor that produces less than 15 MWe [130]. As the definitions of these reactor concepts overlap, this work considers reactors of less than 100 MWth regardless of their specific classification.

## 6.5 Methodology

In this analysis, the energy source (electric and thermal) is a nuclear reactor with co-generation capabilities. The nuclear reactor supplies the grid with electricity  $P_E$  while providing a hydrogen plant with electricity  $P_{EH2}$  and thermal energy  $P_{TH2}$ , as shown in Figure 6.6.

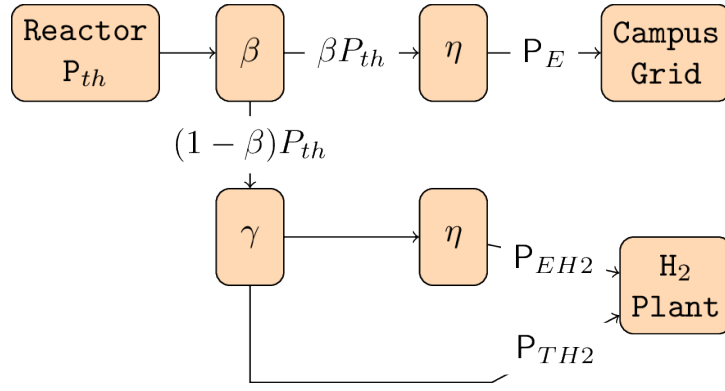


Figure 6.6: Diagram of a reactor coupled to a hydrogen plant.

$\beta$  and  $\gamma$  determine the distribution of the reactor thermal power  $P_{th}$  into  $P_E$ ,  $P_{EH2}$ , and  $P_{TH2}$

$$P_E = \eta\beta P_{th} \quad (6.8)$$

$$P_{EH2} = \eta\gamma(1 - \beta)P_{th} \quad (6.9)$$

$$P_{TH2} = (1 - \gamma)(1 - \beta)P_{th} \quad (6.10)$$

where

$\eta$  = thermal-to-electric conversion efficiency[–]

giving

$$\beta = \frac{P_E/\eta}{P_E/\eta + P_{TH2}/(1-\gamma)} \quad (6.11)$$

$$\gamma = \frac{P_{EH2}/\eta}{P_{EH2}/\eta + P_{TH2}}. \quad (6.12)$$

If  $\beta = 1$ , the reactor only supplies the grid with electricity  $P_E$ , and the hydrogen plant does not produce H<sub>2</sub>. If  $\beta = 0$ , the reactor only supplies the hydrogen plant, and electricity does not flow into the grid. Table 6.1 summarizes the values that  $\gamma$  takes for the various methods.

Table 6.1: Energy requirements of the different H<sub>2</sub> production methods.

Method	$\gamma$	$P_{EH2}$	$P_{TH2}$
LTE	1	$\neq 0$	0
HTE	$0 < \gamma < 1$	$\neq 0$	$\neq 0$
SI	0	0	$\neq 0$

This thesis focuses on two areas: transportation and electricity generation on the UIUC campus. Regarding transportation, Section 6.6.1 discusses the conversion of the UIUC fleet operating on campus to FCEVs. The analysis includes the conversion of the Champaign-Urbana Mass Transit District (MTD) fleet as well. The first step determines the fuel consumed by both fleets and how much H<sub>2</sub> enables the fleets' complete conversion. The next step evaluates several reactor designs and analyzes which ones could produce enough H<sub>2</sub> to fulfill both fleet requirements.

Section 6.6.2 focuses on electricity generation in UIUC's grid. The first step in the analyses quantifies the magnitude of the duck curve in UIUC's grid. To mitigate the consequences of over-generation, in a scenario in which a nuclear reactor is the primary source of energy, I propose to use the over-generated energy to manufacture H<sub>2</sub>. The next step in the analysis quantifies how much H<sub>2</sub> several production methods can generate. The last step in the analysis calculates how much electricity the H<sub>2</sub> could produce.

Both studies propose the same solution - a nuclear reactor coupled to a hydrogen plant. In terms of electricity generation, this solution decreases the need for dispatchable sources and, consequently, reduces carbon emissions. In terms of transportation, it eliminates carbon emissions.

## 6.6 Results

This section holds the results of the transportation sector analysis, Section 6.6.1, and the Energy Generation analysis, Section 6.6.2.

### 6.6.1 Transportation

This section studies the transportation sector fuel requirements. Figure 6.7 displays the fuel consumed per day by MTD and UIUC fleet. The values shown in Table 6.2 allow for calculating the H<sub>2</sub> requirement for MTD and UIUC fleets, shown in Figure 6.8. Table 6.3 summarizes the results.

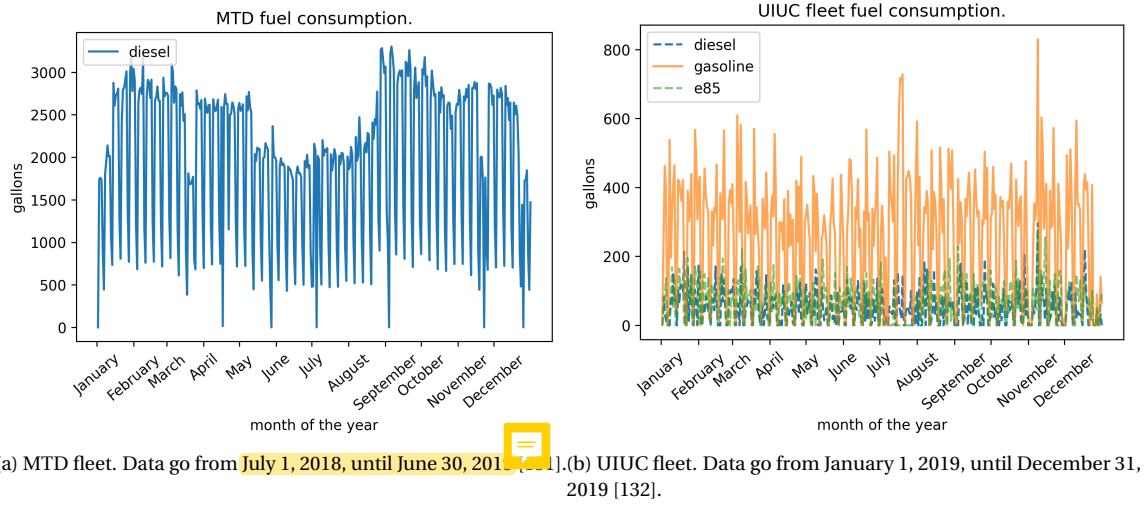


Figure 6.7: Fuel consumption data of MTD and UIUC fleet.

Table 6.2: H<sub>2</sub> necessary to replace a gallon of fuel [133] [134].

Hydrogen Mass [kg]	
Gasoline	1.00
Diesel	1.13
E85	0.78

Table 6.3: H<sub>2</sub> requirement for MTD and UIUC fleets.

Total [tonnes · year <sup>-1</sup> ]	943
Average [kg · day <sup>-1</sup> ]	2584
Average [kg · h <sup>-1</sup> ]	108
Maximum in one day [kg]	4440

Table 6.4 allows for calculating the CO<sub>2</sub> savings caused by converting the fleets to FCEVs. Table 6.5 displays the CO<sub>2</sub> savings for both fleets.

The analysis determined the H<sub>2</sub> requirement by the fleets, and analyses several microreactor designs capable of meeting such demand. Table 6.6 summarizes the microreactor designs considered for this analysis. Further studies could include other designs as well.

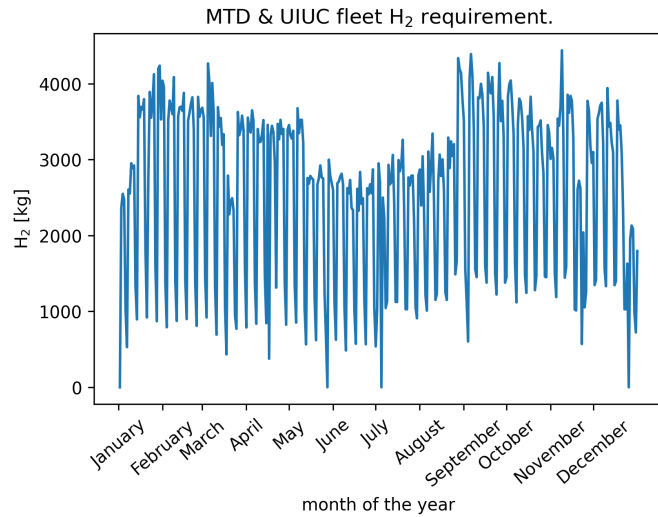


Figure 6.8:  $\text{H}_2$  requirement for MTD and UIUC fleets.

Table 6.4:  $\text{CO}_2$  savings in pounds per gallon of fuel burned [135].

CO <sub>2</sub> produced [lbs · gallon <sup>-1</sup> ]	
Gasoline	19.64
Diesel	22.38
E85	13.76

Table 6.5:  $\text{CO}_2$  yearly savings.

CO <sub>2</sub> mass [tonnes · year <sup>-1</sup> ]	
MTD	7306
UIUC	1143
Total	8449

Figure 6.9 shows the hourly production rates for the different reactors and H<sub>2</sub> production processes. The figure includes a continuous line that represents the hydrogen requirement of both fleets. The microreactors that can meet both fleet hydrogen needs are the MMR, ST-OTTO, U-battery, and Starcore. The Starcore design is the only one that could use the SI process as its outlet temperature is above 800°C.

Table 6.6: Microreactor designs.

Reactor	P[MWth]	T <sub>o</sub> [°C]
MMR [24]	15	640
eVinci [136]	5	650
ST-OTTO [137]	30	750
U-battery [138]	10	750
Starcore [23]	36	850

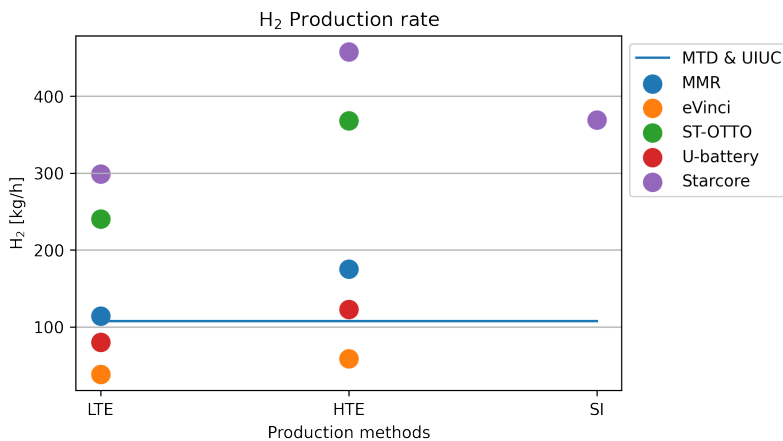


Figure 6.9: Hydrogen production rate by the different microreactor designs.

## 6.6.2 Electricity Generation

This section describes the analysis of the electricity generation sector and the duck curve problem. This work predicted the UIUC grid's load and the expected electricity production from solar to quantify the duck curve's magnitude. As the iCAP's main objective is to become carbon neutral before 2050, this study made a prediction for that year. UIUC's solar farm is relatively new, and more data is necessary to produce a reliable forecast. To circumvent this barrier, the analysis used the available data for the whole US [139]. Figure 6.10 displays the prediction for 2050. The prediction used the linear regression that produces the worst-case scenario, in which the total load increases minimally, whereas the solar generation rises considerably.

The next step applied the same growth factor from the predictions to the UIUC grid's load and solar electricity. The growth factor scaled up the hourly data to obtain a forecast for 2050. I chose a spring day when solar production

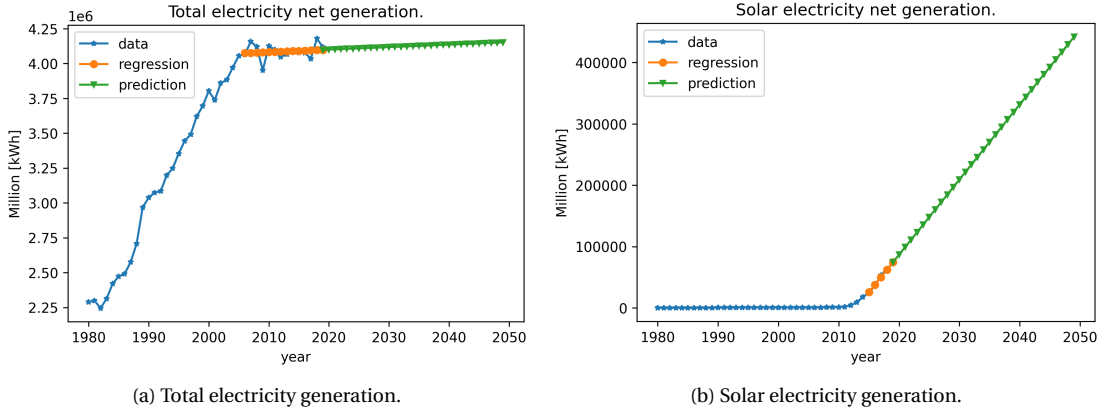


Figure 6.10: Prediction of the electricity generation in the US for 2050. Data from [139].

is higher, as it is sunny, but the total load is low since people are less likely to use electricity for air conditioning or heating [118]. Finally, subtracting the solar production from the total load yielded the net load or demand ( $D_{NET}$ ), shown in Figure 6.11. The net demand reached the lowest value in the 2019's spring on April 4th. In 2050, the peak net demand will be 46.9 MWh at 5 PM, while the lowest net demand will be 15 MWh at 11 AM. The consequent demand ramp is of 31.9 MWh in 4 hours. These results show that the grid requires an available capacity of dispatchable sources of at least 31.9 MW to meet demand ramps.

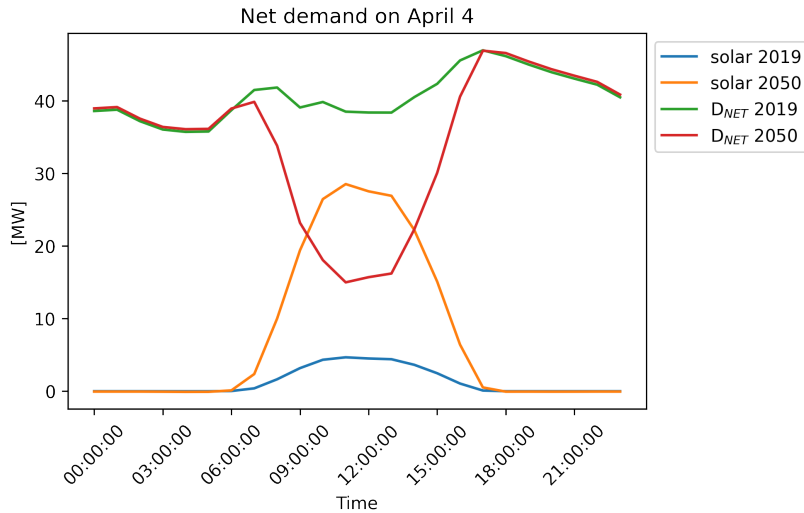


Figure 6.11: Prediction of the UIUC's net demand for 2050.

The next step calculated the over-generated electricity. For that purpose, I rarely chose a reactor of 25 MWe. For the LTE case, any reactor was a valid option. The choice of an  $\eta$  of 33% yields a reactor power of 75.8 MWth. For the HTE case, the reactor's choice was an HTGR with an outlet temperature of 850°C. Considering an  $\eta$  of 49.8% yields a reactor of 50.2 MWth.

The reactor operates at full capacity at all times. However, the reactor electricity production ( $P_E$ ) equals the net demand ( $D_{NET}$ ) once smaller than 25 MWe

$$P_E = D_{NET}$$

$$\frac{P_E}{25[\text{MWe}]} = \frac{\eta\beta P_{th}}{\eta P_{th}} = \beta \quad (6.13)$$

Note that  $P_E$  has power units while  $D_{NET}$  has energy units. The choice of 1 hour time steps in our analysis makes  $P_E$  and  $D_{NET}$  differ by the constant  $h$ . As  $P_E$  is lower than 25 MWe, and the reactor is at full thermal capacity, the hydrogen plant takes the excess of thermal energy. Solving equation 6.13 with equations 6.11 and 6.12 in combination with each method's respective equations, allow for calculating each method's production rate. Figure 6.12 displays the results. The total H<sub>2</sub> production reaches 660, 1009, and 815 kg for LTE, HTE, and SI.

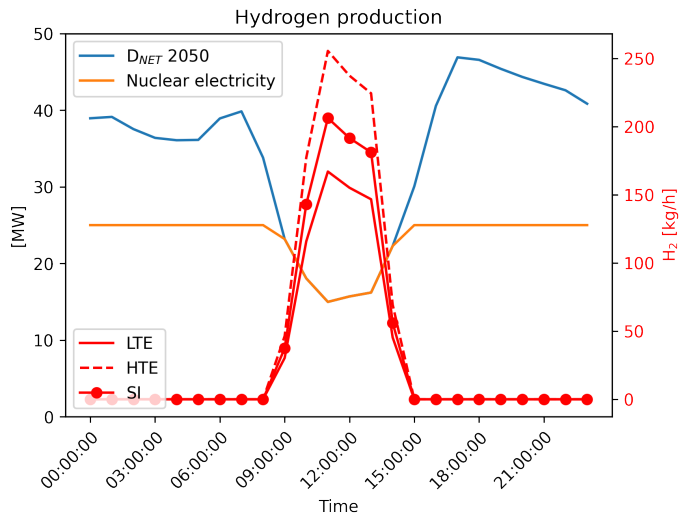


Figure 6.12: H<sub>2</sub> production.

The analysis's last step was to calculate the peak demand reduction by using hydrogen to produce electricity. The energy produced by hydrogen is 285 kJ/mol, equal to 40 kWh/kg [140]. However, conventional fuel cells can use up to 60% of that energy [141]. Knowing the mass of hydrogen produced, I calculated the total electricity produced. The distribution of the electricity over a specific range of hours reduces the peak demand. I chose to distribute the electricity for over 6 hours. The following equation allowed for calculating the new peak

$$NP = \frac{\sum_{i=0}^N D_{NET,i} - TH}{N} \quad (6.14)$$

where

$$NP = \text{new peak magnitude}[kW]$$

$$D_{NET,i} = \text{hourly net demand } [kWh]$$

$$TH = \text{total mass of hydrogen } [kg]$$

$$N = \text{total number of hours}[-].$$

Figure 6.13 shows these results. The different H<sub>2</sub> processes can generate 15.84 MWh, 24.2 MWh, and 19.6 MWh, respectively. This generation accounts for a peak reduction of 5 MW, 6.4 MW, and 5.6 MW.

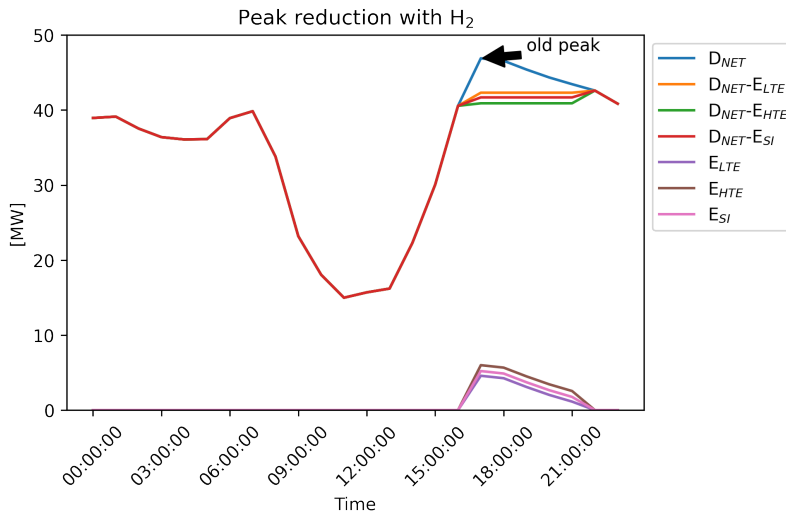


Figure 6.13: Peak reduction by using the H<sub>2</sub> produced by the different production methods.  $E_{LTE}$ ,  $E_{HTE}$ , and  $E_{SI}$  are the generated electricity from the different method's hydrogen production.

## 6.7 Conclusions

The world faces energy challenges that compromise the efforts to stop climate change. The electricity generation and transportation sectors contribute the most to GHG emissions and are the major contributors to climate change. These challenges underscore the need for cleaner sources. Nonetheless, the common belief that renewable energy is the solution to the problem presents several drawbacks. The duck curve is an example of such disadvantages. Moreover, a carbon-neutral electric grid will be insufficient to halt climate change. The transportation sector needs to survey some possible alternatives to become carbon-free as well. This work analyzed combining nuclear energy and hydrogen production as a possible solution to these energy challenges.

To seek a solution for the challenge described above, the analyses studied a specific case, UIUC's campus. Through the implementation of the iCAP, the University of Illinois is actively working to reduce GHG emissions on its campus. This work's objective aligns with the efforts in two of the six target areas defined on the iCAP: electricity generation and transportation.

Regarding hydrogen production methods, this work surveyed three different processes: LTE, HTE, and SI. I developed a tool to calculate their energy requirements regarding electricity and heat and hydrogen production rates. This tool is applicable to a stand-alone hydrogen plant and a nuclear power plant that produces both electricity and hydrogen.

In the transportation sector analysis, Section 6.6.1 analysis quantified the fuel requirements of MTD and UIUC fleets, calculated the mass of hydrogen necessary to replace 100% of the fleet's fossil fuel usage, and calculated the hydrogen production rates of several microreactor designs.

The electricity generation analysis predicted the duck curves' magnitude in UIUC's grid in 2050. This result exhibits how an increased solar penetration into the grid worsens the duck curve. This thesis proposed a mitigation strategy that used a microreactor of 25 MWe. Another analysis quantified the mass of hydrogen produced by the different methods during the day when over-generation occurs. Finally, I calculated a peak demand reduction by using the hydrogen produced. This last result highlights that hydrogen introduces a means to store energy that reduces the reliance on dispatchable sources. This analysis emphasizes how nuclear energy and hydrogen production can potentially mitigate climate change.

# Chapter 7

## Conclusions

### 7.1 Contribution

HTGRs have several desirable features that make them ideal candidates for large-scale deployment in the near future, including their reliance on passive heat transfer mechanisms and use of TRISO particles. Additionally, higher temperatures offer increased thermal cycle efficiencies and enable a wide range of process heat applications, such as hydrogen production. Implementing hydrogen economies can be a decisive response to energy and climate challenges by decarbonizing the transport and power sectors.

To support the evolution of the HTGR technology, this work focused on modeling prismatic HTGRs. Modeling the multi-physics of prismatic HTGRs enables predicting the reactor thermal-fluid behavior, which is necessary for assessing HTGR's safety characteristics. HTGRs' complex geometry requires numerical tools to conduct the analyses, such as Moltres — a simulation tool suitable for multi-physics problems. Although its original development targeted MSRs, this work studied Moltres' applicability to prismatic HTGRs.

Multi-physics simulators need to resolve the double heterogeneities present in the prismatic HTGR fuel assemblies. Moltres relies on transport solvers for obtaining group constants. Monte Carlo solvers are capable of explicitly modeling TRISO particles. Although using such a capability is computationally expensive, Chapter 4 proved it necessary for obtaining group constants for diffusion solvers. Additionally, Chapter 4 introduced a discussion on different levels of homogenization that diffusion solvers rely on. Previous work using Moltres focused on MSRs, which allow for heterogeneous calculations. Still, HTGRs require a higher homogenization level than MSRs, making Moltres application to HTGRs not straightforward. This work used Moltres as a homogeneous solver for carrying out neutronics stand-alone simulations of prismatic HTGRs. The first study analyzed the energy group structure effects on a fuel column's simulation, comparing Moltres and Serpent results. Based on those results, the following section conducted a full-core simulation in Moltres using a 15-energy group structure. The comparison between Moltres and Serpent showed good agreement overall, demonstrating Moltres' ability to model stand-alone prismatic HTGR neutronics.

Finally, Moltres carried out Phase I Exercise 1 of the OECD/NEA MHTGR-350 Benchmark. The exercise specifies

the necessary group constants, which required the development of a Python script to adapt them to Moltres format. The exercise models  $1/3^{rd}$  of the MHTGR-350 and uses periodic boundary conditions on the sides. Imposing those boundary conditions in Moltres was not possible because of the high memory requirement of the simulation. Moltres conducted the exercise using reflective boundary conditions to reduce the high memory requirement. Chapter 4 also analyzed the effects of such an approximation, as some discrepancies in the results arose. Section 4.3 concluded that the boundary condition approximation was responsible for causing such discrepancies.

Since Moltres original development targeted MSR simulations, its thermal-fluids kernels' are not readily applicable to prismatic HTGRs. Chapter 5 focused on developing a thermal-fluids model for Moltres. A first preliminary study verified the proposed model by comparing the numerical solution to a known analytical solution. A second preliminary study applied the thermal-fluids model to a unit cell problem and compared Moltres results to a published article's results. Both preliminary studies showed good results. Another study demonstrated the use of Moltres on a larger-scale problem, a fuel column. The study compared Moltres results to a published article's results for two cases: a no-bypass-gap case and a 3mm-bypass-gap case. In both cases, Moltres exhibited good agreement with the published article's results. As part of the fuel column study, two analyses focused on different aspects of the simulations. The first analysis studied the coolant's mass flow distribution modeling, while the second analysis studied the mesh convergence of the full-fuel column problem. This second analysis exposed that a high level of detail in the model imposes a high memory requirement on the simulations, which might restrict the model's applicability to a full-core problem. Section 5.3 assessed a different approach for modeling the thermal-fluids of the MHTGR-350 to circumvent the high memory requirement restriction. This study analyzed Phase I Exercise 2 of OECD/NEA MHTGR-350 Benchmark results calculated by Moltres. The exercise revealed that both a more accurate mass flow distribution and considering the radiative heat transfer mechanism are necessary for the correct modeling of prismatic HTGRs. This work proved Moltres' capability to conduct steady-state thermal-fluid calculations in local models such as the unit cell and the fuel column problems. On the other hand, the full-core results showed several discrepancies that will require further analysis.

Chapter 5 also focused on studying Moltres applicability to prismatic HTGR multi-physics simulations. Section 5.4.1 used a simplified model to solve Phase I Exercise 3 of OECD/NEA MHTGR-350 Benchmark. Although the model was simple, it allowed visualizing some of the essential aspects of prismatic HTGR multi-physics simulations. Conducting this exercise helped to identify Moltres' flaws and sets a basis for future work.

This work aligns with UIUC's goals to reduce CO<sub>2</sub> emissions from the electricity and transportation sectors. Worldwide climate change demands a large-scale deployment of CO<sub>2</sub>-free energy sources. UIUC is fighting climate change by actively reducing GHG emissions on its campus. This work proposed an alternative — the deployment of a nuclear reactor and a hydrogen production plant. Regarding hydrogen production methods, this work surveyed

three different processes: LTE, HTE, and SI. The development of a tool was necessary to calculate the energy requirements and hydrogen production rates of each. This tool is applicable to a stand-alone hydrogen plant and a nuclear power plant that produces electricity and hydrogen. Additionally, Chapter 6 characterized MTD and UIUC fleet fuel consumption and calculated the hydrogen needs from both fleets. Section 6.6.1 identified several microreactor designs that could meet those hydrogen requirements. Finally, Chapter 6 simulated a scenario where solar production on campus exceeds campus demand and diverts the energy surplus to hydrogen production. The produced hydrogen has the potential to reduce campus reliance on fossil fuels during the evening peak demand.

## 7.2 Future Work

This section introduces some possible future work that sets a basis for a Ph.D. as a continuation of this MS thesis. As mentioned in Chapter 4, periodic boundary conditions impose a high memory requirement on Moltres simulations. Since Moltres relies on PetSc routines for solving the equation systems, future work will look for a PetSc routine to enable the exact modeling of Phase I Exercise 1 of the benchmark, i.e., conduct the simulations with the periodic boundary conditions.

The correct modeling of Phase I Exercise 2 of the benchmark ensures the correct modeling of the coupled exercises. Moltres results for Exercise 2a showed some discrepancies to INL benchmark results. As discussed earlier, the flat flow approximation may be the cause. Thus, future work will add a mass flow distribution capability to Moltres. The first analysis of Section 5.3 intended to reproduce INL results, but that analysis revealed that Moltres modeling fails to capture the right heat transfer between different assemblies. Not modeling the radiative heat transfer between elements might be causing this behavior. Future analyses will add the radiative heat transfer modeling capability to Moltres.

Section 5.4.1 set the basis for prismatic HTGR multi-physics simulations in Moltres. In doing so, it revealed that interfacing the neutronics and the thermal-fluids is crucial in multi-physics modeling. Future work will enable the use of the moderator and fuel assembly-level average temperatures to model the thermal feedback properly.

As described in Chapter 6, high temperatures enable efficient hydrogen production. However, LWRs integrate the current fleet of nuclear reactors with outlet temperatures around only 300°C.

HTE and SI are viable processes for temperatures well above 300°C, but the development of hydrogen economies increasingly demands more mature technologies. Related future work will study the CO<sub>2</sub> savings using the steam reforming method, which may use carbon-capture sequestration systems. Future work will also analyze the feasibility of using a carbon-capture sequestration system from an economic perspective.

If the process does not use a carbon-capture sequestration system, the analysis will compare the CO<sub>2</sub> savings

(from using the H<sub>2</sub> instead of fossil fuel) versus the CO<sub>2</sub> production instead (from producing the H<sub>2</sub> with the steam reforming method). Moreover, related future work will study the viability of coupling LWRs to HTE and SI processes via steam temperature boosting systems. These systems rely on electric heaters to enhance the steam temperature, enabling the coupling of hydrogen plants to the LWR fleet. Though not comprehensive, it is a promising short-term mitigation strategy for climate change.

# Appendix A

This appendix describes the most important equations used in this thesis.

## 8.1 Neutron flux equations

Equations 8.1 and 8.2 describe the time dependent behavior of the neutron flux and the concentration of the delayed neutron precursors duded

$$\frac{1}{v_g} \frac{\partial}{\partial t} \phi_g = \nabla \cdot D_g \nabla \phi_g - \Sigma_g^r \phi_g + \sum_{g' \neq g'}^G \Sigma_{g' \rightarrow g}^s \phi_{g'} + \chi_g^p \sum_{g'=1}^G (1-\beta) v \Sigma_{g'}^f \phi_{g'} + \chi_g^d \sum_i^I \lambda_i C_i \quad (8.1)$$

$$\frac{\partial}{\partial t} C_i = \sum_{g'=1}^G \beta_i v \Sigma_{g'}^f \phi_{g'} - \lambda_i C_i \quad (8.2)$$

where

- $v_g$  = group  $g$  neutron speed [ $cm \cdot s^{-1}$ ]
- $\phi_g$  = group  $g$  neutron flux [ $n \cdot cm^{-2} \cdot s^{-1}$ ]
- $t$  = time [s]
- $D_g$  = group  $g$  diffusion coefficient [ $cm$ ]
- $\Sigma_g^r$  = group  $g$  macroscopic removal cross-section [ $cm^{-1}$ ]
- $\Sigma_{g' \rightarrow g}^s$  = group  $g'$  to group  $g$  macroscopic scattering cross-section [ $cm^{-1}$ ]
- $\chi_g^p$  = group  $g$  prompt fission spectrum [-]
- $G$  = number of discrete energy groups [-]
- $v$  = number of neutrons produced per fission [-]
- $\Sigma_g^f$  = group  $g$  macroscopic fission cross-section [ $cm^{-1}$ ]
- $\chi_g^d$  = group  $g$  delayed fission spectrum [-]
- $I$  = number of delayed neutron precursor groups [-]
- $\beta$  = delayed neutron fraction [-]
- $\lambda_i$  = average decay constant of delayed neutron precursors in precursor group  $i$  [ $s^{-1}$ ]
- $C_i$  = concentration of delayed neutron precursors in precursor group  $i$  [ $cm^{-3}$ ].

The following equation relates  $\chi_g^t$  to  $\chi_g^p$  and  $\chi_g^d$  [142]

$$\chi_g^t = \chi_g^p(1 - \beta) + \chi_g^d \sum_i^I \beta_i \quad (8.3)$$

where

$$\chi_g^t = \text{group } g \text{ total fission spectrum [-].}$$

The combination of the steady-state of equations 8.1, 8.2, 8.3, and replacing  $v\Sigma_g^f$  by  $\frac{v\Sigma_g^f}{k_{eff}}$  yields the eigenvalue equation [64]

$$\nabla \cdot D_g \nabla \phi_g - \Sigma_g^r \phi_g + \sum_{g' \neq g'}^G \Sigma_{g' \rightarrow g}^s \phi_{g'} + \chi_g^t \sum_{g'=1}^G \frac{1}{k_{eff}} v \Sigma_{g'}^f \phi_{g'} = 0 \quad (8.4)$$

where

$k_{eff}$  = multiplication factor [-].

## 8.2 Thermal-fluids equations

The three-dimensional heat conduction equation [3] allows for solving the temperature in the fuel, helium gap, moderator, coolant film, and reflector.

$$\rho_i c_{p,i} \frac{\partial}{\partial t} T_i = k_i \nabla^2 T_i + Q_i \quad (8.5)$$

where

$i = f$  (fuel),  $g$  (helium gap),  $m$  (moderator),  $cf$  (coolant film),  $r$  (reflector)

$\rho_i$  = material  $i$  density [ $kg \cdot cm^{-3}$ ]

$c_{p,i}$  = material  $i$  heat capacity [ $J \cdot kg^{-1} \cdot K^{-1}$ ]

$k_i$  = material  $i$  thermal conductivity [ $W \cdot cm^{-1} \cdot K^{-1}$ ]

$T_i$  = material  $i$  temperature [ $^{\circ}C$ ]

$Q_i$  = material  $i$  volumetric heat source [ $W \cdot cm^{-3}$ ].

Equations 8.6 and 8.7 define the fuel heat source in the stand-alone and coupled calculations

$$Q_f = Q_0 \quad (8.6)$$

$$Q_f = \sum_{g=1}^G \epsilon_g^f \Sigma_g^f \phi_g \quad (8.7)$$

$$Q_g = Q_m = Q_{cf} = Q_r = 0 \quad (8.8)$$

where

$$Q_i = \text{material } i \text{ volumetric heat source } [W \cdot cm^{-3}]$$

$$\epsilon_g^f = \text{energy released per fission } [J]$$

$$\Sigma_g^f = \text{group } g \text{ macroscopic fission cross-section } [cm^{-1}]$$

$$\phi_g = \text{group } g \text{ neutron flux } [n \cdot cm^{-2} \cdot s^{-1}].$$

The governing equation of the coolant is the one-dimensional form of the continuity, momentum, and energy conservation equations [107]

$$\frac{\partial}{\partial t} \rho_c + \nabla \cdot (\rho_c u) = 0 \quad (8.9)$$

$$\rho_c \left( \frac{\partial}{\partial t} u + u \frac{\partial}{\partial z} u \right) = - \frac{\partial}{\partial z} p - \tau \frac{\epsilon}{A} - \rho_c g \quad (8.10)$$

$$\rho_c \left( \frac{\partial}{\partial t} (c_{p,c} T_c) + u \frac{\partial}{\partial z} (c_{p,c} T_c) \right) = \frac{\partial}{\partial t} p + u \frac{\partial}{\partial z} p + q'''_{conv} \quad (8.11)$$

$$\tau = \frac{f}{2} \rho_c u^2 \quad (8.12)$$

$$q'''_{conv} = h \frac{\epsilon}{A} (T_i - T_c) \quad (8.13)$$

where

$\rho_c$  = coolant density [ $kg \cdot cm^{-3}$ ]

$u$  = coolant velocity [ $cm \cdot s^{-1}$ ]

$p$  = coolant pressure [ $\times 10^{-2} Pa$ ]

$\tau$  = shear stress [ $\times 10^{-2} Pa$ ]

$\varepsilon$  = wetted perimeter [ $cm$ ]

$A$  = cross-sectional area [ $cm^2$ ]

$g$  = gravity [ $m \cdot s^{-2}$ ]

$c_{p,c}$  = coolant specific heat capacity [ $J \cdot kg^{-1} \cdot K^{-1}$ ]

$T_c$  = coolant temperature [ $^\circ C$ ]

$k_c$  = coolant thermal conductivity [ $W \cdot cm^{-1} \cdot K^{-1}$ ]

$q'''_{conv}$  = convective heat transfer [ $W \cdot cm^{-3}$ ]

$f$  = friction factor [-]

$h$  = heat transfer coefficient [ $W \cdot cm^{-2} \cdot K^{-1}$ ]

$T_i$  = solid temperature [ $^\circ C$ ].

Equation 8.14 [143] determines the friction factor  $f$

$$f = 8 \left[ \left( \frac{8}{Re} \right)^{12} + \frac{1}{(A+B)^{3/2}} \right]^{1/12}$$

$$A = \left\{ 2.457 \ln \left( \frac{1}{\left( \frac{7}{ReD_h} \right)^{0.9}} + 0.27 \frac{\varepsilon}{D_h} \right) \right\}^{16}$$

$$B = \left\{ \frac{37530}{Re} \right\}^{16} \quad (8.14)$$

where

$\varepsilon$  = surface roughness [-]

$Re$  = Reynolds number [-]

$D_h$  = hydraulic diameter [cm].

Equation 8.17 calculates the film thermal conductivity  $k_f$  [3]

$$Nu = 0.023 Re^{0.8} Pr^{0.4} \quad (8.15)$$

$$h = \frac{Nu \cdot k_c}{D_h} \quad (8.16)$$

$$k_f = h R_{cf} \ln(R_{cf}/R_c) \quad (8.17)$$

where

$Nu$  = Nusselt number [-]

$Pr$  = Prandtl number [-]

$h$  = heat transfer coefficient [ $W \cdot cm^{-2} \cdot s^{-1}$ ]

$D_h$  = hydraulic diameter [cm]

$k_c$  = coolant thermal conductivity [ $W \cdot cm^{-1} \cdot K^{-1}$ ]

$k_{cf}$  = coolant film thermal conductivity [ $W \cdot cm^{-1} \cdot K^{-1}$ ]

$R_{cf}$  = coolant film radius [cm]

$R_c$  = coolant channel radius [cm].

In the steady-state limit, equation 8.9 becomes

$$\nabla \cdot (\rho_c u) = 0 \quad (8.18)$$

which leads to

$$\rho_c u(z) = \rho_{c,i} u_i \quad (8.19)$$

where

$\rho_{c,i}$  = inlet coolant density

$u_i$  = inlet coolant velocity.

In the steady-state limit, the temperature equations (equations 8.5 and 8.11) become [89]

$$k_i \nabla^2 T_i + Q_i = 0 \quad (8.20)$$

$$\rho_{c,i} u_i \frac{\partial}{\partial z} (c_{p,c} T_c) = q''_{conv}. \quad (8.21)$$

### 8.3 Coolant distribution equation

The pressure drop in a coolant channel is proportional to the mass flow squared

$$\Delta P = B_i \dot{m}_i^2 \quad (8.22)$$

where

$\Delta P$  = pressure drop [ $Pa$ ]

$\dot{m}_i$  = channel  $i$  mass flow rate [ $kg \cdot s^{-1}$ ]

$B_i$  = constant specified by the chosen model, value that depends on  $\dot{m}_i$  [ $kg \cdot m^{-1}$ ]

which is equivalent to

$$\dot{m}_i = \sqrt{\frac{\Delta P}{B_i}}. \quad (8.23)$$

Assuming constant  $\Delta P$  across all coolant paths, and using equation 8.23, it is possible to calculate the total mass flow rate  $\dot{m}_T$

$$\dot{m}_T = \sum_i \dot{m}_i = \sum_i \sqrt{\frac{\Delta P}{B_i}} = \Delta P \frac{1}{\sum_i \sqrt{B_i}}. \quad (8.24)$$

Finally, equation 8.25 gives  $\Delta P$

$$\Delta P = \frac{\dot{m}_T}{\sum_i \frac{1}{\sqrt{B_i}}}. \quad (8.25)$$

These equations solve  $\dot{m}_i$  using an iterative scheme as  $B_i$  depends on  $\dot{m}_i$  [3]

$$B_i^{(n)} = f(\dot{m}_i^{(n)}) \quad (8.26)$$

$$\Delta P^{(n)} = \frac{\dot{m}_T}{\sum_i \frac{1}{\sqrt{B_i^{(n)}}}} \quad (8.27)$$

$$\dot{m}_i^{(n+1)} = \sqrt{\frac{\Delta P^{(n)}}{B_i^{(n)}}}. \quad (8.28)$$

# Appendix B

This appendix describes the equations for handling the cross-sections in different sections of this thesis.

## 9.1 Group constants homogenization

The following relations homogenize the group constants over a certain volume  $V_T$  [64]

$$\phi_{g,T} = \frac{\sum_i \phi_{g,i} V_i}{V_T} \quad (9.1)$$

$$\Sigma_{g,T}^t = \frac{\sum_i \Sigma_{g,i}^t \phi_{g,i} V_i}{\phi_g V_T} \quad (9.2)$$

$$\nu\Sigma_{g,T}^f = \frac{\sum_i \nu\Sigma_{g,i}^f \phi_{g,i} V_i}{\phi_g V_T} \quad (9.3)$$

$$\Sigma_{g' \rightarrow g,T}^s = \frac{\sum_i \Sigma_{g' \rightarrow g,i}^s \phi_{g,i} V_i}{\phi_g V_T} \quad (9.4)$$

$$\chi_{g,T}^t = \frac{\sum_i \chi_{g,i}^t \nu\Sigma_{g,i}^f \phi_{g,i} V_i}{\nu\Sigma_g^f \phi_g V_T} \quad (9.5)$$

$$D_{g,T} = \frac{\sum_i D_{g,i} \phi_{g,i} V_i}{\phi_g V_T} \quad (9.6)$$

where

$$\phi_{g,i} = \text{group } g, \text{ region } i \text{ neutron flux } [n \cdot cm^{-2} \cdot s^{-1}]$$

$$V_i = \text{region } i \text{ volume } [cm^3]$$

$$V_T = \text{total volume where the homogenization takes place } [cm^3]$$

$$\Sigma_{g,i}^t = \text{group } g, \text{ region } i \text{ macroscopic total cross-section } [cm^{-1}]$$

$$\nu = \text{number of neutrons produced per fission } [-]$$

$$\Sigma_{g,i}^f = \text{group } g, \text{ region } i \text{ macroscopic fission cross-section } [cm^{-1}]$$

$$\Sigma_{g' \rightarrow g,i}^s = \text{group } g' \text{ to group } g, \text{ region } i \text{ macroscopic scattering cross-section } [cm^{-1}]$$

$$\chi_{g,i}^t = \text{group } g, \text{ region } i \text{ total fission spectrum } [-]$$

$$D_{g,i} = \text{group } g, \text{ region } i \text{ diffusion coefficient } [cm].$$

## 9.2 Group constants condensation

The following equations collapse the group constants [64]

$$\phi_h = \sum_g \phi_g \quad (9.7)$$

$$\chi_h^t = \sum_g \chi_g^t \quad (9.8)$$

$$D_h^t = \frac{\sum_g D_g^t \phi_g}{\phi_{g'}} \quad (9.9)$$

$$\Sigma_h^t = \frac{\sum_g \Sigma_g^t \phi_g}{\phi_{g'}} \quad (9.10)$$

$$\nu \Sigma_h^f = \frac{\sum_g \nu \Sigma_g^f \phi_g}{\phi_{g'}} \quad (9.11)$$

$$\Sigma_{h' \rightarrow h}^s = \frac{\sum_{g'} \sum_g \Sigma_{g' \rightarrow g}^s \phi_{g'}}{\phi_{h'}} \quad (9.12)$$

where

$\phi_g$  = group  $g$  neutron flux [ $n \cdot cm^{-2} \cdot s^{-1}$ ]

$\chi_g^t$  = group  $g$  total fission spectrum [-]

$D_g$  = group  $g$  diffusion coefficient [ $cm$ ]

$\Sigma_g^t$  = group  $g$  macroscopic total cross-section [ $cm^{-1}$ ]

$v$  = number of neutrons produced per fission [-]

$\Sigma_g^f$  = group  $g$  macroscopic fission cross-section [ $cm^{-1}$ ]

$G$  = original number of energy groups [-]

$H$  = new number of energy groups [-]

$\Sigma_{g' \rightarrow g}^s$  = group  $g'$  to group  $g$  macroscopic scattering cross-section [ $cm^{-1}$ ].

### 9.3 Benchmark group constants

The benchmark specifies the following group constants: the normalized neutron flux  $\phi_g$ , the total fission spectrum  $\chi_g^t$ , the diffusion coefficient  $D_g$ , the macroscopic total cross-section  $\Sigma_g^t$ , number of neutrons produced per fission by the macroscopic fission cross-section  $v\Sigma_g^f$ , the macroscopic fission cross-section  $\Sigma_g^f$ , and the macroscopic scattering cross-section  $\Sigma_{g' \rightarrow g}^s$ .

Moltres solves equation 8.4, and requires the following group constants: the diffusion coefficient  $D_g$ , the macroscopic removal cross-section  $\Sigma_g^r$ , the macroscopic scattering cross-section  $\Sigma_{g' \rightarrow g}^s$ , the total fission spectrum  $\chi_g^t$ , and the number of neutrons produced per fission by the macroscopic fission cross-section  $v\Sigma_g^f$ .

Equation 9.13 calculates the removal cross-section [64]

$$\Sigma_{r,g} = \Sigma_{t,g} - \Sigma_{s,g \rightarrow g}. \quad (9.13)$$

# Appendix C

This appendix describes the analytical solution used in Section 5.1.1.

## 10.1 Verification of the thermal-fluids model

The analytical solution of the problem is

$$T_c(r, z) = T_{in} + \frac{q_{ave} R_f^2 L}{2 \rho c_p v \pi R_c^2} \left[ 1 + \cos\left(\frac{\pi}{L}z\right) \right] \quad (10.1)$$

$$T_3(z) = T_c(z) + \frac{q_{ave} \pi}{2} \sin\left(\frac{\pi}{L}z\right) R_f^2 \frac{\ln(R_i/R_m)}{2k_i} \quad (10.2)$$

$$T_2(z) = T_3(z) + \frac{q_{ave} \pi}{2} \sin\left(\frac{\pi}{L}z\right) R_f^2 \frac{\ln(R_m/R_g)}{2k_m} \quad (10.3)$$

$$T_1(z) = T_2(z) + \frac{q_{ave} \pi}{2} \sin\left(\frac{\pi}{L}z\right) R_f^2 \frac{\ln(R_g/R_f)}{2k_g} \quad (10.4)$$

$$T_f(r=0, z) = T_1(z) + \frac{q_{ave} \pi}{2} \sin\left(\frac{\pi}{L}z\right) R_f^2 \frac{1}{4k_f} \quad (10.5)$$

$$T_f(r, z=L/2) = \frac{q_{ave}}{4k_f} (R_f^2 - r^2) + T_1(z=L/2) \quad (10.6)$$

$$T_g(r, z=L/2) = \frac{T_1(z=L/2) - T_2(z=L/2)}{\ln(R_f/R_g)} \ln(r/R_g) + T_1(z=L/2) \quad (10.7)$$

$$T_m(r, z=L/2) = \frac{T_2(z=L/2) - T_3(z=L/2)}{\ln(R_g/R_m)} \ln(r/R_m) + T_2(z=L/2) \quad (10.8)$$

$$T_i(r, z=L/2) = \frac{T_3(z=L/2) - T_c(z=L/2)}{\ln(R_m/R_i)} \ln(r/R_i) + T_3(z=L/2) \quad (10.9)$$

$$T_c(r, z=L/2) = T_c(z=L/2) \quad (10.10)$$

where

$T_c$  = bulk coolant temperature [ $^{\circ}C$ ]

$T_{in}$  = inlet coolant temperature [ $^{\circ}C$ ]

$q_{ave}$  = average power density [ $W \cdot cm^{-3}$ ]

$R_f$  = fuel compact radius [cm]

$L$  = fuel column height [cm]

$\rho$  = helium density [ $kg \cdot cm^{-3}$ ]

$c_p$  = helium heat capacity [ $J \cdot kg^{-1} \cdot K^{-1}$ ]

$v$  = average helium velocity [ $cm \cdot s^{-1}$ ]

$R_c$  = coolant channel radius [cm]

$R_g$  = gap radius [cm]

$R_m$  = moderator radius [cm]

$R_i$  = film radius [cm]

$k_f$  = fuel compact thermal conductivity [ $W \cdot cm^{-1} \cdot K^{-1}$ ]

$k_g$  = gap thermal conductivity [ $W \cdot cm^{-1} \cdot K^{-1}$ ]

$k_m$  = moderator thermal conductivity [ $W \cdot cm^{-1} \cdot K^{-1}$ ]

$k_i$  = film thermal conductivity [ $W \cdot cm^{-1} \cdot K^{-1}$ ].

# References

- [1] H. Brey, "Development History of the Gas Turbine Modular High Temperature Reactor," 2001.
- [2] B. Barre, "Gas-Cooled Reactors," 2010.
- [3] G. Melese and R. Katz, *Thermal and flow design of helium-cooled reactors*. La Grange Park, Ill., USA: American Nuclear Society, 1984.
- [4] O. NEA, "Benchmark of the Modular High-Temperature Gas-Cooled Reactor MHTGR)-350 MW Core Design," Tech. Rep. NEA/NSC/R(2017)4, OECD, 2017.
- [5] P. Demkowicz, Paul, "TRISO Fuel: Design, Manufacturing, and Performance," July 2019.
- [6] P. Paviet-Hartmann, G. Cerefice, M. Riveros Stacey, and S. Bakhtiar, "Analysis of Nuclear Proliferation Resistance Reprocessing and Recycling Technologies," (Japan), May 2011.
- [7] J. Hales, R. Williamson, S. Novascone, D. Perez, B. Spencer, and G. Pastore, "Multidimensional multiphysics simulation of TRISO particle fuel," *Journal of Nuclear Materials*, vol. 443, pp. 531–543, Nov. 2013.
- [8] R. G. Ballinger, C. Y. Wang, A. Kadak, N. Todreas, B. Mirick, E. Demetri, and M. Koronowski, "Balance of Plant System Analysis and Component Design of Turbo-Machinery for High Temperature Gas Reactor Systems," Tech. Rep. 828709, Massachusetts Institute of Technology, Northern Engineering and Research, Aug. 2004.
- [9] L. Herranz, J. Linares, and B. Moratilla, "Power cycle assessment of nuclear high temperature gas-cooled reactors," *Applied Thermal Engineering*, vol. 29, pp. 1759–1765, June 2009.
- [10] P. Breeze, "Nuclear Power," in *Power Generation Technologies*, pp. 353–378, Elsevier, 2014.
- [11] H. C. No, J. H. Kim, and H. M. Kim, "A REVIEW OF HELIUM GAS TURBINE TECHNOLOGY FOR HIGH-TEMPERATURE GAS-COOLED REACTORS," Jan. 2007.
- [12] IAEA, "Current status and future development of modular high temperature gas cooled reactor technology," Feb. 2001.
- [13] C. Baxi, A. Shenoy, V. Kostin, N. Kodochigov, A. Vasyaev, S. Belov, and V. Golovko, "Evaluation of alternate power conversion unit designs for the GT-MHR," *Nuclear Engineering and Design*, vol. 238, pp. 2995–3001, Nov. 2008.
- [14] M. Nagashima, "JAPAN's HYDROGEN STRATEGY AND ITS ECONOMIC AND GEOPOLITICAL IMPLICATIONS," tech. rep., IFRI, Oct. 2018.
- [15] W. Doenitz, R. Schmidberger, and E. Steinheil, "HYDROGEN PRODUCTION BY HIGH TEMPERATURE ELECTROLYSIS OF WATER VAPOURt," p. 9, 1980.
- [16] B. Yildiz and M. Kazimi, "Efficiency of hydrogen production systems using alternative nuclear energy technologies," *International Journal of Hydrogen Energy*, vol. 31, pp. 77–92, Jan. 2006.
- [17] A. Neylan, D. Graf, and A. Millunzi, "The modular high temperature gas-cooled reactor (MHTGR) in the U.S.," *Nuclear Engineering and Design*, vol. 109, pp. 99–105, Sept. 1988.

- [18] F. Silady, J. Cunliffe, and L. Walker, “The licensing experience of the Modular High-Temperature Gas-Cooled Reactor (MHTGR),” *Energy*, vol. 16, pp. 417–424, Sept. 1988.
- [19] A. J. Huning, “A STEADY STATE THERMAL HYDRAULIC ANALYSIS METHOD FOR PRISMATIC GAS REACTORS,” May 2014.
- [20] DOE-NE and GIF, “A Technology Roadmap for Generation IV Nuclear Energy Systems,” Tech. Rep. GIF-002-00, 859029, Dec. 2002.
- [21] P. E. MacDonald, “NGNP Point Design - Results of the Initial Neutronics and Thermal-Hydraulic Assessments During Fy-03,” Tech. Rep. INEEL/EXT-03-00870 Rev. 1, INL, Idaho Falls, Sept. 2003.
- [22] GIF, “GIF Portal - Home - VHTR,” 2019.
- [23] S. C. Nuclear, “Star Core Spec Sheet,” Dec. 2015.
- [24] USNC, “MMR - USNC,” 2019.
- [25] W. N. News, “Micro modular reactors proposed for Idaho and Illinois : New Nuclear - World Nuclear News,” Oct. 2020.
- [26] A. Lindsay, G. Ridley, A. Rykhlevskii, and K. Huff, “Introduction to Moltres: An application for simulation of Molten Salt Reactors,” *Annals of Nuclear Energy*, vol. 114, pp. 530–540, Apr. 2018.
- [27] N.-i. Tak, M.-H. Kim, and W. J. Lee, “Numerical investigation of a heat transfer within the prismatic fuel assembly of a very high temperature reactor,” *Annals of Nuclear Energy*, vol. 35, pp. 1892–1899, Oct. 2008.
- [28] U. Rohde, S. Baier, S. Duerigen, E. Fridman, S. Kliem, and B. Merk, “Development and verification of the coupled 3D neutron kinetics/thermal-hydraulics code DYN3D-HTR for the simulation of transients in block-type HTGR,” *Nuclear Engineering and Design*, vol. 251, pp. 412–422, Oct. 2012.
- [29] F. Bostelmann, H. R. Hammer, J. Ortensi, G. Strydom, K. Velkov, and W. Zwermann, “Criticality calculations of the Very High Temperature Reactor Critical Assembly benchmark with Serpent and SCALE/KENO-VI,” *Annals of Nuclear Energy*, vol. 90, pp. 343–352, Apr. 2016.
- [30] J. C. Ragusa and V. S. Mahadevan, “Consistent and accurate schemes for coupled neutronics thermal-hydraulics reactor analysis,” *Nuclear Engineering and Design*, vol. 239, pp. 566–579, Mar. 2009.
- [31] H. Park, D. A. Knoll, D. R. Gaston, and R. C. Martineau, “Tightly Coupled Multiphysics Algorithms for Pebble Bed Reactors,” *Nuclear Science and Engineering*, vol. 166, pp. 118–133, Oct. 2010.
- [32] D. Gaston, C. Newman, G. Hansen, and D. Lebrun-Grandié, “MOOSE: A parallel computational framework for coupled systems of nonlinear equations,” *Nuclear Engineering and Design*, vol. 239, pp. 1768–1778, Oct. 2009.
- [33] A. Novak, L. Zou, J. Peterson, D. Andrs, J. Kelly, R. Slaybaugh, R. Martineau, and H. Gougar, “Pronghorn Theory Manual,” Feb. 2018.
- [34] E. Lewis and I. Dilber, “Finite element, nodal and response matrix methods: A variational synthesis for neutron transport,” *Progress in Nuclear Energy*, vol. 18, pp. 63–74, Jan. 1986.
- [35] R. Lawrence, “Progress in nodal methods for the solution of the neutron diffusion and transport equations,” *Progress in Nuclear Energy*, vol. 17, pp. 271–301, Jan. 1986.
- [36] D. Delp, D. Fischer, J. Harriman, and M. Stedwell, “FLARE, A three-dimensional boiling water reactor simulator,” 1964.
- [37] N. K. Gupta, “NODAL METHODS FOR THREE-DIMENSIONAL SIMULATORS,” p. 23, 1981.
- [38] T. Duracz, “A Nodal Method in Hexagonal Geometry,” in *International Meeting on Advances in Mathematical Methods for Solution of Nuclear Engineering Problems*, (Munich, Germany), Apr. 1981.

- [39] M. R. Wagner, "Three-Dimensional Nodal Diffusion and Transport Theory Methods for Hexagonal- $z$  Geometry," *Nuclear Science and Engineering*, vol. 103, pp. 377–391, Dec. 1989.
- [40] W. E. Fitzpatrick and A. M. Ougouag, "HEXPEDITE: A Net Current Multigroup Nodal Diffusion Method for Hexagonal- $z$  Geometry," 1992.
- [41] W. Fitzpatrick, *Developments in Nodal Reactor Analysis Tools for Hexagonal Geometry*. PhD thesis, University of Illinois at Urbana-Champaign, Urbana, IL, 1995.
- [42] J. Ortensi, J. Cogliati, M. Pope, J. Bess, R. Ferrer, A. Bingham, and A. Ougouag, "Deterministic Modeling of the High Temperature Test Reactor with DRAGON-HEXPEDITE," in *Proceedings of HTR 2010*, (Prague, Czech Republic), Oct. 2010.
- [43] R. C. C. Collection, "MCNP5 Monte Carlo N-Particle Transport Code System," 2003.
- [44] J. Leppänen, "Serpent – a Continuous-energy Monte Carlo Reactor Physics Burnup Calculation Code," June 2015.
- [45] R. Lawrence, "The DIF3D Nodal Neutronics Option for Two- and Three-Dimensional Diffusion-Theory Calculations in Hexagonal Geometry," Mar. 1983.
- [46] T. Downar, D. Lee, Y. Xu, and T. Kozlowski, "PARCS v2.6 US NRC Core Neutronics Simulator THEORY MANUAL," June 2004.
- [47] C. M. Kang and K. F. Hansen, "Finite Element Methods for Reactor Analysis," *Nuclear Science and Engineering*, vol. 51, pp. 456–495, Aug. 1973.
- [48] S. Cavdar and H. Ozgener, "A finite element/boundary element hybrid method for 2-D neutron diffusion calculations," *Annals of Nuclear Energy*, vol. 31, pp. 1555–1582, Sept. 2004.
- [49] H. Lee, C. Jo, and J. Noh, "DEVELOPMENT OF CAPP CODE BASED ON THE FINITE ELEMENT METHOD FOR THE ANALYSIS OF VHTR CORES," in *Proceedings of the 4th International Topical Meeting on High Temperature Reactor Technology*, (Washington, DC USA), Oct. 2008.
- [50] J. Lautard, S. Loubiere, and C. Magnaud, "CRONOS, A Modular Computational System for Neutronic Core Calculations," Sept. 1990.
- [51] H. C. Lee, C. K. Jo, and J. M. Noh, "Development of the CAPP code for the Analysis of Block Type VHTRs," 2011.
- [52] Y. Wang, S. Schunert, and V. Laboure, "Rattlesnake Theory Manual," Apr. 2019.
- [53] F. Damian, "VHTR Core Preliminary Analysis Using NEPTIS3 / CAST3M Coupled Modelling," in *Fourth International Topical Meeting on High Temperature Reactor Technology, Volume 1*, (Washington, DC, USA), pp. 419–429, ASMEDC, Jan. 2008.
- [54] C. Cavalier, F. Damian, C. Trakas, and M. Groizard, "Presentation of the HTR Neutronic Code System," 2005.
- [55] E. Studer, A. Beccantini, S. Gounand, F. Dabbene, J. Magnaud, H. Paillère, I. Limaiem, F. Damian, H. Golfier, C. Bassi, and J. Garnier, "CAST3M/ARCTURUS: A coupled heat transfer CFD code for thermal–hydraulic analyzes of gas cooled reactors," *Nuclear Engineering and Design*, vol. 237, pp. 1814–1828, Sept. 2007.
- [56] F. Reitsma, J. Han, K. Ivanov, and E. Sartori, "The OECD-NEA/NSC PBMR400 MW coupled neutronics thermal hydraulics transient benchmark - Steady-state results and status," Sept. 2008.
- [57] G. Strydom, J. Ortensi, S. Sen, and H. Hammer, "INL Results for Phase I and III of the OECD/NEA MHTGR-350 Benchmark," Sept. 2013.
- [58] Y. Wang, C. Rabiti, and G. Palmiotti, "Krylov Solvers Preconditioned with the Low-Order Red-Black Algorithm for The Pn Hybrid FEM for the INSTANT Code," in *International Conference on Mathematics and Computational Methods Applied to Nuclear Science and Engineering*, (Rio de Janeiro, Brazil), May 2011.

- [59] Lee, Zhong, Taiwo, Yang, Smith, and Palmiotti, "Status of Reactor Physics Activities on Cross Section Generation and Functionalization for the Prismatic Very High Temperature Reactor, and Development of Spatially-Heterogeneous Codes," Aug. 2006.
- [60] J. S. Han, "Sensitivity Study on the Energy Group Structure for High Temperature Reactor Analysis," May 2008.
- [61] R. Grimesey, "COMBINE/PC-A Portable ENDF/B Version 6 Neutron Spectrum and Cross Section Generation Program," 1994.
- [62] B. Bandini, *A Three-dimensional Transient Neutronics Routine for the TRAC-PF1 Reactor Thermal Hydraulic Computer Code*. Ph.D., The Pennsylvania State University, 1990.
- [63] G. O. Company, "Nuclear Design Methods and Experimental Data in Use at Gulf General Atomic," 1973.
- [64] J. J. Duderstadt and L. J. Hamilton, *Nuclear Reactor Analysis*. New York: Wiley, 1 edition ed., Jan. 1976.
- [65] G. Strydom, F. Bostelmann, and S. J. Yoon, "Results for Phase I of the IAEA Coordinated Research Program on HTGR Uncertainties," Tech. Rep. INL/EXT-14-32944, 1173079, INL, Jan. 2015.
- [66] B. Tyobeka, F. Reitsma, and K. Ivanov, "HTGR REACTOR PHYSICS, THERMAL-HYDRAULICS AND DEPLETION UNCERTAINTY ANALYSIS: A PROPOSED IAEA COORDINATED RESEARCH PROJECT," in *International Conference on Mathematics and Computational Methods Applied to Nuclear Science and Engineering*, (Rio de Janeiro, Brazil), American Nuclear Society, May 2011.
- [67] A. Shenoy and D. McEachern, "HTGR Core Thermal Design Methods and Analysis," Dec. 1974.
- [68] G. Atomics, "Gas Turbine-Modular Helium Reactor (GT-MHR) Conceptual Design Description Report," 1996.
- [69] INL, "RELAP5-3D/ATHENA Code Manual," 2005.
- [70] S. M. Reza, E. Harvego, M. Richards, A. Shenoy, and K. Pddicord, "Design of an Alternative Coolant Inlet Flow Configuration for the Modular Helium Reactor," June 2006.
- [71] H. S. Lim and H. C. No, "GAMMA Multidimensional Multicomponent Mixture Analysis to Predict Air Ingress Phenomena in an HTGR," *Nuclear Science and Engineering*, vol. 152, pp. 87–97, Jan. 2006.
- [72] H. C. No, H. S. Lim, J. Kim, C. Oh, L. Siefken, and C. Davis, "Multi-component diffusion analysis and assessment of GAMMA code and improved RELAP5 code," *Nuclear Engineering and Design*, vol. 237, pp. 997–1008, May 2007.
- [73] E. Takada, S. Nakagawa, N. Fujimoto, and D. Tochio, "Core thermal-hydraulic design," *Nuclear Engineering and Design*, vol. 233, pp. 37–43, Oct. 2004.
- [74] S. Maruyama, T. Murakami, Y. Kiso, and Y. Sudo, "Verification of in-vessel thermal and hydraulic analysis code FLOWNET," 1988.
- [75] Nakano, Tsuji, and Tazawa, "Conceptual Reactor Design Study of Very High Temperature Reactor (VHTR) with Prismatic-Type Core," 2008.
- [76] In, Lee, Lim, and Lee, "Three-Dimensional Analysis of the Hot-Spot Fuel Temperature in Pebble Bed and Prismatic Modular Reactors," May 2006.
- [77] A. Inc., "CFX 10," 2006.
- [78] A. Incorporated, "CFX 11 Manuals," 2006.
- [79] H. Sato, R. Johnson, and R. Schultz, "Computational fluid dynamic analysis of core bypass flow phenomena in a prismatic VHTR," *Annals of Nuclear Energy*, vol. 37, pp. 1172–1185, Sept. 2010.
- [80] F. Inc, "FLUENT," 2006.

- [81] O. Cioni, M. Marchand, G. Geffraye, and F. Ducros, “3D thermal-hydraulic calculations of a modular block-type HTR core,” *Nuclear Engineering and Design*, vol. 236, pp. 565–573, Mar. 2005.
- [82] U. Bieder, C. Calvin, and P. Emonot, “PRICELES: an object oriented code for industrial large eddy simulations.,” June 2000.
- [83] N.-I. Tak, S. N. Lee, M.-H. Kim, H. S. Lim, and J. M. Noh, “DEVELOPMENT OF A CORE THERMO-FLUID ANALYSIS CODE FOR PRISMATIC GAS COOLED REACTORS,” *NUCLEAR ENGINEERING AND TECHNOLOGY*, p. 14, 2014.
- [84] B. W. Travis and M. S. El-Genk, “Thermal-hydraulics analyses for 1/6 prismatic VHTR core and fuel element with and without bypass flow,” *Energy Conversion and Management*, vol. 67, pp. 325–341, Mar. 2013.
- [85] CD-Adapco, “STAR-CCM+ release 7.04,” 2012.
- [86] J.-P. Simoneau, J. Champigny, B. Mays, and L. Lommers, “Three-dimensional simulation of the coupled convective, conductive, and radiative heat transfer during decay heat removal in an HTR,” *Nuclear Engineering and Design*, vol. 237, pp. 1923–1937, Sept. 2007.
- [87] C. D. Limited, “STAR-CD Version 3.24 User Guide,” 2004.
- [88] D. Nield and A. Bejan, *Convection in Porous Media*. New York, USA: Springer-Verlag, 1999.
- [89] Tak, Kim, Lim, and Noh, “A practical method for Whole-Core Thermal Analysis of a Prismatic Gas-Cooled Reactor,” Mar. 2012.
- [90] A. Huning, “A NOVEL CORE ANALYSIS METHOD FOR PRISMATIC HIGH TEMPERATURE GAS REACTORS,” Aug. 2016.
- [91] N.-i. Tak, H. C. Lee, H. S. Lim, and T. Y. Han, “CAPP/GAMMA+ code system for coupled neutronics and thermo-fluid simulation of a prismatic VHTR core,” *Annals of Nuclear Energy*, vol. 92, pp. 228–242, June 2016.
- [92] Sanchez, Hebert, Stankovski, Coste, Loubiere, V. der Gucht, and Zmijarevic, “APOLLO2 Twelve Years Later,” Sept. 1999.
- [93] R. Stainsby, “Investigation of Local Heat Transfer Phenomena in a Prismatic Modular Reactor Core,” tech. rep., AMEC NSS Limited, 2008.
- [94] R. Stamml'er, “HELIOS Methods,” 1998.
- [95] Yuk, Cho, Jo, Tak, and Lim, “Time-dependent neutron diffusion analysis using finite element method for a block-type VHTR core design,” Jan. 2020.
- [96] J. Ortensi, D. Andrs, A.A. Bingham, R.C. Martineau, and J.W. Peterson, “Initial Coupling of the RELAP-7 and PRONGHORN Applications,” Tech. Rep. INL/EXT-12-27350, 1060984, INL, Oct. 2012.
- [97] D. Andrs, R. Berry, R. Gaston, R. Martineau, J. Peterson, H. Zhang, H. Zhao, and L. Zou, “RELAP-7 level 2 milestone report: Demonstration of a steady state single phase pwr simlulation with relap-7,” 2012.
- [98] O. NEA, “Coupled Neutronic/Thermal- Fluid Benchmark of the MHTGR-350 MW Core Design: Results for Phase I Exercise 1,” Feb. 2020.
- [99] N.-i. Tak, T. Y. Han, and H. C. Lee, “Coupled Neutronics and Thermo-Fluid Simulation of Full-Core Prismatic Gas-Cooled Reactor Using DeCART/CORONA Code System,” in *Transactions of the Korean Nuclear Society Autumn Meeting*, (Gyeongju, Korea), p. 4, Oct. 2016.
- [100] KAERI, “DeCART v1.2 User’s Manual,” 2007.
- [101] IAEA, “Evaluation of high temperature gas cooled reactor performance: Benchmark analysis related to initial testing of the HTTR and HTR-10,” Nov. 2003.

- [102] J. Leppänen, *Development of a New Monte Carlo Reactor Physics Code*. PhD thesis, Helsinki University of Technology, Espoo, Finland, June 2007.
- [103] J. Leppänen, M. Aufiero, E. Fridman, R. Rachamin, and S. van der Marck, “Calculation of effective point kinetics parameters in the Serpent 2 Monte Carlo code,” *Annals of Nuclear Energy*, vol. 65, pp. 272–279, Mar. 2014.
- [104] B. S. Kirk, J. W. Peterson, R. H. Stogner, and G. F. Carey, “libMesh : a C++ library for parallel adaptive mesh refinement/coarsening simulations,” *Engineering with Computers*, vol. 22, pp. 237–254, Dec. 2006.
- [105] Balay, Brune, Buschelman, Gropp, Karpeyev, Knepley, C. McInnes, Rupp, Smith, and Zhang, “PETSc Users Manual,” Apr. 2016.
- [106] D. Knoll and D. Keyes, “Jacobian-free Newton–Krylov methods: a survey of approaches and applications,” *Journal of Computational Physics*, vol. 193, pp. 357–397, Jan. 2004.
- [107] F. White, *Viscous Fluid Flow*. McGraw Hill, third ed., 2006.
- [108] J. Krebs, M. Laigle, R. Lenain, G. Mathonniere, and A. Nicolas, “Calculational Methods for PWRs,” Sept. 1990.
- [109] M. Pater, “Multiphysics simulations of Molten Salt Reactors using the Moltres code,” Master’s thesis, Universite Paris-Saclay, Copenhagen, Denmark, Sept. 2019.
- [110] C. Geuzaine and J.-F. Remacle, “Gmsh: a three-dimensional finite element mesh generator with built-in pre- and post-processing facilities.,” June 2020.
- [111] G. Marleau, A. Hebert, and R. Roy, “A USER GUIDE FOR DRAGON VERSION4,” p. 318, 2016.
- [112] NIST, “Thermophysical Properties of Fluid Systems,” Oct. 2020.
- [113] R. W. Johnson, H. Sato, and R. R. Schultz, “CFD Analysis of Core Bypass Phenomena,” p. 60, Nov. 2009.
- [114] P. J. Burke, D. I. Stern, and S. B. Bruns, “The Impact of Electricity on Economic Development: A Macroeconomic Perspective,” *International Review of Environmental and Resource Economics*, vol. 12, pp. 85–127, Nov. 2018.
- [115] M. El-Shafie, S. Kambara, and Y. Hayakawa, “Hydrogen Production Technologies Overview,” *Journal of Power and Energy Engineering*, vol. 07, no. 01, pp. 107–154, 2019.
- [116] U. EPA, “Sources of Greenhouse Gas Emissions,” Jan. 2020.
- [117] Z. Ming, A. Olson, H. Jiang, M. Mogadali, and N. Schlag, “Resource Adequacy in the Pacific Northwest,” Mar. 2019.
- [118] U. D. of Energy, “Confronting the Duck Curve: How to Address Over-Generation of Solar Energy,” Oct. 2017.
- [119] B. Bouillon, “Prepared Statement of Brad Bouillon on behalf of the California Independent System Operator Corporation,” June 2014.
- [120] U. of Illinois at Urbana-Champaign, “Illinois Climate Action Plan,” 2015.
- [121] C. M. Kalamaras and A. M. Efstathiou, “Hydrogen Production Technologies: Current State and Future Developments,” *Conference Papers in Energy*, vol. 2013, pp. 1–9, 2013.
- [122] USDRIVE, “Hydrogen Production Tech Team Roadmap,” Nov. 2017.
- [123] J. E. O’Brien, C. M. Stoots, J. S. Herring, M. G. McKellar, E. A. Harvego, M. S. Sohal, and K. G. Condie, “High Temperature Electrolysis for Hydrogen Production from Nuclear Energy TechnologySummary,” Tech. Rep. INL/EXT-09-16140, 978368, INL, Feb. 2010.
- [124] HELMETH, “High temperature electrolysis cell (SOEC),” Feb. 2020.

- [125] J. E. O'Brien, J. S. Herring, C. M. Stoots, M. G. McKellar, E. A. Harvego, K. G. Condie, G. K. Housley, and J. J. Hartvigsen, "Status of the INL High- Temperature Electrolysis Research Program – Experimental and Modeling," in *Fourth Information Exchange Meeting on the Nuclear Production of Hydrogen*, p. 13, 2010.
- [126] L. Brown, G. Besenbruch, R. Lentsch, K. Schultz, J. Funk, P. Pickard, A. Marshall, and S. Showalter, "HIGH EFFICIENCY GENERATION OF HYDROGEN FUELS USING NUCLEAR POWER," tech. rep., GENERAL ATOMICS (US), June 2003.
- [127] Benjamin Russ, "Sulfur Iodine Process Summary for the Hydrogen Technology Down-Selection," Tech. Rep. INL/EXT-12-25773, 1047207, INL, May 2009.
- [128] S. G. Dotson and K. D. Huff, "Optimal Sizing of a Micro-Reactor for Embedded Grid Systems," in *Transactions of the American Nuclear Society Student Conference*, (Raleigh, N.C.), American Nuclear Society, Mar. 2020.
- [129] US-DOE, "The Ultimate Fast Facts Guide to Nuclear Energy," Fact Sheet DOE/NE-0150, Department of Energy Office of Nuclear Energy, Washington D.C., Jan. 2019. <https://www.energy.gov/ne/downloads/ultimate-fast-facts-guide-nuclear-energy>.
- [130] W. N. Association, "Small nuclear power reactors - World Nuclear Association," June 2020.
- [131] C.-U. M. T. District, "Champaign-Urbana Mass Transit District Public Records," Dec. 2019.
- [132] P. Varney, "Personal Communication," Jan. 2020.
- [133] D. O. of Energy Efficiency and Renewable Energy, "Hydrogen Production Processes," 2020. Library Catalog: [www.energy.gov](http://www.energy.gov).
- [134] A. F. D. Center, "Fuel Properties Comparison," Oct. 2014.
- [135] E. I. Administration, "How much carbon dioxide is produced by burning gasoline and diesel fuel?," Apr. 2014.
- [136] R. Hernandez, M. Todosow, and N. R. Brown, "Micro heat pipe nuclear reactor concepts: Analysis of fuel cycle performance and environmental impacts," *Annals of Nuclear Energy*, vol. 126, pp. 419–426, Apr. 2019.
- [137] B. Harlan, "X-energy Xe-100 Reactor initial NRC meeting," Sept. 2018.
- [138] M. Ding, J. L. Kloosterman, T. Kooijman, and R. Linssen, "Design of a U-Battery," Tech. Rep. PNR-131-2011-014, Urenco, and Koopman and Witteveen, Nov. 2011.
- [139] U. E. I. Administration, "Electric Power Monthly with data for February 2020," Apr. 2020.
- [140] A. Ursua, L. M. Gandia, and P. Sanchis, "Hydrogen Production From Water Electrolysis: Current Status and Future Trends," *Proceedings of the IEEE*, vol. 100, pp. 410–426, Feb. 2012.
- [141] D. E. E. a. R. Energy, "Fuel cells fact sheet," Nov. 2015.
- [142] D. Hetrick, "Dynamics of Nuclear Reactors," 1973.
- [143] S. W. Churchill, "friction-factor equation spans all fluid-flow regimes," 1977.